

THESIS FOR THE DEGREE OF DOCTOR OF PHILOSOPHY

**Local structure and dynamics in proton- and hydride-ion  
conducting perovskite-type oxides; bulk and films**

Elena Naumovska

Department of Chemistry and Chemical Engineering  
CHALMERS UNIVERSITY OF TECHNOLOGY  
Göteborg, Sweden 2025

**Local structure and dynamics in proton- and hydride-ion conducting perovskite-type oxides; bulk and films**

Elena Naumovska

©Elena Naumovska, 2025

ISBN: 978-91-8103-238-3

Doktorsavhandlingar vid Chalmers tekniska högskola.

Ny serie nr: 5696

ISSN 0346-718X

Department of Chemistry and Chemical Engineering  
Chalmers University of Technology  
SE-41296 Göteborg, Sweden

Printed by Chalmers Digitaltryck  
Göteborg, Sweden 2025

Cover: Watercolor abstraction describing a neutron scattering investigation of proton motions in a perovskite-type material. Inspired by the work of Paul Klee.

This thesis builds on my Licentiate Thesis [1]. Please note that the cover photo and the majority of the figures were drawn in Canva. European Young Engineers are thanked for access to the pro version of the program. Please also note that in some instances Talkai was used solely for the purpose of rephrasing sentences and spell-checks for clarity and improved structure.

Elena Naumovska  
Department of Chemistry and Chemical Engineering  
Chalmers University of Technology

### Abstract

Acceptor doped proton- and hydride-ion conducting perovskite-type oxides are promising candidates for application as electrolytes in solid oxide fuel cells at temperatures below 400 °C. However, to be applied in fuel cells, these electrolytes should have ionic conductivities of at least  $10^{-2}$  S/cm which, at present, these materials do not have. Increasing the ionic conductivity relies on a deeper understanding of their local structure and dynamics. Key challenges are related to elucidating how the type and concentration of dopant atoms and the microstructure of these materials influence the structure and proton- or hydride-ion dynamics. In this thesis, these challenges have been approached using quasielastic neutron scattering and infrared spectroscopy. The studies of local structure and dynamics have focused both on microcrystalline bulk samples and on nanocrystalline film samples.

The study of powder samples focused on  $\text{BaZr}_{1-x}\text{Sc}_x\text{O}_{3-x/2}$  with  $x = 0.10$  and  $0.50$ , with the aim to unravel the effect of doping concentration on localized proton dynamics. A key result of this study is that the localized proton dynamics are largely unaffected by the Sc dopant concentration. Besides contributing to an increased fundamental understanding, this knowledge is of importance for further optimization of these materials in actual applications. The study of films focused on  $\text{BaZr}_{1-x}\text{Sc}_x\text{O}_{3-x/2}$ , ( $x = 0.45, 0.54, \text{ and } 0.65$ ), with the aim to elucidate the influence of doping concentration on the local structure and proton environments. The results show that the local proton environments change as a function of increasing Sc dopant concentration, with the creation of preferred proton environments for  $x > 0.50$ . In comparison, the results for powder samples show a more homogeneous distribution of proton environments quite independent of  $x$ . It follows that the local structure of these proton-conducting oxides depends on the microstructure of the samples, which may be tuned by the fabrication method.

Additionally, the effect on the type of dopant atom on the proton dynamics was investigated for powder samples of the brownmillerite-type proton-conducting oxides  $\text{Ba}_2\text{In}_{1.85}\text{M}_{0.15}\text{O}_5$  with  $\text{M} = \text{In}, \text{Ga}, \text{Sc}$  and  $\text{Y}$ . The results show that, compared to  $\text{Ba}_2\text{In}_2\text{O}_5$ , introducing a dopant atom effectively lowers the temperature for both localized and long-range proton dynamics, which is associated with the presence of an additional proton site, quite independent of the type of dopant atom. This finding suggests that doping the  $\text{Ba}_2\text{In}_2\text{O}_5$  structure is an effective strategy for promotion of long-range proton diffusion.

Beyond proton-conducting oxides, the relationship between local structure, and hydride-ion incorporation and dynamics was investigated for the perovskite-type oxyhydrides  $\text{BaTiO}_{2.88}\text{H}_{0.12}$  and  $\text{BaZr}_{1-x}\text{In}_x\text{O}_{3-x/2}$  ( $x = 0.10\text{--}0.59$ ). This work did not only show that the presence of oxygen vacancies seems critical for proton diffusion to occur, but also that the concentration of oxygen vacancies can be tuned by the selection of precursors used in the synthesis of these novel materials.

**Keywords:** *Perovskite, neutron scattering, quasielastic neutron scattering, proton conductors, hydride-ion conductors, infrared spectroscopy, solid oxide fuel cells.*



# List of publications

This thesis is based on the following publications:

**I Localized proton motions in the proton-conducting perovskites  $\text{BaZr}_{1-x}\text{Sc}_x\text{O}_3\text{H}_x$  ( $x = 0.10$  and  $0.50$ ) investigated with quasielastic neutron scattering**

E. Naumovska, J. Orstadius, A. Perrichon, R. Lavén, M. M. Koza, Z. Evenson, and M. Karlsson

*The Journal of Physical Chemistry C*, 2023, 127(51), 24532-24541.

**II Proton diffusion in proton conducting  $\text{Ba}_2\text{In}_{1.85}\text{M}_{0.15}\text{O}_5$  ( $\text{M} = \text{In}, \text{Ga}, \text{Sc}$  and  $\text{Y}$ ) investigated with quasielastic neutron scattering**

E. Naumovska, L. Fine, A. Perrichon, F. Piccinelli, N. Jalarvo, F. Juranyi, M. M. Koza, and M. Karlsson

*In Manuscript*

**III Local structure of hydrated nanocrystalline films of the proton conductor  $\text{BaZr}_{1-x}\text{Sc}_x\text{O}_{3-x/2}$  studied by infrared spectroscopy**

E. Naumovska, G. K. Nzulu, L. Mazzei, A. le Febvrier, K. Komander, M. Magnuson, M. Wolff, P. Eklund, and M. Karlsson

*Vibrational Spectroscopy*, 2024, 130, 103622.

**IV Mechanism of hydride-ion diffusion in the oxyhydride of barium titanate**

R. Lavén, L. Fine, E. Naumovska, H. Guo, U. Häussermann, A. Jaworski, M. Matsuura, M.M. Koza, and M. Karlsson

*Under review in The Journal of Physical Chemistry C*

Publications I contributed to during the PhD and not included in the thesis:

**Growth and thermal stability of Sc-doped  $\text{BaZrO}_3$  thin films deposited on single crystal substrates**

G. K. Nzulu, E. Naumovska, M. Karlsson, P. Eklund, M. Magnuson, and A. le Febvrier, *Thin Solid Films* 2023, 772, 139803

**Differences in interaction of graphene/graphene oxide with bacterial and mammalian cell membranes**

V. Lanai, Y. Chen, E. Naumovska, S. Pandit, E. Schröder, I. Mijakovic, and S. Rahimi *Nanoscale*, 2024, 16(3), 1156-1166

# Contribution report

My contributions to the included papers:

**I** I was the main responsible for the analysis of the experimental data. I was the main responsible for writing the manuscript. The data collection was performed by Johannes Orstadius as part of his Masters thesis. The samples were synthesized and characterized by collaborators at Chalmers University of Technology.

**II** I contributed to the planning of the QENS experiments and I was the main responsible for the data collection and analysis of the experimental data. I was the main responsible for writing the paper. The experiment was performed remotely due to travel restrictions imposed by the COVID pandemic. The samples were synthesized and characterized by collaborators at University of Verona.

**III** I contributed to the planning and execution of the experiments and I was the main responsible for the experimental data collection and analysis of the experimental data. I was the main responsible for writing the manuscript. The samples were synthesized and characterized by collaborators at Linköping University.

**IV** I was responsible for the synthesis and characterization of the  $\text{BaTiO}_{2.88H0.12}$  sample. I contributed to the manuscript writing. The QENS experiments and data analysis were performed by Rasmus Lavén and Lucas Fine.

*To my grandparents Dr. Milorad Mladenovic & Dr. Leposava Mladenovic  
Semper amati, semper desiderati.  
Primum non nocere...*



---

# Contents

<b>1</b>	<b>From materials to sustainable energy solutions</b>	<b>1</b>
<b>2</b>	<b>Proton- and hydride ion conducting oxides</b>	<b>7</b>
2.1	Proton-conducting oxides . . . . .	7
2.2	Perovskite-type oxides . . . . .	10
2.2.1	Structure and proton incorporation . . . . .	10
2.2.2	Local structure and proton sites . . . . .	11
2.2.3	Proton mobility . . . . .	11
2.3	Brownmillerite-type oxides . . . . .	13
2.3.1	Structure and proton incorporation . . . . .	13
2.3.2	Local structure and proton sites . . . . .	14
2.3.3	Proton mobility . . . . .	15
2.4	Hydride ion-conducting oxides . . . . .	16
2.5	Perovskite-type oxyhydrides . . . . .	16
2.5.1	Structure and hydride-ion incorporation . . . . .	16
2.5.2	Hydride-ion dynamics . . . . .	18
2.6	Concluding remarks and scope of thesis . . . . .	19
<b>3</b>	<b>Materials synthesis</b>	<b>21</b>
3.1	Proton-conducting oxides . . . . .	21
3.2	Hydride-ion conducting oxides . . . . .	23
<b>4</b>	<b>Experimental techniques</b>	<b>27</b>
4.1	Neutron scattering . . . . .	27
4.1.1	Foundation and mathematical background . . . . .	27
4.1.2	Quasielastic neutron scattering . . . . .	30
4.1.3	Inelastic Neutron Scattering . . . . .	32
4.2	Infrared spectroscopy . . . . .	34
4.3	Other techniques used in this thesis . . . . .	35
4.3.1	Thermogravimetric analysis . . . . .	35
4.3.2	Nuclear Reaction Analysis . . . . .	36
4.3.3	Powder X-ray diffraction . . . . .	37
4.3.4	Energy dispersive spectroscopy . . . . .	38

<b>5</b>	<b>Instruments</b>	<b>39</b>
5.1	Quasielastic neutron scattering . . . . .	39
5.2	Infrared spectroscopy . . . . .	41
5.3	Thermogravimetric analysis . . . . .	43
<b>6</b>	<b>Overview of Findings</b>	<b>45</b>
6.1	Unraveling the effect of doping concentration on local structure and dynamics . . . . .	45
6.2	Elucidation of the relationship between type of dopant atom and local structure and dynamics . . . . .	49
6.3	Local structure and dynamics in perovskite-type oxyhydrides . . . . .	52
<b>7</b>	<b>Conclusions and outlook</b>	<b>55</b>
	<b>Appendix A</b>	<b>59</b>
	<b>Appendix B</b>	<b>61</b>
<b>8</b>	<b>Bibliography</b>	<b>65</b>

---

## List of abbreviations

BZO	Barium zirconate
BIO	Barium indate
EISF	Elastic incoherent structure factor
FWHM	Full width at half maximum
IR	Infrared
ILL	Institut Laue-Langevin
MD	Molecular dynamics
NRA	Nuclear reaction analysis
QENS	Quasielastic neutron scattering
SNS	Spallation Neutron Source
TGA	Thermogravimetric analysis
TOF	Time-of-flight



---

# From materials to sustainable energy solutions

I believe that water will one day be employed as fuel,..., that will furnish an inexhaustible source of heat and light.

---

*Jules Verne*

The climate crises and the demand for lowering gas emissions (e.g. CO<sub>2</sub>) [1], presents both a challenge and a unique opportunity to develop technologies which can promote the green energy transition to a more environmental and sustainable society.

Reducing the dependency of fossil fuels and transitioning to energy from renewable sources, or "green energy", can significantly help preserve natural resources, biodiversity, and ecosystems, all of which are endangered by the extraction and transportation of fossil fuels [1–3]. This is particularly important as a recent report highlighted that human activities have breached six out of the nine planetary boundaries essential for the stability and resilience of the Earth system [1, 4].

As opposed to fossil fuels which are the primary contributors to CO<sub>2</sub> emissions which directly contribute to climate change and global warming [1–3], "green energy" devices generate no or almost no greenhouse gas emissions when producing electricity; examples of such devices are solar panels, which produce electricity from sunlight with no emissions, wind turbines, which generate electricity from wind without fossil burning, water turbines, which generate electricity from water, and fuel cells, which produce electricity with (clean) water as side product [1, 5, 6].

The transition to green energy and the use of green energy devices are, however, subject to several challenges. While many of these challenges are related to policy and economic factors [2, 3, 7], a key challenge lies in the industrialization of these devices [8–11].

Fuel cells are considered a particularly promising device for electricity generation in a non-polluting way, and there are a number of applications based on fuel cells developed so far which directly support the United Nations Sustainable Development Goals by enabling clean, reliable, and sustainable energy solutions (Figure 1.1) [10, 12–15].

There are different types of fuel cells (already) available, such as the molten carbonate fuel cell, the phosphoric acid fuel cell, the proton-exchange membranes fuel cell (PEMFC) and the solid oxide fuel cell (SOFC) [16–19]. Among these, PEMFCs and SOFCs are unique because they are entirely solid-state devices, which eliminate issues such as electrolyte leakage and corrosion [16, 18, 19].

PEMFCs operate at relatively low temperatures, from room temperature up to about 80 °C. This allows for quick startup times, making them well-suited for use as power sources in electric

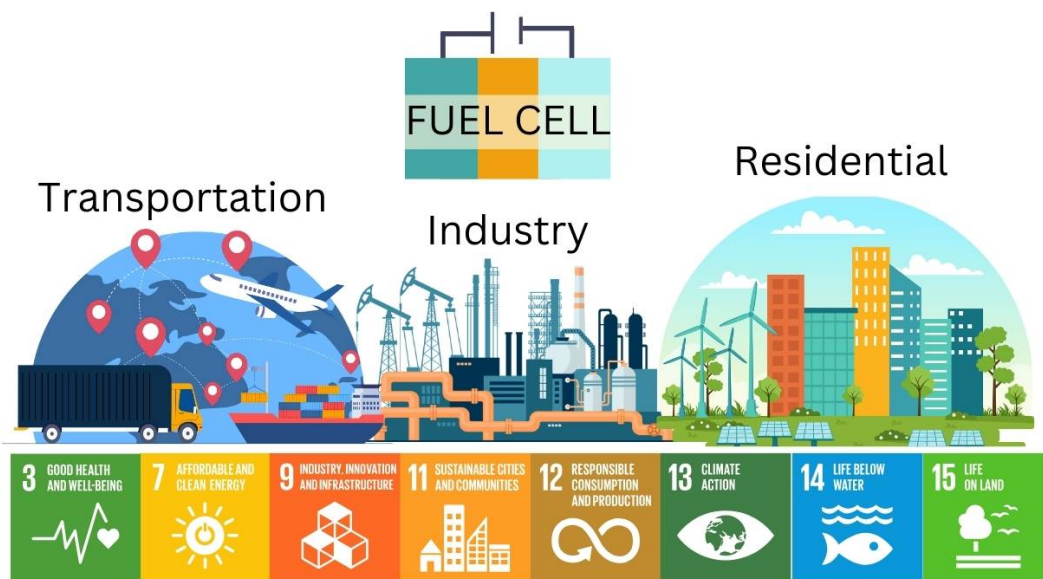


Figure 1.1: Illustration of applications of fuel cells for primary and backup power of residential and industrial buildings, and power of vehicles. Contribution as per United Nations Sustainable Development Goals. Designed by Freepik, slidesgo/Freepik, and macrovector/Freepik.

vehicles [16, 20, 21]. However, their low operating temperature requires the use of expensive precious metal catalysts like platinum, which significantly increase the cost of devices. Additionally, PEMFCs require pure hydrogen as fuel [16, 22]. In contrast, SOFCs operate at much higher temperatures up to 1000 °C [16, 23, 24]. These elevated temperatures speed up the electrode reactions, allowing SOFCs to function efficiently without the need for precious metal catalysts [16]. The high operating temperature also grants SOFCs greater fuel flexibility; they can use not only fossil fuels, but also renewable biomass as fuel sources [16, 24].

A typical SOFC single cell consists of three main layers arranged in a sandwich-like structure: a porous oxide-based cathode, a dense ceramic electrolyte, and a porous ceramic-metal composite anode, as shown in Figure 1.2 [16, 19, 24]. The electrolyte is positioned between the cathode and anode. Unlike traditional chemical redox reactions, where oxidants and reductants come into direct contact, in a SOFC these reactants do not touch directly [16, 19, 24]. Instead, the fuel undergoes an electrochemical oxidation at the anode, releasing electrons that travel through an external circuit to the cathode. At the same time, oxygen molecules are reduced at the cathode via the electrochemical oxygen reduction reaction. The electrolyte facilitates the transfer of ions (*e.g.* protons) from one side of the cell to the other (from the anode for oxygen ions or from the cathode for protons) through its solid structure, completing the electrochemical process [16, 19, 24].

The electrolyte plays several critical roles: first, it acts as a physical barrier to prevent direct mixing of fuel and oxidant, so it must be fully dense; second, it serves as an electronic insulator, blocking electron flow through the solid and ensuring that electrons only move through the external circuit to generate electricity. Finally, the electrolyte also serves as a supporting substrate for both electrodes, which means that its mechano-thermal properties should be well matched with those

of the electrodes [11, 16, 24]. In a SOFC, the properties of the electrolyte influence the reaction pathways, affect overall stability, impact mechanical performance, and set the operating temperature of the entire cell. Since the electrolyte is exposed to the atmospheres of both the anode and cathode, it must exhibit high chemical stability across a wide range of oxygen partial pressures [6, 16].

The current SOFC technologies typically consist of an oxygen-ion conducting yttria-stabilized zirconia electrolyte [12, 23, 25, 26]. These cells usually operate at temperatures above 800 °C to achieve optimal power output [16]. However, it is now widely recognized that lowering the operating temperature to the intermediate range of 200–400 °C is crucial for promoting a broader adoption of the SOFC technology [16]. Lowering the high operating temperature range of fuel cells to 200–400 °C comes with several opportunities, such as faster startup times, prolonged lifespan and decreased mechanical stress on the components caused by thermal expansion, when compared to traditionally used SOFCs, as well as application of a wider range (and cheaper) materials [8, 9, 16] when compared to PEMFCs [22].

To overcome these challenges, the development of new electrolyte materials optimized for operation in the intermediate temperature range of 200–400 °C is necessary [16, 19, 27]. Over recent years, significant efforts have been made to identify and improve such materials to enable efficient and reliable SOFC performance within the intermediate temperature range. To be applied in fuel cell, however, the materials' proton conductivity must be rationally increased to at least  $10^{-2}$  S/cm within this temperature range [28].

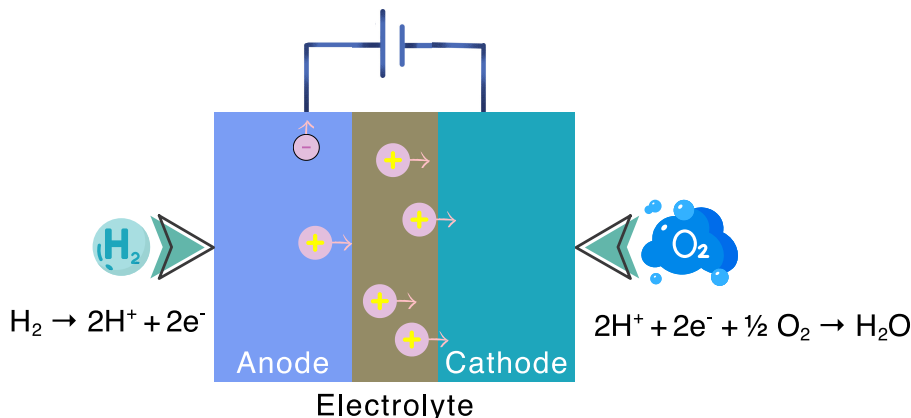


Figure 1.2: Schematic drawing of a SOFC with a proton-conducting electrolyte.

Proton-conducting oxides with the  $ABO_3$  type<sup>1</sup> perovskite structure are widely recognized as the most promising materials for the application as electrolytes in SOFCs [10]. Currently, state-of-the-art materials, such as  $BaZrO_3$  and  $BaCeO_3$  based compounds, exhibit proton conductivities ranging from  $10^{-7}$  S/cm to  $10^{-2}$  S/cm within the temperature window of 200–400 °C [8, 29–32]. In the past decade, an extensive amount of research has been focused on increasing the proton conductivity in these materials [14, 15, 29, 29, 31, 33–46]. To do that, researchers have explored a wide range of strategies, including the development of new compositions based on the perovskite structure and on tuning the proton conductivity [8, 9, 14, 29, 47–49]. Construction engineering approaches have been used in optimizing the microstructure and grain boundaries to facilitate proton transport [8, 9, 50, 51]. The application of different dopant atoms, polymers, and nanostructuring, have been also extensively studied to identify those materials with superior conductivity [52–54].

<sup>1</sup>The  $ABO_3$  type proton-conducting oxides belong to a wider class of materials with general formula  $ABX_3$ , where A and B are cations, and A is usually larger in size than B, and X is usually an oxygen.

Research efforts have also been focused on broadening the research on materials beyond perovskite-based proton conductors, with hopes to include a wider variety of materials that can enhance the operational conditions of intermediate-temperature SOFCs [55–59]. Moreover, advanced computational techniques, including molecular dynamics simulations and artificial intelligence, have been employed to predict material behavior, optimize compositions, and accelerate the discovery of high-performance proton conductors [56, 57]. Hence it remains to be elucidated *how specific compositional and structural modifications influence the proton conduction mechanisms at the atomic level*. Understanding this will open a pathway that governs proton mobility resulting in a rational design of materials with tailored properties, ultimately leading to more efficient, durable, and cost-effective proton-conducting materials for practical applications. Addressing this question will also enable for a targeted engineering of materials that meet the demanding requirements of next-generation energy devices.

With a view towards SOFC electrolytes based on materials beyond proton-conducting oxides, there is an increasing trend of investigations on hydride-ion conducting oxides. Recently, for example,  $\text{La}_{1-x}\text{Sr}_x\text{H}_{3-x-2\gamma}\text{O}_\gamma$  was shown to exhibit a high hydride-ion conductivity of  $10^{-5}$ – $10^{-4}$  S/cm, depending on concentration of strontium ( $x$ ) and oxygen ( $\gamma$ ) at room temperature [60]. This demonstrated a true milestone in the field of materials science and increased the interest in hydride-ion conducting oxides for applications in SOFCs. Another interesting class of hydride-ion conductor is the oxyhydride of  $\text{BaTiO}_3$ , which gained significant attention due to its conductivity between  $10^{-4}$  S/cm and  $10^{-3}$  S/cm at room temperature [61]. Interestingly, it was also found that the presence of oxygen vacancies, or the lack thereof, has a significant influence on the hydride-ion diffusion and its conductivity [62, 63]. Research into hydride-ion perovskite-type oxides is still emerging, but advances in synthesis techniques that enable precise control over their structures (in terms of oxygen vacancy and hydride-ion concentration) remains a challenge [64–69]. Synthetically, there are various pathways to explore. A key requirement for the synthesis process, however, is the need for strong reducing conditions [64, 65]. This creates complexities, as the reducing conditions pose a significant risk of unwanted reduction of the cations to their metallic state; additionally, the synthesis often requires extreme conditions such as high temperatures, high pressures, or specialized atmospheres to stabilize the desired phases, which complicates reproducibility and scalability [65, 70–75]. An open research question in this context is: *how can synthesis methods be optimized to reliably produce phase-pure, stable perovskite oxyhydrides with controlled compositions and vacancies?* Addressing this question involves exploring novel synthesis routes, such as low-temperature techniques, alternative precursor materials, or different atmospheres that facilitate the incorporation of hydride ions without degrading the phases. Understanding the fundamental parameters that influence phase stability, ion mobility, and defect formation during synthesis is crucial for advancing the field.

While there is an enormous progress that has led to the industrialization of some materials, the journey of finding the ideal material which will revolutionize the field (in terms of fabrication, stability and efficiency of devices) of fuel cells continues [9, 59, 76, 77]. Additionally, there is a significant need in more fundamental studies because they provide the foundational knowledge needed to tailor synthesis processes and to rationally improve material properties. Investigating the mechanisms of hydride and proton incorporation, diffusion pathways, and the local structure can reveal insights that can benefit the field of ion-conductors, not only by developing new classes of materials, but also by application in innovative solutions across multiple technological fields [64, 65]. Such studies can also elucidate the relationships between local structure, composition, and functional properties, ultimately guiding the design of new materials with enhanced performance for applications in energy storage, catalysis, or electronics [8, 63, 65, 78–81].

## Motivation and research questions addressed in this thesis

Motivated by the current need for developing new, better performing proton- and hydride-ion conducting materials for "green energy" applications, this thesis focuses on investigations of fundamental key aspects of structure and dynamics in some archetypal proton- and hydride-ion conducting perovskite oxides. These materials are proton-conductors of Sc-doped  $\text{BaZrO}_3$  and  $\text{Ba}_2\text{In}_{1.85}\text{M}_{0.15}\text{O}_5$  ( $\text{M} = \text{In}, \text{Ga}, \text{Sc}$  and  $\text{Y}$ ), and hydride-ion conductors based on  $\text{BaTiO}_3$  and In-doped  $\text{BaZrO}_3$ . The research has been experimental in nature and the primary tools to this end have been quasielastic neutron scattering and infrared spectroscopy. The open research questions explored and addressed through this thesis are as follows:

### Proton-conducting oxides

- What is the relationship between the doping concentration and the dynamics of protons, its activation energy, timescale and geometry in Sc-doped  $\text{BaZrO}_3$  powders? Does it differ? How?
- Is the local proton environment similar in Sc-doped  $\text{BaZrO}_3$  films and powders? Does it differ? Why?
- What are the effects of different dopants on the proton environments, proton diffusion, its timescale, and geometry of motion in  $\text{Ba}_2\text{In}_{1.85}\text{M}_{0.15}\text{O}_5$ ,  $\text{M} = \text{In}, \text{Ga}, \text{Y}$ , and  $\text{Sc}$ ?

### Hydride-ion conducting oxides

- What synthesis parameters in  $\text{ATiO}_3$ ,  $\text{A} = \text{Ba}, \text{Sr}, \text{Ca}$  perovskites influence the hydride-ion incorporation and concentration? Does it change when using different reducing agents? Does it differ? How?
- How does the presence of oxygen vacancies influence the hydride-ion dynamics in  $\text{BaTiO}_3$  oxyhydrides? Does it differ? How?
- What is the relationship between the In doping concentration and the incorporation of hydride-ions in In-doped  $\text{BaZrO}_3$  perovskites?
- How can we optimize the synthesis routes for design of existing and new classes of perovskite oxyhydrides? Can we make it suitable for large-scale industrial applications having also in mind the economic and time parameters? How?

The ultimate aim is to develop the understanding needed to rationally propose new materials with higher proton or hydride-ion conductors based on the perovskite structure.



---

# 2 Proton- and hydride ion conducting oxides

All innovation begins with curiosity.

---

*Jen Keane*

## 2.1 Proton-conducting oxides

<sup>1</sup> The introductory chapter of this thesis highlighted the importance of developing new proton- and hydride-ion conducting oxides with higher conductivity for application in intermediate temperature SOFCs. From a material point of view, research on proton conducting oxides started already in the 1960s, inspired by the proton-conducting polymer Nafion<sup>®</sup>, which was used in a polymer electrolyte fuel cell in the Gemini and Apollo space programs as a source for onboard electric power, operating at temperatures below 100 °C [35]. In the 1980s, Iwahara and his team published the first findings on high-temperature proton-conducting oxides that functioned between 800 and 1000 °C, marking significant advancement in this field [82].

Figure 2.1 shows the conductivity of the (so far) best performing proton-conducting oxides along with some of the best materials used in low and high temperature fuel cells respectively [83–85]. Note, there is a "gap" of materials with high conductivity (here  $> 10^{-2}$  S/cm) in the intermediate temperature range between 200 °C and 400 °C [28]; which is the reason as to why intermediate temperature SOFCs have not yet been developed. The most promising materials that can potentially fill in this gap are based on perovskite-type BaCeO<sub>3</sub>, BaZrO<sub>3</sub>, and Ba<sub>2</sub>In<sub>2</sub>O<sub>5</sub> [77].

In more detail, BaCeO<sub>3</sub> is known for its high proton conductivity at elevated temperatures [8, 27, 37–40, 86]. Cation substitution with trivalent atoms on the Ce site (doping) in BaCeO<sub>3</sub> was found to enhance its conductivity; for example, doping 10–15% with Y was shown to give a maximal proton conductivity in the range of 0.01 and 0.12 S/cm at temperatures between 500 and 600 °C [37–40]. Co-doping strategies with different elements have also been explored to further improve stability and proton transport [8, 54, 86]. Nonetheless, BaCeO<sub>3</sub>-based materials face limitations due to chemical instability in the presence of CO<sub>2</sub> and steam, leading to decomposition [8, 76, 77]. To address this, researchers started investigating alternative materials with the same structure, but with better chemical resilience and higher proton conductivity. Materials based on BaZrO<sub>3</sub> have been found to have exceptional chemical stability across various environments, including those

---

<sup>1</sup>This chapter is partially based on my Licentiate thesis [1].

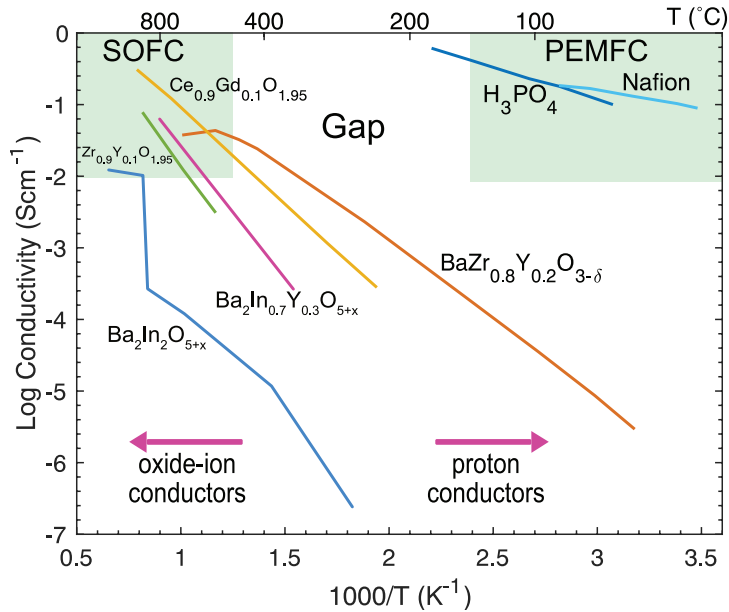


Figure 2.1: Ionic conductivity of some of the best ionic conductors together with the operation ranges of low temperature proton-exchange membrane fuel cells (PEMFCs) and high temperature solid oxide fuel cells (SOFCs) (green), respectively. The figure is modified as per data from [83–85].

containing  $\text{CO}_2$  and  $\text{H}_2\text{S}$ , over a wide temperature range [31, 33–36, 49]. Numerous studies showed that partial doping on the Zr site, between 10% and 20%, with different rare earth metals such as Sc, In, La, Y, and Fe, leads to high proton conductivities in the intermediate temperature range, with Y being the dopant atom which corresponds to highest conductivity in the range between  $10^{-3}$  and  $3.3 \cdot 10^{-2}$  S/cm [14, 15, 29, 41–45]. Interestingly, it was showed that doping with Ga corresponds to lowest proton conductivity at the investigated temperature range [87–89]. Recently, significant higher proton conductivity by two orders of magnitude up to  $10^{-2}$  S/cm at  $396^\circ\text{C}$  was discovered in  $\text{BaZrO}_3$  when replacing 60% of Zr with Sc, as opposed to the same system with only 20% Sc doping [46]. Moreover, exceptionally good properties in terms of conductivity, and chemical stability in water and carbon dioxide atmospheres were reported for  $\text{BaZrO}_3$  systems co-doped with Y and Pr or Nd [14, 29]. Various doping and synthesis strategies have been adopted with the aim to increase proton conductivity in these systems. As a notable example, compositions such as  $\text{BaCe}_{1-x-y}\text{Zr}_x\text{Y}_y\text{O}_{3-\delta}$ , recently gained considerable attention due to the high proton conductivity in the range of up to  $9 \cdot 10^{-3}$  S/cm at  $500^\circ\text{C}$  and good chemical stability [9, 90]. Furthermore, donor doping the oxygen-deficient  $\text{BaScO}_{2.5}$  with  $\text{Mo}^{6+}$  to form  $\text{BaSc}_{0.8}\text{Mo}_{0.2}\text{O}_{2.8}$  achieved conductivities up to  $10^{-2}$  S/cm at  $320^\circ\text{C}$  with enhanced stability [9, 91].

Beyond the  $\text{ABO}_3$ -structured perovskite, the brownmillerite  $\text{Ba}_2\text{In}_2\text{O}_5$ , traditionally known as an oxide-ion conductor, gained considerable attention due to its ability to incorporate protons, and thus become a proton-conducting oxide [13, 84, 85, 92, 93]. For instance, the brownmillerite  $\text{Ba}_2\text{In}_2\text{O}_5$  exhibits a proton conductivity between  $10^{-6}$  and  $10^{-5}$  S/cm at temperatures between  $400^\circ\text{C}$  and  $500^\circ\text{C}$  [84, 94]. Doping  $\text{Ba}_2\text{In}_2\text{O}_5$  with 20% Yb on the In site was found to result in an increased proton conductivity to  $1.7 \cdot 10^{-3}$  S/cm [95]. Recently, it was also reported that increased proton conductivity of the  $\text{Ba}_2\text{Sc}_2\text{O}_5$  brownmillerite system was achieved by replacing the traditionally used solid state synthesis route with high pressure synthesis [96]. The obtained proton

concentration of these materials was reported to be 10 times higher than, for instance, the best acceptor doped barium zirconates [96].

It is worth pointing out that the proton conductivities reported for these materials often vary widely due to differences in study conditions, chemical compositions, microstructural properties, and manufacturing processes, making it difficult to definitively identify the best performers [8]. Proton conductivity can also depend heavily on environmental conditions; factors such as temperature and humidity significantly influence conductivity [8, 9]. Furthermore, from a thin film point of view, comparative data indicate that, at temperatures between 500 °C and 700 °C, 20% Y-doped BaZrO<sub>3</sub>-based electrolytes show the lowest conductivity up to  $6 \cdot 10^{-3}$  S/cm [8], compared to the same material in a powder form with conductivity up to  $3.3 \cdot 10^{-2}$  S/cm, indicating that different structural effects affect the proton conductivity in the films. Hence, it is clear that the rational increase of the proton conductivity in these proton-conducting perovskites relies on a deeper understanding of the structure-conductivity relationships in the most promising materials. By gaining insights into how structural characteristics influence proton conduction, it becomes possible to design materials with specific structures to achieve improved proton conductivity. The research efforts within the field of proton-conducting oxides is summarized in Figure 2.2.

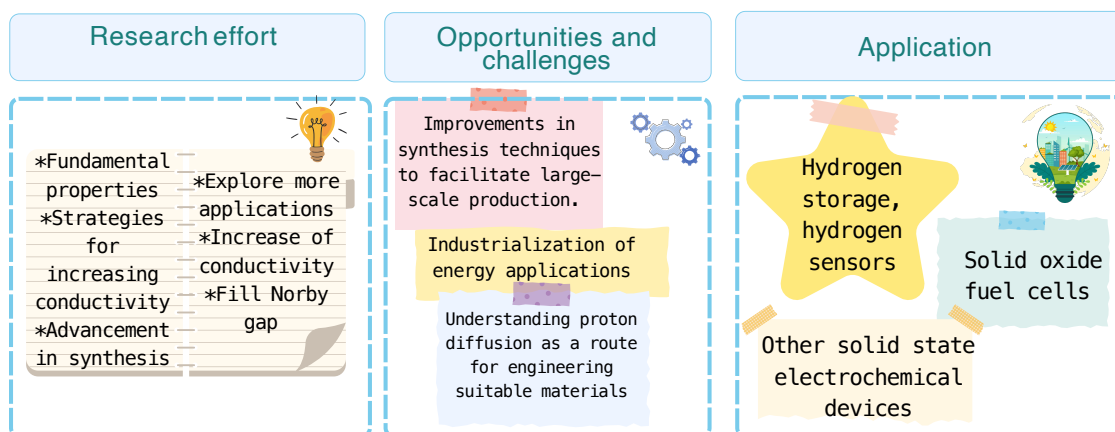


Figure 2.2: Schematic drawing and a summary of focus areas related to proton-conducting oxides, including current and future research efforts, application and opportunities and challenges within the field. The figure is modified as per data from [9].

## 2.2 Perovskite-type oxides

### 2.2.1 Structure and proton incorporation

Perovskite-type oxides based on  $\text{BaZrO}_3$  and  $\text{BaCeO}_3$ , belong to the wider class of materials with general formula  $\text{ABX}_3$ . The Ba cations occupy body centered positions, whereas the oxygen atoms are at the center of each plane of the cube, forming an octahedron; the Zr (or Ce) cation is placed at the center of this octahedron [97, 98]. Protons are not part of this structure, and in order to be incorporated, defects need to be created in the, otherwise, "perfect" cubic structure [97, 98]. Traditionally, this is achieved by cation substitution of Zr (or Ce) with lower-valent (trivalent) dopant atoms with ionic radii that roughly match the one of the cation, and thus creating oxygen vacancies for charge compensation.<sup>2</sup> The newly created oxygen deficient material is then exposed to hydration, where the water dissociates in a way that the hydroxide ion fills the oxygen vacancy and the proton forms a covalent bond to the oxide ion. Accordingly, the concentration of protons will be proportional to the doping concentration, for a fully hydrated system. As an example, a schematic drawing of the crystal structure, doping and proton incorporation for  $\text{BaZrO}_3$  is presented in Figure 2.3.

For the purpose of this study, hydrated forms of powder and film samples were prepared by annealing as-prepared powders and films in a tube furnace subjected to a mixture of nitrogen and water vapor environment, while cooling from 600 to 200 °C at a rate of 0.2 °C/min. For further details related to the incorporation of protons, see Appendix B. It is important to note that the degree of hydration reported in the literature for acceptor-doped  $\text{BaZrO}_3$  spans a wide range, from 60% to 100% [41, 99–105]. A low hydration degree is an indication of some unfilled oxygen vacancies, which further indicates that there is an uneven, potentially preferred distribution of protons within the material. The reason for a low hydration degree, or its relationship with proton conductivity is unknown.

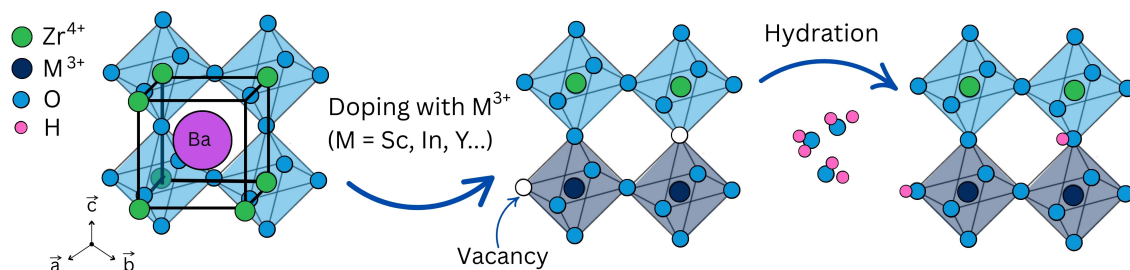


Figure 2.3: Schematic drawing of acceptor doping and proton incorporation in  $\text{BaZrO}_3$ . Doping with trivalent atoms creates oxygen vacancies; upon hydration the water dissociates into hydroxyl groups which fill the oxygen vacancies and protons are incorporated in the structure.

<sup>2</sup>Substitution of the B<sup>4+</sup> cation with lower-valent M<sup>3+</sup> atoms (acceptors) is also known and hereafter referred to as acceptor doping, or simply doping.

## 2.2.2 Local structure and proton sites

Once protons are incorporated into the  $ABO_3$  material, it is crucial to elucidate their local environment, also known as proton sites. The fundamental concept is that a proton upon being introduced in the material forms a covalent bond to an oxygen atom, here called O(1). The proton can likewise form a hydrogen bond to a neighboring oxygen atom, here called O(2). Due to the presence of dopant atoms, the protons can occupy different sites. For instance, the proton can be located between two B-site ions, or between two dopant atoms, which are here referred to as symmetrical sites. The proton can likewise be located between a dopant atom and a B-site ion, here referred to as asymmetrical sites. Schematic illustrations of these different proton sites are shown in Figure 2.4.

Several studies revealed that the size of the dopant atom plays a significant role in the local environment of the protons. Dopant atoms similar in size to the B-site ion result in the creation of a structural effect which promotes hydrogen bonding by tilting the proton towards the neighboring oxygen, which is especially evident for asymmetrical sites. On the contrary, a dopant atom larger in size than the B-site ion, results in a distortion of the local structure around the dopant, which can limit the degree of hydrogen bonding [106, 107].

Understanding the nature of proton sites is essential for investigating and developing a fundamental understanding of the relationship between proton dynamics and the underlying mechanisms governing proton conduction in these materials.

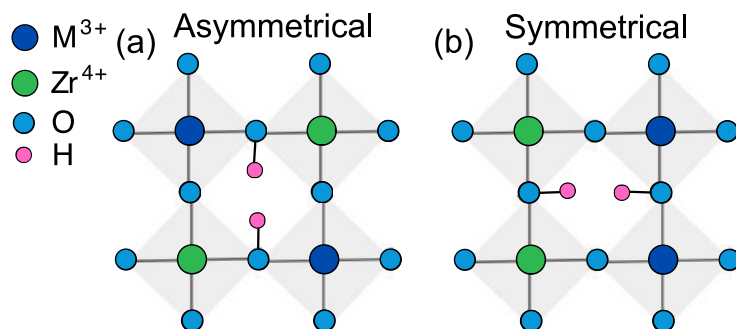


Figure 2.4: Schematic drawing of proton sites for an acceptor doped perovskite (ab plane). An asymmetrical site refers to proton site between a B-site cation (e.g. Zr) and a dopant atom M, represented as green and dark blue circles, respectively (a). A symmetrical site refers to a proton site between two identical cations (B or M) (b).

## 2.2.3 Proton mobility

The nature of proton conduction in proton-conducting perovskite type oxides has been extensively studied from both theoretical and experimental point of views, however, how the proton moves and how it is affected by structural properties such as the type and concentration of dopant atoms is not fully understood [49, 108–110].

Theoretically, the proton diffusion in acceptor doped  $BaZrO_3$  systems can be geometrically divided into two elementary, short-range (localized), dynamic processes: a transfer (jumps) of the protons between two oxygen atoms and rotational motions of the  $-OH$  group [Figure 2.5 (a) and (b)] [111–118]. This type of localized diffusion is strongly dependent on the hydrogen bond formation and breaking. In a more comprehensive manner, transfer from one to another oxygen atom requires a formation of a new covalent O–H bond and a new hydrogen bond [119]. Rotational motions of

the  $-OH$  group require breaking of the hydrogen bond. While the transfer process is associated with the overcoming of the energy barrier between the two sites, the rotational process is associated with the energy needed to break the hydrogen bond. A series of these processes leads to long-range diffusion [Figure 2.5 (c)].

There have been extensive discussions on which of the two fundamental transport steps is more energy consuming, or, in other terms, which of the two processes is the rate-limiting for long-range diffusion [107, 113, 120, 121]. In more detail, it has been found that the proton mobility is strongly influenced by structural and chemical distortions introduced with dopant atoms, although the actual reason for this is still unclear [122–125]. In more detail, when in asymmetric proton environments, the  $-OH$  group tilts towards the dopant atom, resulting in shortening of the oxygen-oxygen distance and stronger hydrogen bonding. Although this is advantageous for the proton transfer step, it can hinder the rotational process which requires breaking of hydrogen bonds [107, 112]. Multiple studies have provided evidence that the rotational process is faster than the transfer process [111, 120, 126]. However, some research indicates that the two processes might have comparable rates [102, 127], while others propose that the rotational process could actually be the rate-limiting for long-range diffusion [128].

Studies of  $BaZrO_3$ -based materials doped with up to 20% of Y, In, and Sc on the Zr site, based on neutron scattering, ascribed the localized proton diffusion to contributions of both proton transfers and rotational motions with comparable timescales up to 30 ps, and activation energies below 100 meV [58, 115, 116, 129–131]. Higher doping concentrations, which could provide more information regarding their influence on the localized proton diffusion, however, are to be obtained. Nevertheless, since it has been difficult to separate the contributions from proton transfer and  $-OH$  rotational diffusion in the analysis of experimental data based on neutron scattering, no understanding on which process (transfer or rotation) is the rate-limiting, and which promotes long-range diffusion has been reached so far [115, 116, 129, 130].

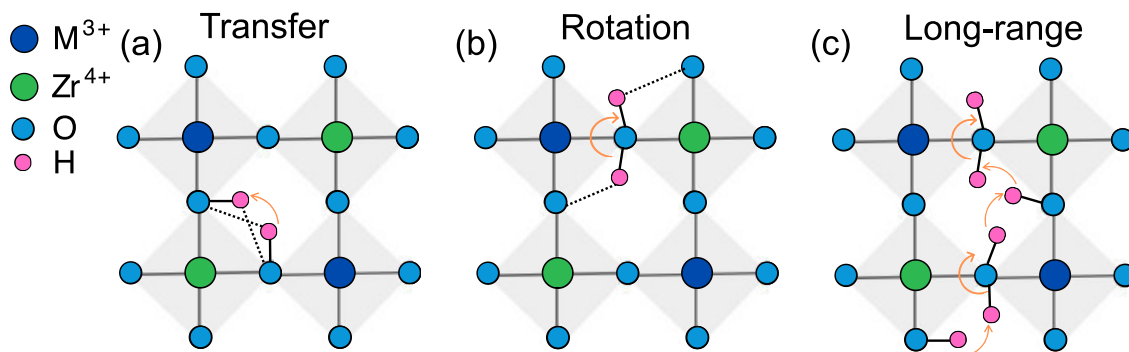


Figure 2.5: Schematic drawing of proton transfer (a), proton orientation (b), and long-range diffusion (c) for an acceptor doped perovskite (ab plane). The arrows indicate the pathway of the proton.

## 2.3 Brownmillerite-type oxides

### 2.3.1 Structure and proton incorporation

The brownmillerite structure,  $A_2B_2O_5$ , and specifically the material  $Ba_2In_2O_5$ , is a well-known oxide-ion conductor. It can be considered as an oxygen-deficient variant of the perovskite-structure, and it is composed of  $InO_6$  octahedral layers and  $InO_4$  tetrahedral layers, with Ba atoms placed in between, as well as oxygen vacancies arranged along the  $[0\ 1\ 0]$  direction as shown in Figure 2.6 [92, 93, 129, 132].

In addition to being an oxide-ion conductor, the brownmillerite  $Ba_2In_2O_5$  undergoes a structural transformation in humid atmosphere at about 300 °C resulting into the proton-conducting system  $Ba_2In_2O_5(H_2O)_x$  [84, 133]. Here  $x$  can be between 0 (dehydrated) and 1 (fully hydrated). During hydration, the water molecules dissociate into hydroxyl groups which fill the tetrahedral layers and convert them in pseudo-cubic layers, (see Figure 2.6). The protons migrate into the not significantly distorted, cubic layers [13, 92, 93]. Similar as for the acceptor-doped perovskite-type oxides, a low hydration degree in  $Ba_2In_2O_5$  is an indication of unfilled oxygen vacancies. Cation substitution of  $Ba_2In_2O_5$  has been showed as a promising route to accommodate high proton conductivity [95, 129, 134]. Specifically,  $Ba_2In_{2-x}M_xO_5$  systems with partial ( $x = 0.15-0.35$ ) substitution of In for Sc and Y, showed increased proton conductivity up to  $5.4 \cdot 10^{-3}$  and  $2.0 \cdot 10^{-3}$  S/cm at 350 °C, respectively [134]. However, the relationship among the proton conductivity, local structure and proton environments, as well as the effect of the dopant atoms, has not been fully understood.

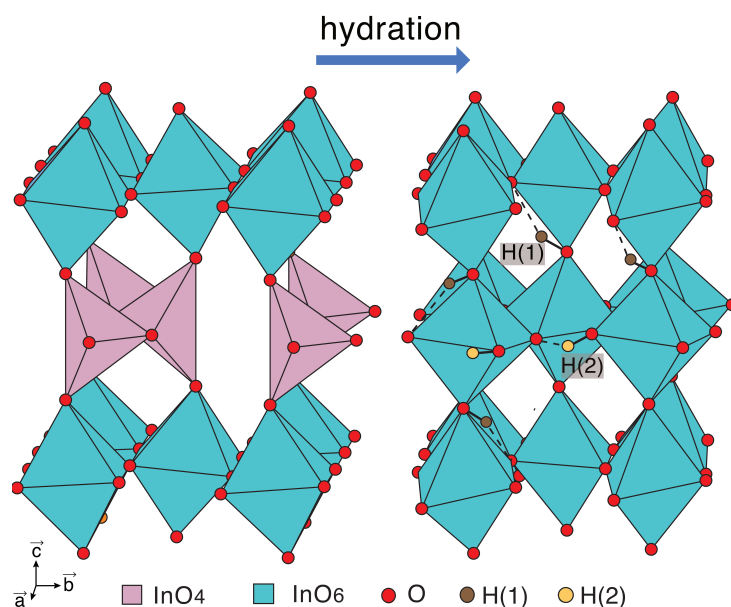


Figure 2.6: Schematic drawing of the dehydrated and fully hydrated form of  $Ba_2In_2O_5$ . Adapted from [129].

### 2.3.2 Local structure and proton sites

$\text{Ba}_2\text{In}_2\text{O}_5(\text{H}_2\text{O})_x$  is characterized primarily with two proton sites, H(1) and H(2), each featured by different local structural properties [92, 93, 129, 135–138]. The H(1) protons are bonded to the oxygen atoms that connect the  $\text{InO}_6$  octahedra with the middle layer consisted of the heavily distorted octahedra (i.e. the former tetrahedral layer). They also form hydrogen bonds with neighboring oxygen atoms. On the contrary, the H(2) protons are located solely in the middle layer of the heavily distorted octahedra, forming covalent bonds with oxygen atoms and hydrogen bonds with neighboring oxygen atoms within that same layer. The H(1) protons are, in general, characterized with much weaker hydrogen bonding compared to the H(2) protons, which are characterized with strong hydrogen bonding and much shorter oxygen-oxygen distances which, for 10% of the H(2) protons, can reach up to only 2.59 Å [129, 135]. Various cation substitutions on the In sites,  $\text{Ba}_2\text{In}_{1.85}\text{M}_{0.15}\text{O}_5(\text{H}_2\text{O})_x$  with  $\text{M} = \text{In}, \text{Ga}, \text{Sc}$  and  $\text{Y}$ , have been also investigated and showed a difference in the population of H(1) and H(2) proton sites [135]. Considering the  $\text{Ba}_2\text{In}_2\text{O}_5(\text{H}_2\text{O})_x$  as an equilibrium state, doping with smaller cations like Ga and Sc was shown to increase the population of the H(1) sites up to an equal distribution of protons within the two sites. On the contrary, doping with the larger Y cation, was shown to increase the population of the H(2) site. Similarly, for the Y doped system, increased presence of H(2) protons with unusually strong hydrogen bonding and, accordingly, a shorter oxygen-oxygen distance was observed [135].

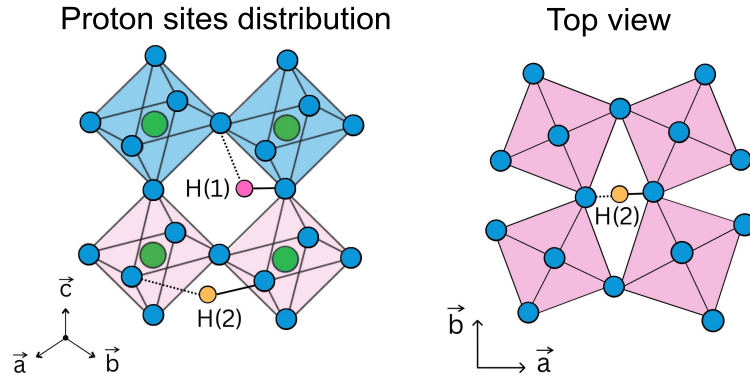


Figure 2.7: Schematic drawing of proton sites in hydrated  $\text{Ba}_2\text{In}_2\text{O}_5$ .

### 2.3.3 Proton mobility

Similar as for the acceptor doped perovskites, the proton conducting mechanism of brownmillerites such as  $\text{Ba}_2\text{In}_2\text{O}_6\text{H}_2$  may be divided into two localized motions, i.e., proton transfers from one to another neighboring oxygen and orientational motions of the  $-\text{OH}$  group [93, 129]. In more detail, results from neutron scattering and *ab initio* molecular dynamics (AIMD) data showed that the proton-conduction mechanism involves localized motions of the protons, distinguished as rotational diffusion of the  $\text{O}-\text{H}(1)$  species and  $\text{H}(2)$  proton transfers between neighboring oxygens, as shown in Figure 2.8 [129]. Interestingly, a third proton site,  $\text{H}(3)$ , which is found to become occupied upon increasing the temperature and that serves as a saddle state for the interexchange between  $\text{H}(1)$  and  $\text{H}(2)$  protons was observed [129]. Crucially, the occupation of the  $\text{H}(3)$  site was shown to promote long-range diffusion of protons [129]. The same study also observed that decreased proton concentration down to 30% results in an absence of long-range diffusion, likely due to hindered proton jumps in the vicinity of oxygen vacancies. Furthermore, cation substitution of  $\text{Ba}_2\text{In}_2\text{O}_6\text{H}_2$  has been shown to lead to a general increase of the proton conductivity of the material [88], which suggests that the proton conductivity may be directly linked to the relative occupation of the two types of proton sites,  $\text{H}(1)$  and  $\text{H}(2)$ , present. Motivated by these studies and with the hope to unravel the mechanistic details of proton diffusivity especially, in regard to the nature of localized  $\text{H}(1)$  and  $\text{H}(2)$  dynamics and how it depends on the type of dopant atom, this thesis reports on a study of the proton dynamics in hydrated  $\text{Ba}_2\text{In}_{1.85}\text{M}_{0.15}\text{O}_5$  with  $\text{M} = \text{In}, \text{Ga}, \text{Sc}$  and  $\text{Y}$ .

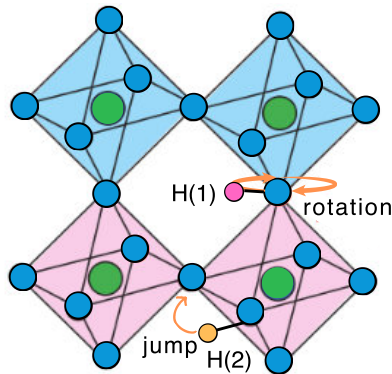


Figure 2.8: Schematic drawing of proton transfer and rotational motions, associated with the  $\text{H}(2)$  and  $\text{H}(1)$  sites, respectively.

## 2.4 Hydride ion-conducting oxides

Similarly to proton-conducting oxides, hydride-ion conducting oxides host hydrogen in the oxide structure, but now the hydrogen is in the form of a hydride species rather than protons.

Over the last decades, hydride-ion conduction has been extensively studied in materials such as LiH, CaH<sub>2</sub> and SrH<sub>2</sub> [139]. Research on hydride-ion conducting oxides was driven by the discovery of hydride-ion conduction in the layered perovskite oxyhydride LaSrCoO<sub>3</sub>H<sub>0.7</sub> [140], that could host both oxygen and hydride-ions in the structure. Since the discovery of LaSrCoO<sub>3</sub>H<sub>0.7</sub> research on oxyhydrides has advanced. Of specific concern in this thesis, the oxyhydride of BaTiO<sub>3-x</sub>H<sub>x</sub>, (with  $x$  values up to 0.6) was discovered in 2012 [66], which rejuvenated interest in the field, demonstrating that transition metals could stabilize hydride anions. The discovery also marked the first instance of an oxyhydride featuring the simple cubic perovskite structure.

In terms of hydride-ion conductivity, in the past few years, several oxyhydrides have shown high hydride-ion conductivity in the temperature range between 200 and 300 °C, making them promising candidates for application in intermediate-temperature fuel cells. In more detail, the oxyhydride La<sub>2</sub>Sr<sub>0.1</sub>LiH<sub>0.9</sub>O<sub>3</sub> exhibits hydride-ion conductivity as high as  $2 \cdot 10^{-5}$  S/cm for temperatures between 200 and 300 °C [139, 141]. The same study verified the performance of this material as an electrolyte in all-solid cell [139, 141]. The oxyhydride Ba<sub>1.75</sub>LiH<sub>2.7</sub>O<sub>0.9</sub> shows hydride-ion conductivity of  $10^{-2}$  S/cm at 300 °C [139, 142]. Further, the oxyhydride BaTiO<sub>3</sub>H<sub>x</sub> with  $x = 0.14$ - $0.35$ , shows a conductivity up to  $10^{-3}$  S/cm [61].

While oxyhydrides have demonstrated hydride-ion conductivity suitable for application in SOFCs, there is a lack of new oxyhydrides developed so far. Further advancement in synthesis techniques will allow for the exploration of a broader range of compositions, expanding the scope of materials available for study. It will also contribute to get a better, systematic-based understanding of hydride-ion conductivity mechanisms and advancement of new oxyhydride materials with enhanced properties for their final application.

## 2.5 Perovskite-type oxyhydrides

### 2.5.1 Structure and hydride-ion incorporation

Similarly to proton-conducting perovskites, the ABO<sub>3</sub> structure provides a straightforward structural framework which allows for application of different cations, resulting in materials with different properties [61, 64–66, 143]. For instance, the choice of A-site cations (such as Ba, Sr and Ca) in ATiO<sub>3</sub> oxyhydrides affects the temperature at which hydrogen is released, therefore directly influencing the mobility of hydride ions [143].

The ABO<sub>3</sub> oxyhydrides, and specifically BaTiO<sub>3-x</sub>H<sub>x</sub>, the O<sup>2-</sup> and H<sup>-</sup> ions create an octahedral arrangement around the Ti ions, resulting in Ti atoms with a mixed IV/III oxidation state [66–69]. This alteration in oxidation state leads to an expansion of the structure to accommodate an additional electron, which ensures that the material remains cubic across all temperatures, as compared to pure BaTiO<sub>3</sub> which is cubic only at temperatures above 396 K [144]. Introducing different A-site cations also results in different structural properties, as the size of the cation has a significant influence on the octahedral tilts and local environments in which the hydride ions are accommodated [62]. For example, at room temperature, CaTiO<sub>3-x</sub>H<sub>x</sub> and CaTiO<sub>3</sub> are orthorhombic, while SrTiO<sub>3</sub> and SrTiO<sub>3-x</sub>H<sub>3</sub> are cubic. Conversely, BaTiO<sub>3</sub> is tetragonal, whereas BaTiO<sub>3-x</sub>H<sub>x</sub> adopts a cubic structure. This change in symmetry for BaTiO<sub>3-x</sub>H<sub>x</sub> is attributed to the reduction

to  $\text{Ti}^{3+}$ , which cancels out the ferroelectric distortion [69, 80, 143]. In contrast,  $\text{CaTiO}_3$  and  $\text{SrTiO}_3$  are not ferroelectric; their orthorhombic structure results from tilting of the  $\text{TiO}_6$  octahedra, which remains largely unaffected by the Ti reduction [69, 80, 143]. Interestingly, the transition to an oxyhydride is likewise accompanied by a significant color change from white to dark blue [66, 69].

There are different methods for hydride-ion incorporation of  $\text{ABO}_3$  based oxyhydrides, based on different synthesis routes. Perhaps one of the most explored synthesis methods for hydride-ion incorporation is based on the topochemical route in which a reducing hydride agent is used for vacancy formation and hydride ion incorporation at elevated temperatures in an Ar atmosphere (see Figure 2.9 for a schematic description). While the first study based on topochemical synthesis reported a formation of a homogeneous  $\text{BaTiO}_{3-x}\text{H}_x$ , with  $x$  values reaching up to 0.6 [66], further studies showed quite distinctive results, where the  $\text{BaTiO}_3$  oxyhydride contains both oxygen vacancies and hydride ions up to 0.25 [145]. A higher hydride-ion concentration was obtained for the oxyhydride of  $\text{BaTiO}_{2.30}\text{H}_{0.70}$ , by selecting (100) centered  $\text{BaTiO}_3$  cubes as a starting material (precursor) [146]. The same study pointed out that the type of precursor, its crystalline size, as well as the synthesis method used for its production (such as solution-based or hydrothermal method), have a significant effect on the hydride-ion concentration [147]. Some studies have also shown that the selection of the reducing metal hydride ( $\text{CaH}_2$ ,  $\text{NaH}$ ,  $\text{LiH}$ ,  $\text{MgH}_2$ ) play a critical role in the synthesis and especially the formation of oxygen vacancies [69, 145]. Details regarding the hydride-ion incorporation with this method are provided in Appendix B. As a result of the challenges in incorporating a controlled hydrogen concentration associated with the topochemical reaction, several research studies focused on synthesis methods beyond the traditionally used one. The mechanochemical route attracted significant attention, as it allowed for a direct synthesis of  $\text{ATiO}_3$  materials by a simple utilization of mechanical energy for chemical reactions [147]. The reduction synthesis based on  $\text{H}_2$  gas was likewise explored as a synthesis route [70]. The hydrogen gas reduction route paved the way for the synthesis of a new class of oxygen-deficient perovskite-based oxyhydrides, such as  $\text{BaZr}_{0.50}\text{In}_{0.50}\text{O}_{2.75}$  oxyhydrides [70].

The journey of optimizing  $\text{ABO}_3$  oxyhydrides for enhanced functionality in fuel cells is still in progress. Although new materials are being developed, it is crucial to explore fundamental questions related to the synthesis methods employed, and the connections between the local structure, oxygen vacancies, and hydride-ion dynamics within this class of materials.

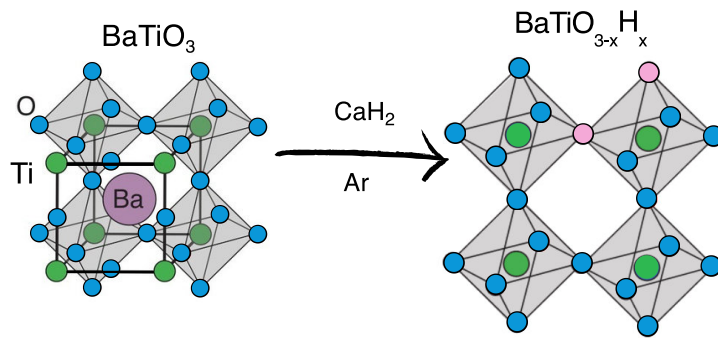


Figure 2.9: Schematic drawing of oxygen vacancy creation and hydride-ion incorporation in  $\text{BaTiO}_3$  *via* the topochemical synthesis route with a reducing agent ( $\text{CaH}_2$ ). Ti atoms are presented with green circles, O is represented with blue and the hydride ion with pink circles, respectively.

## 2.5.2 Hydride-ion dynamics

The mobility of hydride ions in  $\text{BaTiO}_{3-x}\text{H}_x$  oxyhydride with  $x$  ranging from 0.35 to 0.60, was observed recently, by replacing hydrogen with deuterium atoms above 400 °C [148–150]. This finding lead to further curiosity in uncovering the potential mechanism for hydride-ion diffusion. A computational study further proposed that the possible mechanisms of hydride-ion diffusion in these materials include jumps between nearest-neighbor (NN) and next-nearest-neighbor (2NN) sites (Figure 2.10) [78]. Building on this idea, a quasielastic scattering study on  $\text{BaTiO}_{3-x}\text{H}_y\text{O}_{x-y}$  with  $x$  between 0.18 and 0.7 and  $y$  between 0.04 and 0.1 [63, 80], showed that hydride ions are mobile already at room temperature. The diffusional mechanism of the hydride-ions was indeed confirmed to jumps between NN and 2NN sites, with jump distances between 2.7 and 5.2 Å increasing with temperature, respectively. It was also shown that these jumps are temperature-dependent, with predominant jumps between NN sites at temperatures below 250 K, and combination of jumps between NN and 2N sites at temperatures above 400 K [63, 80]. The difference in diffusion mechanism between  $\text{BaTiO}_3$  oxyhydride with and without oxygen vacancies is yet to be obtained. The local environment of the hydride-ions is significantly different than the one of protons in the perovskite oxides. The hydrogen atom in  $\text{BaTiO}_{3-x}\text{H}_x$  oxyhydride forms a Ti-H-Ti bonding, and participates in Ti-H related vibrations. These vibrations can be classified as vibrations along the Ti-H bond, here referred to as  $\omega_{\parallel}$ , and vibrations perpendicular to the Ti-H bond, here referred to as  $\omega_{\perp}$  [79, 80, 97]. Schematic drawing of these two types of vibrations is shown in Figure 2.10.

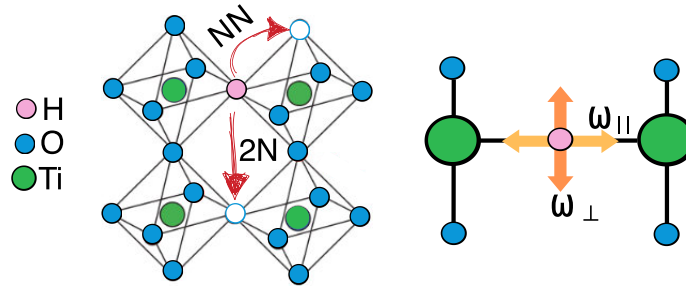


Figure 2.10: Schematic drawing of hydride-ion diffusion mechanisms in  $\text{BaTiO}_3$  oxyhydride along with vibrational modes of the hydride-ion, where the arrows indicate the direction of the motions.

## 2.6 Concluding remarks and scope of thesis

Although there has been significant effort to develop solid proton and hydride-ion conductors beyond perovskite-type materials, these materials still remain the most promising ones for application in fuel cells [2, 3, 33, 110]. However, developing a better understanding of the structure and dynamics of these materials is critical for future breakthroughs. For this purpose, this thesis aims to elucidate key questions related to local structure and dynamics. The studies have been focused on polycrystalline powder samples of  $\text{BaZr}_{1-x}\text{Sc}_x\text{O}_{3-x/2}$  ( $x = 0.10$  and  $0.50$ ) and  $\text{Ba}_2\text{In}_{1.85}\text{M}_{0.15}\text{O}_5$  ( $M = \text{In}, \text{Ga}, \text{Sc}$  and  $\text{Y}$ ), as well as of films of  $\text{BaZr}_{1-x}\text{Sc}_x\text{O}_{3-x/2}$  ( $x = 0.45, 0.54,$  and  $0.64$ ). Sc has been chosen as a dopant atom because its ionic radius is close to the one of Zr, which results in a cubic structure with high doping concentration and high proton conductivity (as opposed to e.g. Y which is much larger than Zr and does not remain cubic for large doping concentrations). This implies that it is possible to study the local structure and dynamics over a large range of dopant concentrations with the overall crystal structure essentially being (virtually) unaffected. Further, the studies have focused on  $\text{BaTiO}_3\text{H}_{0.12}$  with the aim to get a better understanding about the role of oxygen vacancies in the governing diffusional mechanisms for this material. The primary methods used for these investigations have been neutron scattering and infrared spectroscopy.

Additionally, the studies focused on optimization of the topochemical synthesis method for synthesis of  $\text{ATiO}_3$  oxyhydrides by utilizing different reducing agents for compositions with different amount of hydride-ions and oxygen vacancies. Likewise, the hydrogen gas reduction based synthesis method was applied for development of a series of  $\text{BaZr}_{1-x}\text{In}_x\text{O}_{3-x/2}$  ( $x = 0.1 - 1.0$ ). A concise description of the synthesis routes and the experimental methods used in this thesis is presented in the next chapter. A schematic summary of the studies is presented in Figure 2.11.

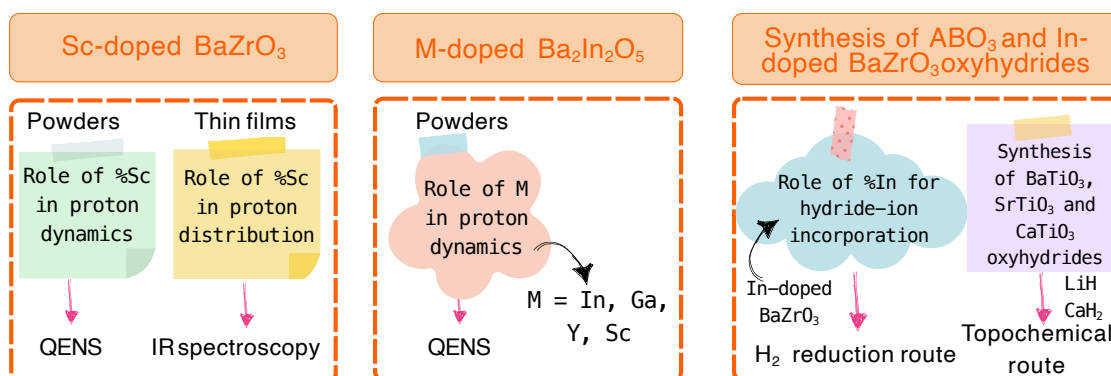


Figure 2.11: A schematic summary of the studies in this thesis. Please note that QENS refers to quasielastic neutron scattering, and IR spectroscopy refers to infrared spectroscopy. A detailed description of each method is presented in Chapter 3 and Chapter 4.



This chapter describes the synthesis protocol of the various powders and thin film samples of the proton- and hydride-ion conducting oxides as investigated in this thesis.

## 3.1 Proton-conducting oxides

### Polycrystalline powder samples

Perhaps the most commonly used synthesis route for obtaining polycrystalline powder samples of proton-conducting oxides is based on the solid-state route, which was also the technique used in this thesis. Essentially, the solid-state route is based on mixing precursors in agate mortar with pestle, followed up by formation of pellets and exposures to high temperatures above 1000 °C [30, 42, 50, 151–153]. The high temperature required for synthesis is an important issue that complicates further industrialization of these materials, as the high temperature is not suitable for industrial purposes, mostly from an economical point of view [33, 154, 155]. Furthermore, the high temperature synthesis may lead to other problems, such as Ba deficiency, which can result in the formation of grain boundaries with low proton conductivity [156]. Other synthesis methods such as sol-gel (obtaining solids from small molecules that undergo irreversible chemical reactions) or the wet chemical approach (obtaining solids from chemical reactions in solutions) have been designed to lower the synthesis temperature, sometimes below 100 °C, and/or to obtain a high amount of samples with less grain boundaries [1, 42, 48, 51, 157]. However, organic traces present in the proton conducting oxide materials as a result of these synthesis methods, can cause problems when using neutron scattering techniques, as this technique is highly sensitive to such species. Note, the solid-state route, described above, produce materials essentially free from protons. Introduction of protons in these materials can be achieved by a so called hydration procedure. Schematic drawing of the steps for the solid-state synthesis is presented in Figure 3.1.

In this thesis, the mixture of precursors was initially fired at 900 °C overnight to remove excess CO<sub>2</sub>. The powders were then mixed again in agate mortar with addition of 99% ethanol as a suppressing agent for about 1.5 hours. The finely ground mixture was then pressed into a pellet and put in a  $\alpha$ -Al<sub>2</sub>O<sub>3</sub> crucible and exposed to 1200 °C for 48 hours. After the first exposure, the pellet was crushed, and the powder was mixed again in a mortar with 99% ethanol for 1.5 hours, pressed into a pellet and put in  $\alpha$ -Al<sub>2</sub>O<sub>3</sub> crucible and exposed to 1325 °C for 72 hours. It is important to note that excess powder (from the powder mixture) was used as a "sacrificial" powder to cover the bottom of the crucible, and the top of the pellet; this is especially useful for eliminating any

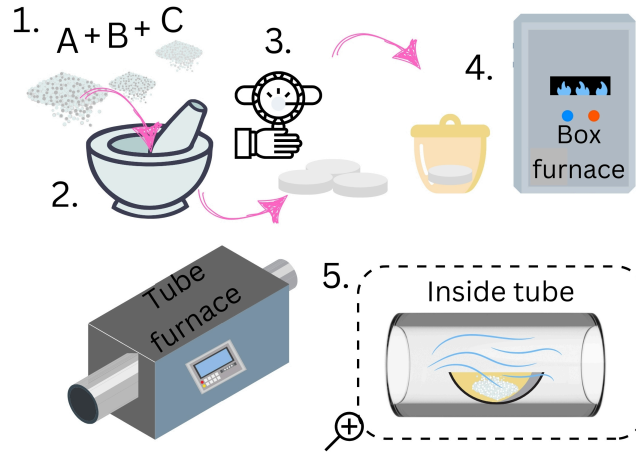


Figure 3.1: Schematic drawing of the solid-state route and proton incorporation in acceptor-doped perovskite-type oxides. The starting materials (precursors A, B and C) are combined (1) and mixed in a mortar with pestle (2), and compressed into pellets (3). The pellets are then placed in a  $\alpha$ - $\text{Al}_2\text{O}_3$  crucible and then fired at elevated temperature for a few days (4). Hydration (proton incorporation) of the sample is achieved in a tube furnace by exposing the material to a mixture of nitrogen gas and water vapor at elevated temperatures (5).

volatilization of  $\text{BaO}$ , or formation of impurities (especially  $\text{Sc}_2\text{O}_3$ ) due to contact with the crucible<sup>1</sup> [30, 151–153, 158–161]. The solid-state synthesis route was used for the synthesis of various doping concentrations of Sc- and In-doped  $\text{BaZrO}_3$  polycrystalline powder samples. Besides using this technique for synthesis of powder samples to be investigated by neutron scattering and infrared spectroscopy, it was also used for preparing the "targets" for the preparation of thin films (as described in the next section). Hydration of the samples was performed by heating the samples to 500–700 °C in a water vapour environment, followed by slow cooling to ambient temperatures [30, 152, 153].

## Nanocrystalline thin films

There are numerous fabrication techniques for film deposition, primarily classified as chemical vapor deposition and physical vapor deposition based techniques [162]. Techniques based on chemical vapor deposition are related to the undergoing chemical reaction between the substrate and gases in the chamber [162]. On the contrary, physical vapor deposition (PVD) is based on raw materials (targets) that are released and physically moved to the substrate surface by sputtering or thermal evaporation [162]. In this thesis two deposition methods based on PVD were used for fabrication of Sc-doped  $\text{BaZrO}_3$ , namely pulsed laser deposition (PLD) and magnetron co-sputtering.

Magnetron co-sputtering is based on ejection of sputtered atoms from targets, when exposed to a magnetic field, onto a substrate [163, 164]. In this thesis, ca. 2  $\mu\text{m}$  thick  $\text{BaZr}_{1-x}\text{Sc}_x\text{O}_{3-x/2}$  with  $x = 0.45, 0.54$  and  $0.64$  films, were deposited on 1 mm-thick double-side polished c-plane  $\text{Al}_2\text{O}_3$  substrates. The deposition process employed three different targets: with  $\text{BaZrO}_3$  as the primary source, Sc as the dopant, and Ba to maintain the metallic ratio. Detailed information on the film fabrication and structural characterization can be found in ref. [165]. The magnetron co-sputtering

<sup>1</sup>The principle of "sacrificial" powder is similar as coating the bottom of a pan with flour when baking cakes or bread.

deposition was performed by collaborators at Linköping University. A schematic drawing of the process is shown in Figure 3.2 (a). Followed by an investigation on the local proton environment of the  $\text{BaZr}_{1-x}\text{Sc}_x\text{O}_{3-x/2}$  with  $x = 0.45, 0.54$  and  $0.64$  films with infrared spectroscopy, additional films with similar composition were performed by PLD, with the aim to get more information on possible differences in these local proton environment when using another fabrication method.

PLD is based on an ablation of a target material using a high power pulsed laser beam onto a substrate [162, 166, 167]. In this thesis, approximately  $0.5 \mu\text{m}$  thick  $\text{BaZr}_{1-x}\text{Sc}_x\text{O}_{3-x/2}$  with  $x = 0.10, 0.20$  and  $0.30$  were deposited on on 1 mm-thick double-side polished  $c$ -plane  $\text{Al}_2\text{O}_3$  substrates. Ablation of the  $\text{BaZr}_{1-x}\text{Sc}_x\text{O}_{3-x/2}$  ( $x = 0.10-0.30$ ) powder targets was performed using a KrF excimer laser with an energy of 210 mJ, a fluence of  $2-3 \text{ J}\cdot\text{cm}^{-2}$ , and a working frequency of 4 Hz and under a  $\text{O}_2$  partial pressure of 0.3 mbar. The films were deposited at  $650 \text{ }^\circ\text{C}$  for 50 min. The samples were bonded to the holder with silver paste. The pulsed laser deposition was performed by collaborators at Rennes University. A schematic drawing of the process is shown in Figure 3.2 (b).

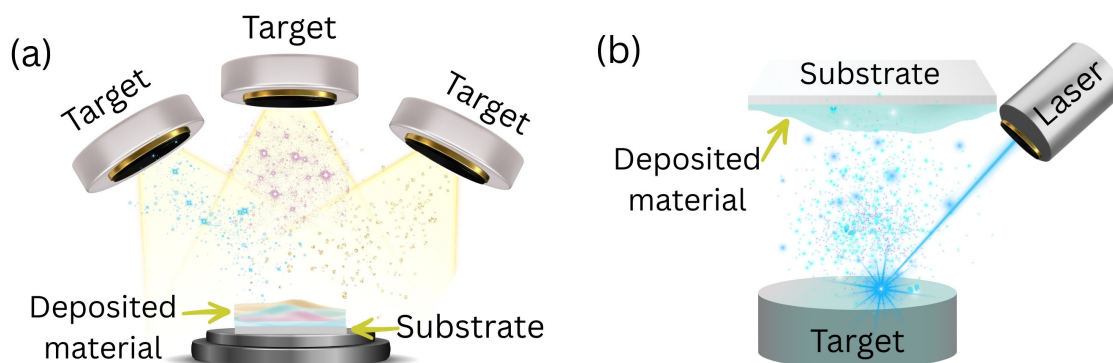


Figure 3.2: Schematic drawing of pulsed laser deposition (a) and magnetron co-sputtering (b) films fabrication technique.

## 3.2 Hydride-ion conducting oxides

### Topochemical route

The synthesis of polycrystalline powder samples of oxyhydrides can be quite challenging and typically requires a reducing or isolated environment. In a typical lab-scale synthesis, as schematically drawn in Figure 3.3, metal oxides are usually mixed with a reducing agent (metal hydride), in a mortar and then compressed into pellets. This entire process takes place inside a glove box filled with inert gas to prevent exposure to air, as the reducing agent is unstable in such conditions [64]. After mixing, the pellets are usually sealed in either silica or stainless steel tubes. In this thesis, we use stainless steel tubes sealed by welding within the glove box, primarily because they offer greater pressure resistance compared to silica tubes [64, 67, 69]. The final product (oxyhydride) is created by sintering the sealed sample in a furnace for several days at temperatures between a few hundred and several hundred  $^\circ\text{C}$ , depending on the type of reducing agent used [69]. Once the heating process is complete, the powders are washed with a weak acid and ethanol to remove any impurities.

The choice of a reducing agent, as previously mentioned, significantly influences both the sintering temperature and the concentration of hydride ions incorporated into the structure. Recent

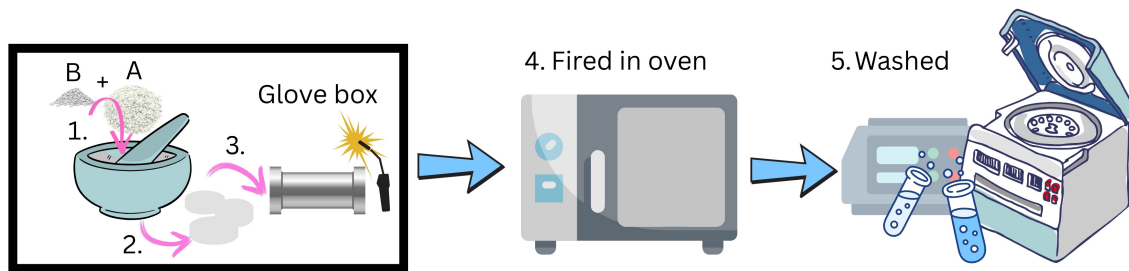


Figure 3.3: Schematic drawing of the topochemical route for synthesis of oxyhydrides. The starting materials (precursors A and B) are combined and mixed in a mortar (1), and compressed into pellets (2). The pellets are then sealed in a stainless steel tube by welding (3). The sealed tube is then fired at elevated temperature for few days (4), after which the powders are washed to remove impurities (5). Adapted and modified from [64].

studies showed that  $\text{BaTiO}_3$  can be successfully reduced using different metal hydrides [67, 145]. In these studies, different concentrations of  $\text{NaH}$ ,  $\text{NaBH}_4$ ,  $\text{CaH}_2$ ,  $\text{MgH}_2$ , and  $\text{LiH}$  were employed as reducing agents [67, 68]. It was found that  $\text{NaH}$  acts as a weak reducing agent for  $\text{BaTiO}_3$  mostly because of its low decomposition temperature, which likely produced hydrogen gas ( $\text{H}_2$ ) as the reducing agent [67, 68]. This reduction mainly changed only the surface layer of the  $\text{BaTiO}_3$  powder [67, 68]. When using  $\text{NaBH}_4$  for reduction, the resulting products remained a single phase even at the highest hydrogen concentrations, while other reducing agents created mixtures of two cubic phases as hydrogen concentration increased [67, 68]. Samples reduced with  $\text{MgH}_2$  showed the largest lattice parameters [67, 68]. Reducing  $\text{BaTiO}_3$  with  $\text{LiH}$  significantly lowered the sintering temperatures to as low as  $300\text{ }^\circ\text{C}$ , producing the oxyhydride  $\text{BaTiO}_{2.9}\text{H}_{0.1}$  [67]. At higher temperatures, oxygen vacancies were created, but the hydrogen concentration remained mostly the same. From an oxyhydride synthesis point of view, key questions that still need to be addressed are related to factors that influence the formation of oxyhydrides, instead of formation of solely vacancies amid the reduction of hydrides. Open questions are also related to the governing mechanism responsible for hydride incorporation and reduction in  $\text{BaTiO}_3$ . Addressing these questions would essentially contribute to the development of straightforward synthesis routes under mild conditions which could be applied to a wider class of oxyhydride systems. Such advancement would significantly benefit progress in the field.

In this thesis, polycrystalline powders of  $\text{BaTiO}_3\text{H}_x$ ,  $\text{SrTiO}_3\text{H}_x$  and  $\text{CaTiO}_3\text{H}_x$  oxyhydrides were prepared using different reducing agents. Specifically,  $\text{BaTiO}_3\text{H}_x$  was synthesized with  $\text{LiH}$  as the reducing agent, aiming to produce an oxygen-vacancy-free structure at a lower temperature of  $350\text{ }^\circ\text{C}$ . Meanwhile,  $\text{SrTiO}_3\text{H}_x$  and  $\text{CaTiO}_3\text{H}_x$  oxyhydrides were synthesized using  $\text{CaH}_2$  as the reducing agent at  $550\text{ }^\circ\text{C}$ . Due to the unchanged color (to blue),  $\text{BaTiO}_3$  oxyhydride was subject to an additional reduction with  $\text{LiH}$  followed by annealing for  $350\text{ }^\circ\text{C}$  for another 48 hours. After the heating steps, each of the powders was washed with acetic acid ( $\text{HAc}$ ) solution to remove residual  $\text{LiH}$  or  $\text{CaH}_2$ , respectively, as well as metal oxides or hydroxides formed during hydride reduction. The washing process for the  $\text{SrTiO}_3$  oxyhydride powder was repeated once more to remove remaining residuals. For the  $\text{CaTiO}_3$  oxyhydride, the overall washing process was repeated three times, with two of these processes involving  $0.5\text{ M HAc}$  solution to remove the excess of "stubborn" residuals.

## Gas reduction-based route

Some studies have suggested that hydride ions can be formed in acceptor doped perovskites, such as  $\text{SrTi}_{1-x}\text{Fe}_x\text{O}_{3-x/2}$ , when exposed to very low oxygen partial pressures [168, 169]. These findings introduced the concept that acceptor-doped perovskite systems, which have pre-existing oxygen vacancies, could be transformed into oxyhydrides and may serve as promising candidates for applications based on hydride-ion conduction. Crucially, a recent report on  $\text{BaZr}_{0.50}\text{In}_{0.50}\text{O}_{2.75}\text{H}_{0.5}$  oxyhydrides, created through a hydrogen gas reduction method [70] has opened up new possibilities for a class of oxyhydride materials with high hydride-ion conductivity.

The gas reduction route requires an atmosphere containing the specific anion of interest [64]. In this route, the metal oxides act as solid starting materials (precursors). Throughout the process, exchange reactions occur between the oxide ions and the anionic species present in the gas phase. This synthesis process typically uses a tube furnace, as illustrated in Figure 3.4. The precursor is placed in a boat-shaped crucible, which is then inserted into the furnace tube and heated in a hydrogen gas environment. The reduction reaction begins with hydrogen molecules adsorbing onto the surface of the powder, as well as a reaction forming oxygen vacancies at that surface. It is important to note that the surface of the powder interacts with gas molecules more frequently, potentially resulting in uneven reactions between the surface and the bulk of the powder [64, 145]. Crucially, the synthesis conditions, such as hydrogen gas flow and temperature, must be carefully controlled to manage the oxidation state of the cations and prevent their reduction to pure metals [64]. However, it is challenging to control all parameters at once, as they can change depending on the nature of precursor used. This is why synthesis conditions are often determined through empirical methods. Significant effort is required to tackle these challenges and create a more straightforward synthesis approach based on the gas reduction synthesis.

In this thesis, powders of  $\text{BaZr}_{1-x}\text{In}_x\text{O}_{3-x/2}$  with  $x = 0.10, 0.20, 0.56$  and  $0.59$ , were loaded in alumina crucibles, which were put in a quartz tube and heated in a tube furnace. Before exposure to  $\text{H}_2$  gas (99.999%), the samples were annealed in an argon (99.999%) flow for several hours to remove moisture. Then, the samples were heated under flowing hydrogen gas at  $800\text{ }^\circ\text{C}$ . Exposure times varied between 24-48 hours. Afterwards, the samples were cooled down up to  $150\text{ }^\circ\text{C}$  while still being exposed to hydrogen gas. Cooling down from  $150\text{ }^\circ\text{C}$  to room temperature was performed in argon atmosphere. Lowering of the exposure temperature, as well as changes in hydrogen gas flow and reduction time was likewise performed in order to modify the synthesis method.

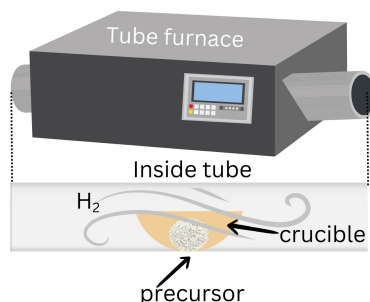


Figure 3.4: Schematic drawing of the gas reduction route for synthesis of oxyhydrides. The starting materials are placed in a boat crucible and exposed to a hydrogen gas environment at elevated temperatures for several hours. The reduction and hydride ion incorporation start at the surface of the material and penetrate to the bulk. Adapted and modified from [64].



---

# 4 Experimental techniques

## 4.1 Neutron scattering

Millions saw the apple fall, but Newton asked why.

---

*Bernard Baruch*

### 4.1.1 Foundation and mathematical background

<sup>1</sup>Neutron scattering is a highly powerful experimental technique used across various fields, including physics, chemistry, biology, and materials engineering [79, 131, 170–172]. Neutrons are particularly advantageous for probing the structure and dynamics of materials due to several benefits connected to their fundamental properties [173]. As uncharged particles, neutrons interact directly with atomic nuclei through nuclear interactions, allowing the neutrons to penetrate into the bulk of materials. The relatively weak interaction also makes neutron scattering a non-destructive method. Additionally, the random variability of the nuclear interactions across the periodic table is noteworthy; specifically, hydrogen possesses a large cross-section, making it detectable by neutrons, in contrast to its invisibility to X-rays, schematically illustrated in Figure 4.1 [173]. However, this weak interaction also makes neutron scattering a relatively "slow" and costly technique. As a result, neutrons are typically employed only when other methods are insufficient.

Furthermore, the neutron has a wave-like behavior characterized with sinusoidal oscillations in both space and time; the square of its amplitude would indicate the probability of finding the neutron at a specific location [131, 173]. When neutrons scatter, the strength of the interaction between the neutron and the nucleus is related to the amplitude of the neutron, while the scattered neutron wave is isotropic,<sup>2</sup> and can be written as  $(-b/\vec{r})e^{i\vec{k}\vec{r}}$ , considering the nucleus is at the center of the coordination system [131, 173]. In this context,  $\vec{k}$  is the wave vector of magnitude  $\vec{k} = 2\pi/\lambda$ ,  $\vec{r}$  is the position vector,  $b$  is the scattering length of the nucleus which reflects the strength of the neutron-nucleus interaction,  $(1/\vec{r})$  is the factor used for the inverse square law which points out that the intensity of the neutron beam, defined by the square of the amplitude, is decreasing as the

---

<sup>1</sup>This chapter is partially based on my Licentiate thesis [1].

<sup>2</sup>The scattering event of the neutron can be described by the cross section  $\sigma$  quod est the effective area of the nucleus to the passing neutron. When the neutron hits this area, it scatters isotropically (it has an equal probability to scatter in any direction) because the nuclear potential range is much smaller than the neutron's wavelength.

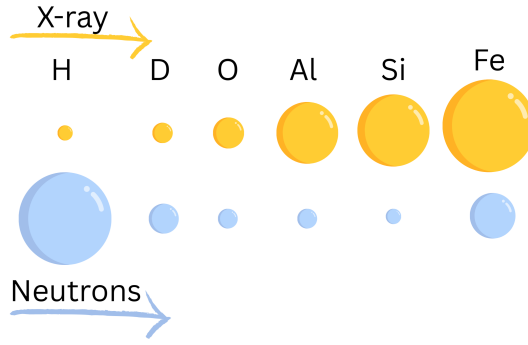


Figure 4.1: Schematic drawing of the X-ray and total neutron cross-sections of some elements. Figure adapted from [173].

inverse square of the distance from the source. In this type of collision, the neutron's energy does not change and is referred to as elastic. Yet, when a neutron interacts with matter, it may change its momentum and energy, as scattering occurs with atoms that are in motion to some extent; this type of scattering, which leads to a gain or loss of energy, is referred to as inelastic scattering. The amount of momentum transferred by the neutron during this type of collision is called momentum transfer and is described as  $\hbar\vec{Q} = \hbar(\vec{k}_i - \vec{k}_f)$ , where  $\vec{k}_i$  is the incident wave vector of the neutron, and  $\vec{k}_f$  is the scattered wave vector. Accordingly,  $\vec{Q} = \vec{k} - \vec{k}'$  is the scattering vector and can be geometrically represented by the scattering triangle shown in Figure 4.2 a). As can be seen, the direction and magnitude of  $Q$  is dependent on the incident and scattered neutrons (in terms of vector addition), as well as the  $2\theta$  angle named the scattering angle [131, 173, 174]. The scattering length  $b$ , which varies among different atoms and their isotopes, is related to the cross section  $\sigma$  by  $\sigma = 4\pi b^2$  [131, 173]. Experimentally, the quantity that is measured in a neutron scattering experiment is given by the double differential cross-section according to:

$$\frac{d^2\sigma}{d\Omega dE_f} = \frac{k'}{k} \frac{1}{4\pi} \left\{ \sigma_{coh} S_{coh}(Q, E) + \sigma_{inc} S_{inc}(Q, E) \right\} \quad (4.1)$$

where

$$\sigma_{coh} = 4\pi \langle b \rangle^2 = 4\pi b^2 \quad (4.2)$$

$$\sigma_{inc} = 4\pi (\langle b \rangle^2 - \langle b^2 \rangle) \quad (4.3)$$

Here,  $S_{coh}(Q, E)$  and  $S_{inc}(Q, E)$  are the coherent and incoherent dynamic structure factors, respectively, which contain information about correlations in both space and time, and  $\sigma_{coh}$  and  $\sigma_{inc}$  are the coherent and incoherent cross sections, respectively. Incoherent scattering arises due to random variations in the scattering lengths of atoms within a sample, which can result from different isotopes of the same element or isotopes with non-zero nuclear spin (like hydrogen). This type of scattering provides insights into the behavior of individual particles, in contrast to coherent scattering, which reveals information about spatial correlations or collective motion, thereby addressing questions related to the positions of atoms [131, 173]. For hydrogen, the incoherent cross section  $\sigma_{inc} = 80.26$  barn is extraordinary large, whereas the coherent cross section  $\sigma_{coh} = 1.76$  barn is rather small [131].<sup>3</sup> As mentioned above, neutron scattering can also be classified as elastic or inelastic. Elastic scattering reveals information regarding the positions of atoms and their rearrangements. Conversely, inelastic scattering occurs when the neutrons experience a change in energy during the

<sup>3</sup>Metric unit of area equal to  $10^{-28} \text{ m}^2 = 1$  barn.

scattering event, offering insights into both diffusional and vibrational dynamics (periodic motions) within a material. A subcategory of inelastic scattering is quasielastic neutron scattering (QENS), which occurs due to random (non-periodic) motions of atoms, such as diffusion or molecular orientational motions in a material. Such motions lead to small energy transfers of the neutrons resulting in a continuous broadening of the elastic peak of the overall spectrum [131, 173]. A schematic drawing of the three scattering components, i.e., elastic, inelastic and quasielastic scattering, which may be measured in a neutron scattering experiment are presented in Figure 4.2 b).

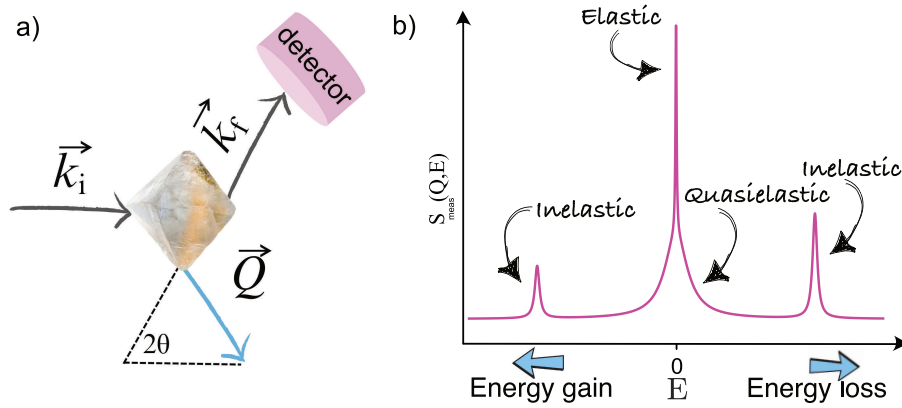


Figure 4.2: A Schematic drawing of a scattering experiment along with the relations of incident and scattered wave vectors a). A schematic drawing of the elastic, inelastic and quasielastic scattering, which are measured in a neutron scattering experiment b).

## 4.1.2 Quasielastic neutron scattering

The measured scattering intensity,  $S(Q, E)$ , in a QENS experiment, can be expressed as

$$S(Q, E)_{\text{meas}} \propto S(Q, E) \otimes R(Q, E), \quad (4.4)$$

where  $S(Q, E)$  is the dynamic structure factor that contains information about the dynamical properties of the investigated material, and  $R(Q, E)$  is the instrumental resolution function. Typically,  $S(Q, E)$  consists of both a coherent and an incoherent component. However, earlier QENS investigations on proton-conducting oxides have demonstrated that almost only the incoherent scattering from protons contributes to the quasielastic signal [175]. This has the important indication that the quasielastic signal can be ascribed to self-dynamics rather than collective dynamics, of the protons.

For the QENS experiments in this thesis,  $S(Q, E)$  was fitted with a function composed of one elastic component, described as the intensity  $I_D(Q)$  multiplied with a Dirac delta function, a quasielastic component which represents the broadening of the elastic peak, as the intensity  $I_L(Q)$  multiplied with a Lorentzian function  $L(Q, E)$ , and a background,  $bkq(Q, E)$ , see Eq. (3.5).

$$S(Q, E) = I_D(Q)\delta(E) + I_L(Q)L(Q, E) + bkq(Q, E). \quad (4.5)$$

The background originates from scattering of species that are featured by a dynamics too fast to be resolved by the instrument and thus cause broadening of the QENS signal to the baseline, or inelastic scattering that forms peaks in the QENS signal. From the full width at half maximum (FWHM) of the Lorentzian function one can obtain information about the timescale ( $\tau$ ) of these processes as  $\tau = 2\hbar/\text{FWHM}$ , which is important for accessing more information about the nature of the localized motion and rate-limiting steps for long range diffusion, in our case. The activation energy can be obtained from the temperature dependence of FWHM under the assumption that the dynamics follow an Arrhenius temperature dependence. Figure 4.3 shows, as an example, the  $S(Q, E)$  at  $T = 510$  K and  $Q = 1.325 \text{ \AA}^{-1}$  for hydrated  $\text{BaZr}_{0.50}\text{Sc}_{0.50}\text{O}_{2.75}$  together with fits featuring one Lorentzian function, as measured in this thesis.

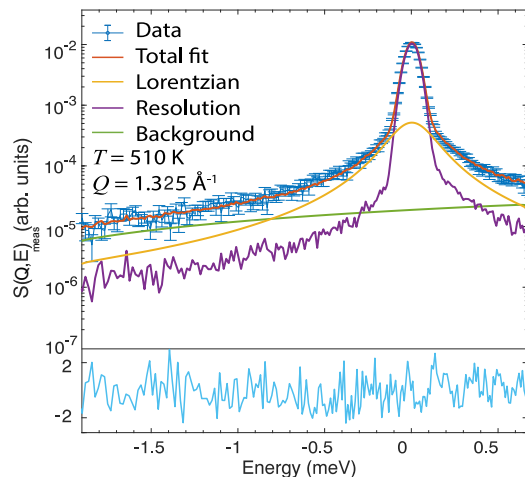


Figure 4.3:  $S(Q, E)$  at  $T = 510$  K and  $Q = 1.325 \text{ \AA}^{-1}$  for hydrated  $\text{BaZr}_{0.50}\text{Sc}_{0.50}\text{O}_{2.75}$  together with fits, as measured on the IN6 instrument at Institut Laue-Langevin (Paper I).

## Analysis of the spatial geometry of the localized dynamics

Information regarding the spatial geometry of localized dynamics observed as quasielastic scattering can be obtained from analysis of the elastic incoherent structure factor (EISF), defined as the ratio of the elastic intensity over the sum of the elastic and quasielastic intensity (see Eq. 3.5), i.e.  $EISF = I_D/(I_D+I_L)$ . Figure 4.4 shows, as an example, the EISF for  $BaZr_{0.50}Sc_{0.50}O_{2.75}$  together with fits to theoretical jump-diffusion models over two and four sites, respectively, which here represent proton transfers (jump from one to another neighboring oxygen atom) or rotational diffusion of the proton around one oxygen atom, accordingly [115, 116, 176, 177]. In this thesis, the jump diffusion models regarding jumps between two sites (2N) and jumps between four sites (4N) were fitted as per the following equations:

$$EISF_{2N} = c + (1 - c) \frac{1}{2} \left( 1 + \frac{\sin(Q2r_{2N})}{Q2r_{2N}} \right) \quad (4.6)$$

$$EISF_{4N} = c + (1 - c) \frac{1}{4} \left( 1 + \frac{2 \sin(\sqrt{2}Qr_{4N})}{\sqrt{2}Qr_{4N}} + \frac{\sin(2Qr_{4N})}{2Qr_{4N}} \right) \quad (4.7)$$

The constant  $c$  may be interpreted here as extra elastic scattering due to "immobile" protons, i.e., protons that give rise to scattering, but move too slowly to give rise to quasielastic scattering in the probed "time window";  $r_{2N}$  is half of the jump distance between neighboring oxygen atoms, and  $r_{4N}$  is the length corresponding to the O-H bond.

## Analysis of the spatial geometry of the long-range dynamics

Information regarding the spatial geometry of long-range dynamics observed as quasielastic scattering can be obtained from analysis of the  $Q$ -dependent FWHM. The long-range diffusion in proton-conducting oxides is characterized by a sequence of successive jumps, defined by a characteristic jump length and the time between each jump (the residence or relaxation time). Specifically to this thesis, the model that was used to address long-range diffusion was the one proposed by Chudley and Elliott (C-E) [178], which assumes a constant jump length,  $d_{C-E}$ , a fixed residence time,  $\tau$ , and a negligible jump time, as per the relationship:

$$FWHM = \frac{2\hbar}{\tau} \left( 1 - \frac{\sin(Qd_{C-E})}{Qd_{C-E}} \right) \quad (4.8)$$

Other commonly used models for describing long-range diffusion in proton-conducting oxides, although not applied to in this thesis, are the Hall-Ross model [179], which assumes a Gaussian distribution of jump lengths, and the Singwi and Sjölander model [180], which assumes an exponential distribution of jump lengths.

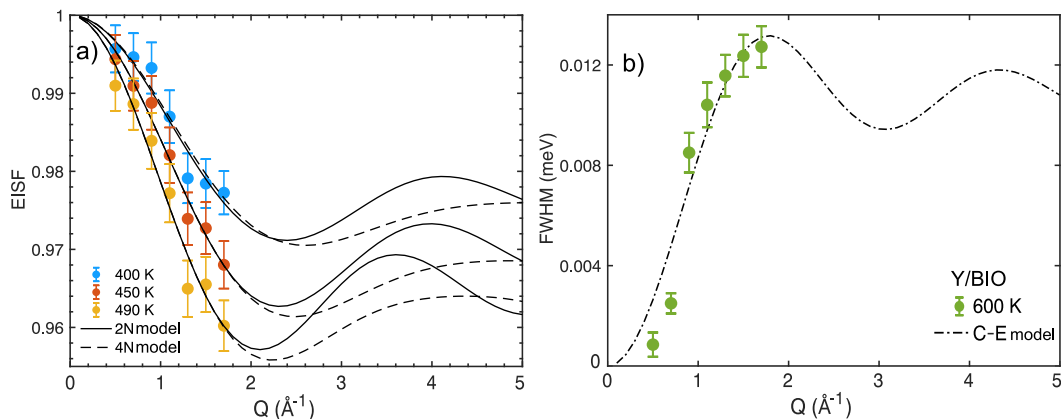


Figure 4.4: Fits for geometrical representation of localized dynamics a) and long-range dynamics b) for different temperatures of hydrated  $\text{Ba}_2\text{In}_{0.85}\text{Y}_{0.15}\text{O}_5$  as measured on the BASIS instrument at Oak Ridge National Laboratory. The data are compared to jump diffusion models over two (2N) and four (4N) sites a), and the jump diffusion over a lattice as per C-E model b) (Paper II).

### 4.1.3 Inelastic Neutron Scattering

INS refers to inelastic neutron scattering and can be used to obtain the vibrational spectra of a material. Unlike the commonly used Raman and infrared spectroscopy which are limited by certain selection rules, INS is based on the interaction of the neutron with the material's different cross sections, therefore allowing for measurements of all the vibrations present [79, 80, 172, 173, 181]. Nevertheless, the combination of INS with Raman and/or infrared spectroscopy is often necessary to give the complete picture of the vibration fingerprint in a material; as an example, some vibrations may be absent in the infrared spectrum, but intense in the Raman spectrum and quite weak in the INS spectrum [172].

In more detail, INS reveals information of the interactions between neutrons and a sample that involve energy transfers. When a neutron gains energy ( $E < 0$ ), it causes the sample to lose energy. Conversely, when a neutron loses energy ( $E > 0$ ), the sample gains energy [79, 80, 173]. Explained in simple words, INS allows us to see how atoms and molecules move by observing the inelastic interaction between neutrons which bounce off a non-rigid framework and exchange energy with it [173]. This process allows for investigations of the vibrational excitation states within the sample.

The measured intensity of a vibrational band  $S_i$  is dependent on both its energy  $E_i$  and the momentum transfer  $Q$  and is, accordingly, proportional to:

$$S_i(Q, E_i) \propto \sigma e^{-Q^2 U_{total}^2} \frac{(QU_i)^{2n}}{n!}, \quad (4.9)$$

where  $n = 1$  for fundamental mode,  $n = 2$  and  $n = 3$  are the first and second overtone, respectively; the average neutron scattering cross section of all atoms involved in the mode is denoted as  $\sigma$ , whereas the vibrational amplitude of the normal mode  $i$  is represented by  $U_i$ , and the total displacement of all atoms summed over all modes is  $U_{total}$ .

Typically, INS probes vibrational motions in condensed matter within the energy range up to 500 meV [80]. These vibrations are small oscillations of atoms around their equilibrium. In materials such as proton- and hydride-ion conducting oxides, INS can detect collective vibrational modes (phonons), as well as individual vibrations of the hydrogen ions [80, 172, 181].

In perovskite-type ion conducting oxides, the low energy vibrational modes up to 75 meV are interpreted as various vibrations of the perovskite host lattice, including A-site ion vibrations, octahedral and oxygen vibrations [97, 181]. The first-order (fundamental) vibrations involving hydrogen, such as wag O–H vibrations in proton-conducting perovskites, or hydride-ion vibrations involving the B-site cation are peaking around 80–150 meV [97, 182]. Example of such modes in  $\text{BaTiO}_{3-x}\text{H}_x$ , parallel and perpendicular to the Ti-H bond, here denoted with their frequencies  $\omega_{\parallel}$  and  $\omega_{\perp}$  is shown in Figure 4.5.

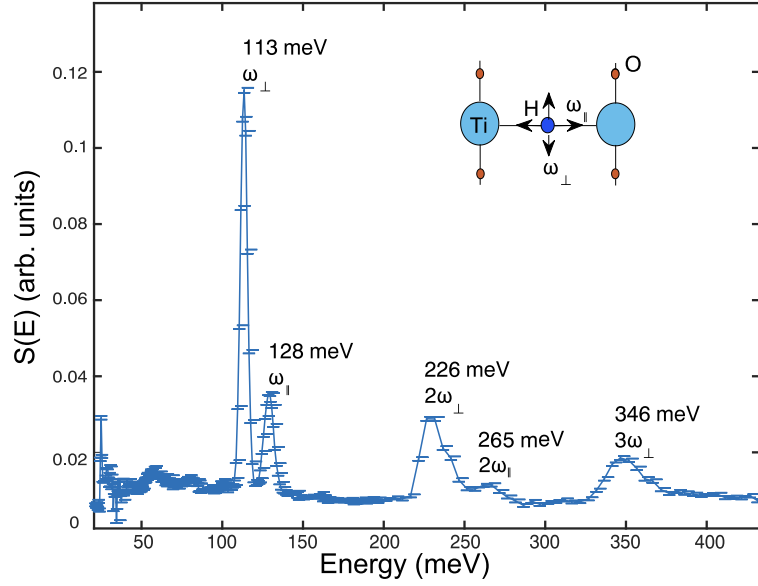


Figure 4.5: Peak assignments of vibrational motions involving the hydride-ion along with schematic representations of those motions. INS measurement performed at 10 K on the LAGRANGE spectrometer at Institut Laue-Langevinu, France (Paper IV).

## 4.2 Infrared spectroscopy

Infrared (IR) spectroscopy is based on excitation of vibrational motions of atoms by electromagnetic radiation in the IR range. It provides information about the specific vibrational frequencies and bond strengths in a material. To put simply, let us assume that atoms are balls connected by springs (bonds). The way the balls vibrate depends on their mass and how strong the springs are. In essence, IR spectroscopy detects these vibrations at particular frequencies which are related to different modes associated with a certain bond type [183]. For a certain material to have an IR spectral fingerprint, it must, however, fulfill a selection rule which states that the dipole moment of the atoms consisting it, must change during vibration. Hence not all vibrations are IR active. For instance, for homonuclear diatomic molecules like O<sub>2</sub> or N<sub>2</sub> stretch modes are not IR active, whereas stretch modes of heteroatomic diatomic molecules such as CO, HF, and OH are IR active [183].

As the primary concern of this study is the O–H stretch mode, further in this section we will discuss the O–H stretch mode characteristics in hydrated BaZr<sub>1-x</sub>Sc<sub>x</sub>O<sub>3-x/2</sub> ( $x = 0.10$ – $0.65$ ) powders and films, as well as hydrated Ba<sub>2</sub>In<sub>1.85</sub>M<sub>0.15</sub>O<sub>5</sub> powders with M = In, Ga, Sc and Y. When analysing IR spectroscopic data, vibrational modes are often assigned based on the presence of specific bonds which have a specific IR fingerprint. Some of the strongest (and shortest) bonds are formed with hydrogen and elements from the second row of the periodic table, such as oxygen. Hydrogen bonding is crucial in identification of structures of inorganic materials [183]. The O–H stretch modes are wildly affected by hydrogen bonds. For instance, sharp intense bands for free or isolated O–H groups are observed in the range of 3590–3690 cm<sup>-1</sup>, however, in presence of hydrogen bonding, the O–H stretch band typically shifts to lower frequency, where proton sites with different hydrogen bonds are present, such as for example the presence of different proton sites identified for hydrated Ba<sub>2</sub>In<sub>0.85</sub>M<sub>0.15</sub>O<sub>5</sub>, M= In, Ga, Y and Sc materials as shown in Figure 4.6.

In more detail, understanding the proton environment is especially useful when studying proton-conducting oxides. In this work, the proton sites were classified as two main types, namely sites in the low frequency region (below 375 meV) and in the high frequency region (above 375 meV) of the O–H stretch band in the spectrum. Bonds in the low frequency region correspond to protons with strong hydrogen bonding, indicating that a predominant motion would be the proton transfer (jump); whilst, protons in the high frequency region correspond to protons with weaker hydrogen bonding, indicating that the predominant motion would be the rotational motion of the –OH group (Paper II). The shape of the O–H stretch band, corresponding to O–H stretching modes in different local coordination environments can also give information of the availability of proton sites. Broader O–H stretch band would indicate more diverse distribution of protons in different sites, whereas more narrow O–H stretch band, on the contrary, would indicate preferred sites of the protons (Paper III). In combination with other techniques, such and neutron scattering techniques, IR spectroscopy can give powerful insights into the local proton environment and preferred localized diffusion mechanism present in materials.

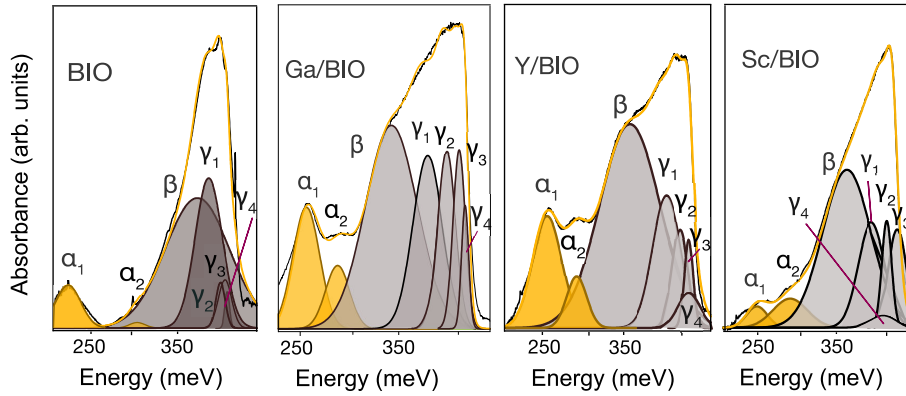


Figure 4.6: Fits of different proton sites in the O–H stretch region of the IR spectra for hydrated  $\text{Ba}_2\text{In}_{0.85}\text{M}_{0.15}\text{O}_5$ ,  $\text{M} = \text{In}, \text{Ga}, \text{Y}$  and  $\text{Sc}$  (BIO, Ga/BIO, Y/BIO and Sc/BIO, respectively). The  $\alpha$  peaks correspond to protons with relatively strong hydrogen bonding, whereas the  $\beta$  and  $\gamma$  peaks correspond to protons with relatively weaker hydrogen bonding (Paper II).

### 4.3 Other techniques used in this thesis

In addition to the primary techniques as described in sections 4.1 and 4.2, additional analytical techniques have been routinely utilized in this thesis in order to verify the chemical composition, incorporation of hydrogen, and purity of the powder and film samples investigated in this thesis.

#### 4.3.1 Thermogravimetric analysis

Thermogravimetric analysis (TGA) is a method that monitors mass changes as a function of temperature. TGA is, therefore, especially convenient for observing various chemical phenomena including, but not limited to, oxidation, vaporization, dehydration, and solid-state reactions, which is why it is applicative as a characterization tool in very diverse fields within material science [184]. In this work, TGA has been used for determining the degree of hydrogen concentration in hydrated powder samples of  $\text{BaZr}_{1-x}\text{Sc}_x\text{O}_{3-x/2}$  ( $x = 0.10$  and  $0.50$ ) and  $\text{Ba}_2\text{In}_{1.85}\text{M}_{0.15}\text{O}_5$  ( $\text{M} = \text{In}, \text{Ga}, \text{Sc}$  and  $\text{Y}$ ). These materials have distinctive thermograms, characterized with a broad slope in the interval between  $300\text{ }^\circ\text{C}$  and  $500\text{ }^\circ\text{C}$  upon increasing temperature, manifested by a gradual dehydration of the materials, followed by a final plateau, as shown in Figure 4.7 for  $\text{Ba}_2\text{In}_{1.85}\text{Ga}_{0.15}\text{O}_6\text{H}_2$  (Ga/BIO). However, for some proton conducting oxides the curves do not reach such a plateau even at temperatures beyond  $900\text{ }^\circ\text{C}$ . The reason for this behavior is, at present, not fully understood, but may be linked with a release of strongly physisorbed water molecules and/or bulk protons, as seen in other studies on similar materials [185–187].

Beyond proton-conducting oxides, TGA measurements were likewise performed on the synthesized oxyhydrides in order to verify that they are reduced and get a rough estimate of the content of hydride-ions (if any) present in the structure. The oxyhydride thermograms are characterized by a rise in mass for the temperature range between  $550$  and  $650\text{ }^\circ\text{C}$ , manifesting gradual oxidation, followed by a final plateau at temperatures above, as shown for  $\text{BaTiO}_3$  oxyhydride (BTO) in Figure 4.7.

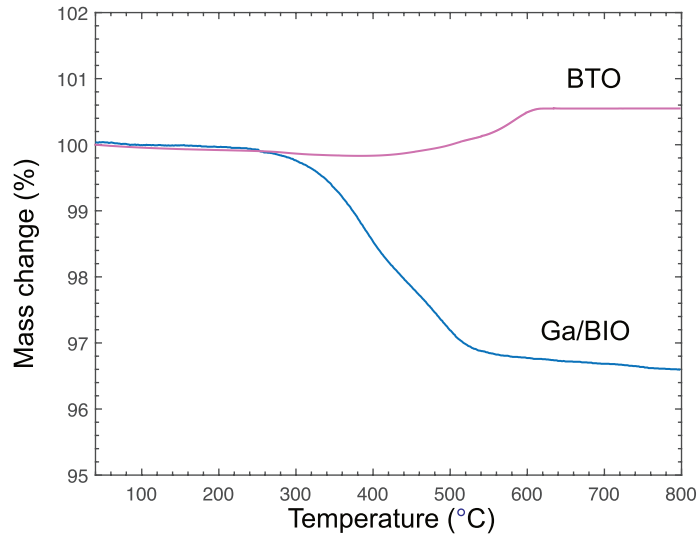
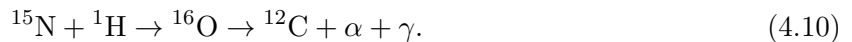


Figure 4.7: TG curve for a hydrated powder sample of  $\text{Ba}_2\text{In}_{1.85}\text{Ga}_{0.15}\text{O}_6\text{H}_2$  (Ga/BIO), presented as a blue line, and  $\text{BaTiO}_{3-x}\text{H}_x$  oxyhydride (BTO), presented with a pink line.

### 4.3.2 Nuclear Reaction Analysis

Nuclear reaction analysis (NRA) was used to verify the degree of hydrogen in films of  $\text{BaZr}_{1-x}\text{Sc}_x\text{O}_{3-x/2}$  ( $x = 0.45, 0.54, \text{ and } 0.64$ ). The basic principle of NRA is that the film of interest is exposed to accelerated and energy-monochromatized  $^{15}\text{N}$  ions, which upon contact with hydrogen in the film, these ions undergo the following reaction:



At resonance energy  $E_R = 6.385$  MeV, excited  $^{16}\text{O}$  nucleus is formed as an intermediate compound, which then undergoes  $\alpha$ -decay into the first nuclear excited state of  $^{12}\text{C}$ , followed by release of  $\gamma$ -radiation with energy equal to 4.4389 MeV. The intensity of the  $\gamma$ -radiation signal is measured by a  $\gamma$ -detector and it is related to the hydrogen concentration at a specific depth. The  $^{15}\text{N}$  ions with  $E_N = E_R$  can only induce a reaction with the hydrogen atoms near the surface of the film [188]. For  $E_N > E_R$ , the  $^{15}\text{N}$  ions penetrate further into the film, and lose energy due to electronic stopping amid traveling through the film,  $\Delta E = E_N - E_R$ . Crucially, the energy loss  $\Delta E$  is proportional to the certain depth, or, to the trajectory length of the penetrated ions,  $z$ , which is equal to zero at the surface [188], and can be calculated as  $z = \Delta E/S$ , where  $S$  is the stopping power which, in our experiments, is related to the total film thickness. A schematic drawing of the NRA measurements on film samples is shown in Figure 4.8.

In our experiments, the energy resolution of the  $^{15}\text{N}$  beam was set to be around 13 keV, which corresponds to a depth resolution of a film of 50 Å, as previously determined by NRA measurements on a  $\text{BaZr}_{0.53}\text{In}_{0.47}\text{O}_{2.765}$  500 nm thick film [189]. The obtained results from the NRA measurements give information about the total hydrogen concentration and hydration degree of the film samples.

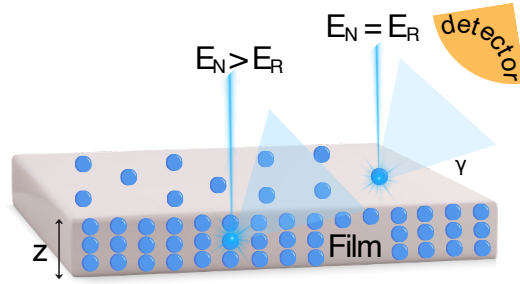


Figure 4.8: Schematic drawing of the basic principle of NRA for detection of hydrogen. Here,  $E_N$  represents the energy of the  $^{15}\text{N}$  ions, and  $E_R$  the resonance energy equal to 6.385 MeV.

### 4.3.3 Powder X-ray diffraction

Powder X-ray diffraction (XRD) is a commonly employed technique in materials science for analyzing the crystal structure of materials [190, 191]. This process involves exposing a material of interest to X-rays, which upon interaction with the material, produce constructive interference (and also diffracted rays) when conditions satisfy Bragg's law:  $n\lambda = 2d\sin(\theta)$ . Essentially, Bragg's law relates the wavelength of the X-ray to the diffraction angle and the lattice spacing in a material. The intensities of the diffracted X-rays are detected and counted. By scanning the sample to a  $2\theta$  range, all possible diffraction directions of the lattice should be achieved. The intensities of the scattered X-rays are then plotted against the scattering angle, resulting in a diffraction pattern  $I(2\theta)$  [190, 191].

This diffraction pattern  $I(2\theta)$  provides insights into the material's crystal structure, as each material exhibits a unique diffraction pattern, akin to a fingerprint (Figure 4.9). Further analysis of this pattern can reveal information such as the presence of different phases and the sizes of grains in polycrystalline materials [190, 191]. In this thesis, XRD was used to perform phase analysis and in particular determination of (phase) purity of the analyzed material.

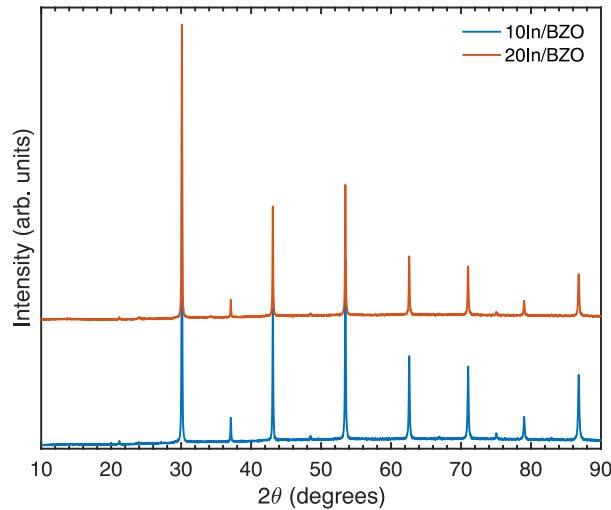


Figure 4.9: Examples of diffraction pattern of  $\text{BaZr}_{1-x}\text{In}_x\text{O}_{3-x/2}$ ,  $x = 0.10$  and  $0.20$  powder samples used as precursors for synthesis of oxyhydrides.

### 4.3.4 Energy dispersive spectroscopy

The analysis of X-rays produced when a high-energy electron beam interacts with a sample in an electron microscope is called energy dispersive spectroscopy (EDS) [190]. These X-rays are generated when the high-energy electron strikes a specific area of the sample, ejecting a core electron [190]. As a result, outer shell electrons transition to fill the vacant lower energy levels, emitting X-rays in the process. A detector is used to analyze these X-rays [190].

The EDS spectrum is composed of different peaks, where each peak corresponds to the characteristic radiation of a specific element in the sample. The intensity of each peak is proportional to the amount of that element present, allowing for the determination of the sample's composition. By measuring the intensities of these peaks, a quantitative assessment of the elemental composition is obtained, providing accurate information about the atomic composition of the sample [190]. In this thesis, EDS was used as a complementary technique for verification of elemental compositions of various proton- and hydride-ion conducting materials.

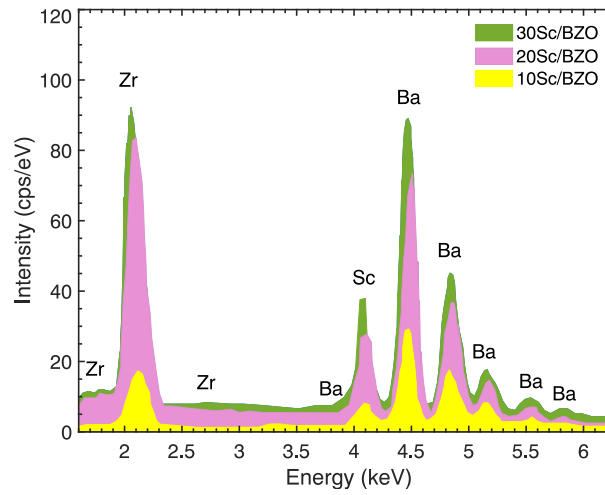


Figure 4.10: Examples of EDS spectra of BaZr<sub>1-x</sub>Sc<sub>x</sub>O<sub>3-x/2</sub>,  $x = 0.10, 0.20$  and  $0.30$  powder samples used as targets for fabrication of films.

---

The true method of knowledge is  
experiment.

---

*William Blake*

## 5.1 Quasielastic neutron scattering

<sup>1</sup>There are different types of instruments for performing QENS measurements. In this thesis, neutron time-of-flight (TOF) and backscattering instruments were used. The primary difference between the two types of instruments is in the determination of the neutron energy transfer  $\Delta E = E_i - E_f$ , where  $E_i$  is the incident neutron energy and  $E_f$  is the final neutron energy. The TOF instruments have a, so called, direct geometry, which means that neutrons with fixed  $E_i$  hit the sample;  $E_f$  is then determined by measuring the time the neutron needs to reach the well-defined distance between the sample and the detector, as shown in Figure 5.1 a). Backscattering scattering instruments, have an indirect geometry, which means that  $E_f$  is selected by Bragg reflection from an analyzer crystal (in our case a Si crystal), and  $E_i$  varies, as shown in Figure 5.1 b).

Traditionally, a Doppler-moving monochromator that selects the  $E_i$  wavelength is part of backscattering instruments. However, for spallation source-based instruments, like the one used in this thesis, the  $E_i$  wavelength is a result of a built-in neutron pulsed structure.

The difference when using these two techniques is within the energy resolution, which due to the Bragg angle close to  $90^\circ$ , is much higher ( $\mu\text{eV}$  range) for the backscattering technique. Accordingly, this corresponds to measurements of different timescales; due to the higher energy resolution, backscattering instruments can probe longer time-range than TOF instruments, which gives the possibility of observing long-range diffusional processes in addition to localized diffusion.

As part of this thesis, three TOF instruments were used for studies on the localized proton motion in Sc-doped  $\text{BaZrO}_3$  and  $\text{Ba}_2\text{In}_2\text{O}_5$  powders, i.e., IN6, TOFTOF, and FOCUS.

IN6 is a TOF instrument at Institut Laue–Langevin (ILL), in Grenoble, France. The polychromatic neutron beam is monochromized by graphite monochromator which is then chopped by a Fermi chopper. The scattered neutrons are then detected by 337 He detectors covering scattering angles between  $10^\circ$  and  $115^\circ$  [79, 192]. For our experiments, the spectrometer operated with  $5.1 \text{ \AA}$  incident wavelength neutrons, yielding an energy resolution of  $0.07 \text{ meV}$  at full width at half maximum (FWHM) at the elastic line, and an accessible  $Q$ -range in the range of  $0.21\text{--}2.08 \text{ \AA}^{-1}$ . Of

---

<sup>1</sup>This chapter is partially build up on on my Licentiate thesis [1].

relevance to this thesis, the IN6 instrument was chosen to probe the fundamental steps of proton diffusion in hydrated  $\text{BaZr}_{0.90}\text{Sc}_{0.10}\text{O}_{2.95}$  and  $\text{BaZr}_{0.50}\text{Sc}_{0.50}\text{O}_{2.75}$  (Paper I). More specifically, IN6 allowed for detection of proton transfers and rotational motions on the picosecond timescale.

TOFTOF is an instrument at the FRM II Neutron Source in Garching, Germany. The beam is monochromatized and pulsed by seven fast rotating disc choppers, and is then focused onto the sample by a converging super-mirror. The scattered neutrons are detected by 1000 He detectors covering scattering angles between  $7^\circ$  and  $140^\circ$  [193]. In our study, TOFTOF was operated with  $2.5 \text{ \AA}$  incident wavelength neutrons, yielding an energy resolution of  $0.45 \text{ meV}$  at FWHM at the elastic line, and an accessible  $Q$ -range of  $0.35\text{--}4.72 \text{ \AA}^{-1}$ . In this thesis, TOFTOF was used as a complementary tool to IN6 for further studies of the proton transfers and rotational motions in the hydrated  $\text{BaZr}_{0.90}\text{Sc}_{0.10}\text{O}_{2.95}$  and  $\text{BaZr}_{0.50}\text{Sc}_{0.50}\text{O}_{2.75}$  (Paper I). In more detail, the wide  $Q$ -range offered by TOFTOF was especially useful for analysis of the geometry of these localized processes. This wide  $Q$ -range offered increased statistics and more physically reasonable values of the analyzed parameters. Overall, these two instruments allowed for thorough investigation on the effect of the doping concentration on the localized proton dynamics in Sc-doped  $\text{BaZrO}_3$ .

FOCUS is a TOF instrument at The Paul Scherrer Institute (PSI), Switzerland. A horizontally and vertically focusing monochromator with variable curvature in both directions focuses the beam through a Fermi-chopper on the sample. The scattered neutrons are detected by 375  $^3\text{He}$  counter tubes of rectangular shape. The scattering angle covers a range from  $10^\circ$  and  $130^\circ$  [194]. For our experiments, FOCUS operated with  $6 \text{ \AA}$  incident wavelength neutrons, providing an energy resolution at the FWHM of the elastic line of  $\sim 40 \text{ \mu eV}$  and an accessible  $Q$ -range of  $0.2\text{--}2 \text{ \AA}^{-1}$ . In regards to this thesis, FOCUS was used as an additional tool for investigation of fast localized proton motions (of few tens ps) in hydrated  $\text{Ba}_2\text{In}_{1.85}\text{M}_{0.15}\text{O}_5$  with  $\text{M} = \text{In, Ga, Sc and Y}$  (Paper II). Additionally, the inelastic part of the measurements were also subjected to further analysis in these materials. Schematic drawing of IN6, TOFTOF, and FOCUS configurations based on a direct geometry setup is shown in Figure 5.1 a).

As part of this thesis, the backscattering instrument BASIS, at the Spallation Neutron Source (SNS) at Oak Ridge National Laboratory, USA was used for analysis of the localized proton motion in hydrated  $\text{Ba}_2\text{In}_{1.85}\text{M}_{0.15}\text{O}_5$  with  $\text{M} = \text{In, Ga, Sc and Y}$  (Paper II). BASIS is characterized with an energy resolution up to  $3.5 \text{ \mu eV}$  with Si(111) analyzer, and accessible timescales from 2 ps to 0.1 ns [195]. Access to an extended  $Q$  range up to  $3.8 \text{ \AA}^{-1}$  can be achieved by switching to Si(311) analyzer. For our experiments, the spectrometer operated with Si(111) analyzer, yielding an energy resolution of  $3.5 \text{ \mu eV}$  at FWHM at the elastic line, and an accessible  $Q$ -range of  $0.2\text{--}2.0 \text{ \AA}^{-1}$ . Specifically, the high resolution of BASIS was a key to obtain information of slower localized motions on the hundred picosecond timescale, associated with an additional site in these materials, as well as the presence of long-range dynamics in these materials. Ultimately, this measurement allowed for detailed investigation on the proton diffusion and its effect on the nature of dopant atom in  $\text{Ba}_2\text{In}_{1.85}\text{M}_{0.15}\text{O}_5$  with  $\text{M} = \text{In, Ga, Sc and Y}$ . Schematic drawing of a traditional backscattering instrument configuration based on an indirect geometry is shown in Figure 5.1 b).

A comparison of some important characteristics of the instruments used in this thesis are presented in Figure 5.2.

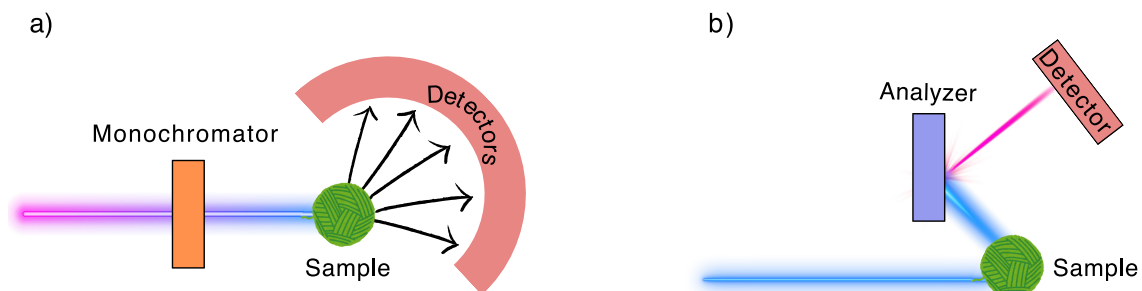


Figure 5.1: Schematic drawing of a) direct geometry (IN6, TOFTOF, FOCUS) and b) indirect geometry (BASIS) instrumental setup.

	IN6, ILL	TOFTOF, FRM II	FOCUS, PSI	BASIS, SNS
NEUTRON SOURCE	Reactor source	Reactor source	Spallation source	Spallation source
NEUTRON FLUX	$1.5 \cdot 10^{15}$ neutrons/s $\text{cm}^2$	$10^{14}$ neutrons/s $\text{cm}^2$	$10^{14}$ neutrons/s $\text{cm}^2$	60 pulses/s
INSTRUMENT TYPE	Time-of-flight (direct geometry) $E_i$ is fixed by graphite crystal	Time-of-flight (direct geometry) $E_i$ is fixed by choppers	Time-of-flight (direct geometry) $E_i$ is fixed by choppers	Backscattering (indirect geometry) $E_i$ is fixed by analyzer
WAVELENGTH	5.1 Å	2.5 Å	6 Å	6.267 Å
PROBED TIMESCALE	Picosecond (100 ps)	Picosecond to ns (up to 50 ns)	Picosecond (100 ps)	Picosecond to nanosecond
PROBED Q RANGE	0.21-2.08 Å <sup>-1</sup>	0.35-4.72 Å <sup>-1</sup>	0.2-2.0 Å <sup>-1</sup>	0.2-2.0 Å <sup>-1</sup>

Figure 5.2: Some characteristics of the IN6, TOFTOF and BASIS instruments used for QENS measurements in this thesis.

## 5.2 Infrared spectroscopy

In the past, IR spectrometers were equipped with various prisms, detectors and diffraction accessories connected to a recorder. Nowadays, IR spectrometers use interferometers and Fourier transform data processors, and are known as Fourier transform IR spectrometers (FTIRs) [183, 190, 196].

The basic working principle of a FTIR spectrometer is as follows: a IR light source (usually IR radiation obtained from a heated ceramic material) is defined by an aperture and is partially transmitted and partially reflected to a moving mirror by a beam splitter. The moving mirror creates an interferogram which is then Fourier transformed into a spectrum [197]. FTIR spectrometers are single-beam instruments, which means that both background and sample spectra need to be recorded as separate measurements. The final spectrum is then obtained by the ratio of the two spectra. The FTIR spectrometer used for this thesis is a Thermo Scientific Nicolet Nexus instrument and the two sampling techniques used in this thesis are the transmittance mode for the film samples and diffuse reflectance mode for the powder samples. A schematic drawing of the two modes is shown in Figure 5.4.

## Transmittance mode

The transmittance mode is based on the principle that the incident light passes through the whole sample and a spectrum is recorded. Although quite simple and straightforward method, the transmittance mode is often complicated by the sample's thickness, and/or lattice to substrate mismatch (for films samples) [181, 190]. Additional data manipulation is often needed. In this thesis the film samples (Paper III) were measured in transmittance mode in both air and argon atmosphere at room temperature. A reference spectrum was taken on the  $\text{Al}_2\text{O}_3$  substrate which is almost transparent in the IR range. The absorbance spectra was then derived by taking the logarithmic ratio between the reference and sample spectrum. It is important to point out that for the proton-conducting films in paper III, due to the large thickness of the substrate there was a strong interference which was smoothed using the Savitzky-Golay algorithm in the Thermo Scientific OMNIC FTIR software.

## Diffuse reflectance mode

The diffuse reflectance mode in infrared spectroscopy collects the diffuse reflection of the incident light by the powder's surface reflection in all directions and directs in towards the detector [181, 190]. This mode is especially useful for rough surfaces, such as powder samples. In this thesis the proton-conducting powder samples were subjected to diffuse reflectance infrared spectroscopy measurements. The reference measurement is often collected from a perfect diffuse scatterer, such as wrinkled aluminum foil or a specialized accessory offered by the instrument [181, 190]. In this thesis, the proton conducting powder samples (prior and after proton incorporation) were measured using the diffuse reflectance background accessory (mimicking perfect diffuse scattering) as a reference (background) spectrum. The absorbance spectra was then derived by taking the logarithmic ratio between the reference and sample spectrum. All of the measurements were performed in air at room temperature.

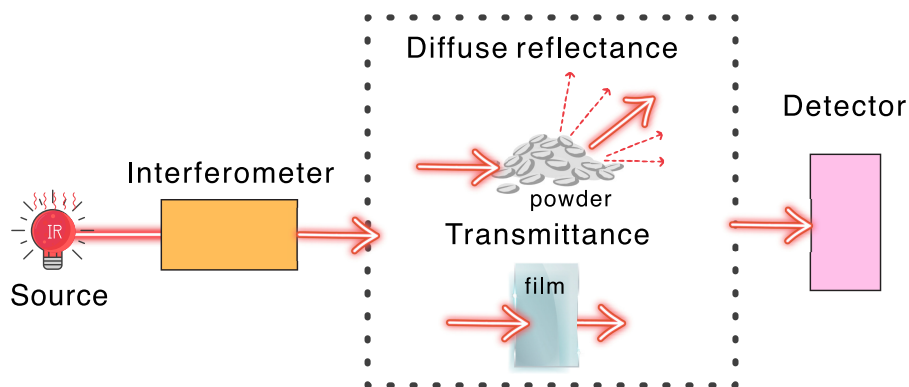


Figure 5.3: Simplified schematic drawing of FTIR spectrometer operating in a diffuse reflectance or in a transmittance mode.

## 5.3 Thermogravimetric analysis

The instrument used for this work is the STA 409 PC Luxx thermal and calorimetric analyzer which operates within temperatures up to 2000 °C. The instrument is consisted of a thermobalance which includes an electronic balance (microgram precision), a temperature-programmable furnace and computer-driven controller which enables simultaneous heating and weighing of a sample. Figure 5.4 shows a schematic drawing of the components of the instrument. The working principle is as follows; first, the sample is placed and weighed in a crucible (for our experiments an alumina crucible was used due to its resistance to high temperature and non-reactivity with the  $\text{BaZrO}_3$ ,  $\text{BaTiO}_3$  and  $\text{Ba}_2\text{In}_2\text{O}_5$  powders). Then, the sample is heated to higher temperatures with a constant heating rate, or in our case between 800–1000 °C with 5–10 °C/min. The sample is situated within an enclosed system ensuring a gaseous atmosphere of the measurement. In our case the instrument was connected to nitrogen gas to prevent possible oxidation for the measurements of the proton-conducting materials. The oxyhydride materials were, in turn, measured in air to allow for an oxidation and avoid formation of oxynitrides [64].

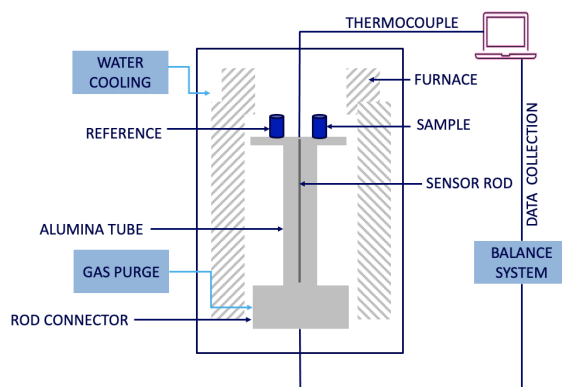


Figure 5.4: Schematic drawing of the STA 409 PC Luxx thermal and calorimetric analyzer's configuration. The sample is put on the balance within the furnace and mass change is detected as a function of temperature. This figure has been also used in my Licentiate thesis.



---

# 6 Overview of Findings

It is a wild dance floor there at the molecular level.

---

*Roald Hoffmann*

This chapter summarizes the key results obtained from my study on the local structure and dynamics in proton-conducting and hydride-ion conducting materials. It is structured as the following; in section 6.1, I describe the effect of doping concentration on the local structure and dynamics in Sc-doped BaZrO<sub>3</sub> proton-conducting materials (Paper I [198] and Paper III [199]); in section 6.2, I discuss the relationship between the nature of dopant atom and local structure and dynamics in Ba<sub>2</sub>In<sub>2</sub>O<sub>5</sub>-based proton-conducting materials (Paper II); in section 6.3, I give an overview of key parameters that influence the hydride-ion incorporation and diffusion in BaTiO<sub>3</sub> and In-doped BaZrO<sub>3</sub> oxyhydrides (Paper IV).

## 6.1 Unraveling the effect of doping concentration on local structure and dynamics

The effect of the doping concentration on the proton diffusion and local proton environments was studied on a series of Sc-doped BaZrO<sub>3</sub> powders and thin films. Sc as a dopant atom was chosen due to its similarity in size to Zr, which results in a cubic structure for higher doping concentrations, allowing for a more detailed study on the effect of the dopant atom in acceptor-doped BaZrO<sub>3</sub> materials.

Research on the effect of varying Sc doping concentrations on proton mobility has so far been limited to low doping levels up to 20% [108, 115, 200, 201]. These studies indicate that the localized proton diffusion occur on the picosecond timescale, with only a minor effect on doping concentration. However, further investigations involving significantly higher doping concentrations are necessary to fully understand how increased doping influences proton mobility. Therefore, this study has been focused on investigation of the localized proton dynamics using QENS on two hydrated powder samples with significantly different Sc-doping concentration, namely BaZr<sub>0.90</sub>Sc<sub>0.10</sub>O<sub>2.95</sub> (10Sc/BZO) and BaZr<sub>0.50</sub>Sc<sub>0.50</sub>O<sub>2.75</sub> (50Sc/BZO).

Analysis of the fitting parameters revealed localized dynamics in the picosecond timescale, below 8 ps for both materials and consistent with previous QENS studies on 10Sc/BZO [108, 113, 115, 176]. The activation energy for these dynamics was found to be in the range of 8–40 meV, and it was slightly lower for 50Sc/BZO than for 10Sc/BZO. The geometry of the motion has been described

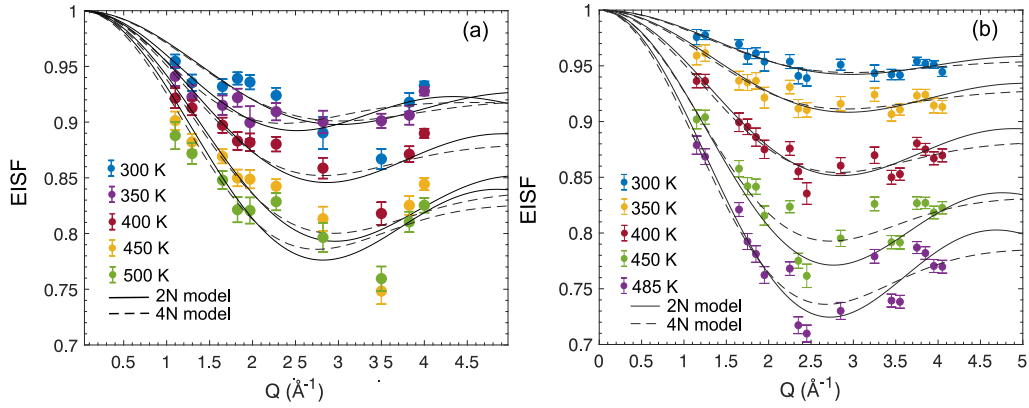


Figure 6.1: EISFs for (a) 10Sc/BZO and (b) 50Sc/BZO, as derived from the TOFTOF data. The lines are fits to the jump-diffusion model over two (2N) and four (4N) sites.

with a contribution from both proton transfer and orientational motions, as shown in Figure 6.1. Additionally, a marginally larger fraction of mobile protons in 50Sc/BZO was found to be released at higher temperatures, associated with lower trial frequencies.

The lower activation energy observed in 50Sc/BZO may be linked to the increased proportion of asymmetric units, rising from 20% in 10Sc/BZO to 50% in 50Sc/BZO, assuming that the Sc-dopants are dispersed randomly within the matrix. Since the activation energy for proton transfer correlates with the jump length, shorter average jump distances may also account for the lower activation energy observed in 50Sc/BZO in accordance to studies on Sc-doped  $\text{BaZrO}_3$ , and similar  $\text{BaZrO}_3$  systems doped with Y or In [106, 122, 176]. Furthermore, these differences could originate from modification of the lattice dynamics, such as a shift of phonon frequencies to lower energies involved in the proton transfer process, or the presence of additional localized oxygen modes. The increased presence of asymmetric units Sc–O–Zr in 50Sc/BZO could also contribute to these effects. This structural change likely promotes a relatively higher population of proton transfers with shorter jump distances, which could explain the lower activation energy, as previously reported on 10% Sc- and Y-doped  $\text{BaZrO}_3$  [108, 115, 176, 177]. The results indicate that significant increase of the Sc dopant concentration from 10% to 50%, has little effect on the localized proton dynamics, its timescale, and its activation energy. This finding is of relevance for future industrialization of these materials for fuel cell technologies, as it suggests that the application of lower doping concentration can not only have (virtually) the same effects in terms of proton diffusion, but also lower the fabrication costs and decrease the demand of critical raw materials (one of which is Sc).

In my thesis, I also investigated the effects of doping concentration on the local structure and coordination of protons in Sc-doped  $\text{BaZrO}_3$  films. Such insights are particularly important, as for application in fuel cells, the material should be in a thin film form [8, 17, 27, 77]. Understanding the differences between the local structure and coordination of protons in films and powders can, therefore, help to facilitate the commercial development of these materials. More specifically, the nature of the local structure and coordination environment of protons, as well as their dependence on the morphology of nanocrystalline  $\text{BaZr}_{1-x}\text{Sc}_x\text{O}_{3-x/2}$  films with  $x = 0.45, 0.54, 0.65$  were investigated using IR spectroscopy. The proton concentration in each sample was determined by NRA, revealing that the hydration levels of the films range from 28% for  $x = 0.45$ , to 22% for  $x = 0.54$ , and to 19% for  $x = 0.64$ ; As shown in Figure 6.2, the proton concentration across all doping concentrations remains below 30% (of 100% which corresponds to full hydration). A significant portion of protons is localized near the surface, as opposed to a relatively low proton concentration observed in the

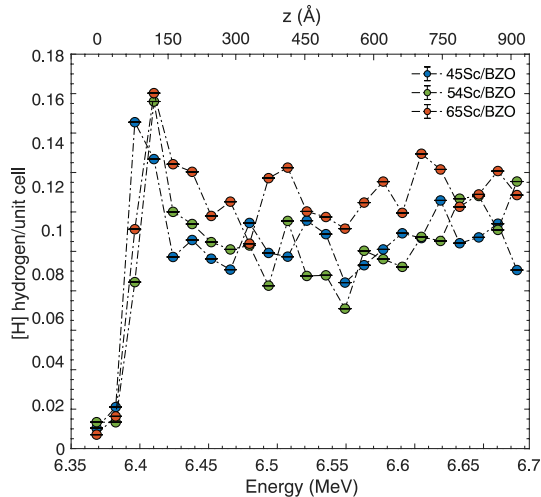


Figure 6.2: Hydrogen concentration of the hydrated film samples of  $\text{BaZr}_{1-x}\text{Sc}_x\text{O}_{3-x/2}$  with  $x = 0.45, 0.54,$  and  $0.65$  (45Sc/BIO, 54Sc/BIO and 65Sc/BIO, respectively) as derived from NRA. The top axis shows the estimated penetration depth. The error bars were calculated as a standard deviation with 95% certainty and are within the data points. (Paper III).

bulk of the film.

Crucially, IR spectroscopy measurements revealed notable differences among the samples, as seen in Figure 6.3. In general the IR spectra of Sc-doped  $\text{BaZrO}_3$  powders are characterized by a broad, dominant O-H stretch band, due to presence of various local proton environments in the materials. Specifically, the lower-frequency region of the O-H band ( $2500\text{--}3000\text{ cm}^{-1}$ ) corresponds to protons in non-symmetrical environments, such as  $\text{Zr-O-Sc}$ , while the higher-frequency region ( $3000\text{--}3700\text{ cm}^{-1}$ ) is associated to protons in symmetrical environments, such as  $\text{Zr-O-Zr}$  and  $\text{Sc-O-Sc}$  [107]. Variations in the band profiles with increasing Sc dopant concentrations reflect differences in the distribution of protons across these different sites. In contrast, the spectra of the hydrated thin films display markedly different features. These IR spectra show significantly weaker and narrower bands, indicating a less homogeneous proton distribution, with a larger fraction of protons in symmetric, weakly hydrogen-bonding configurations. Specifically, Figure 6.3 (b) shows the IR absorbance spectra for the hydrated film samples of  $\text{BaZr}_{1-x}\text{Sc}_x\text{O}_{3-x/2}$  with  $x = 0.45, 0.54,$  and  $0.64$ . For  $x = 0.45$ , the spectrum shows a broad, weak band similar as the one observed in the powders. At  $x = 0.54$ , distinct bands emerge around  $3400\text{ cm}^{-1}$  and  $3700\text{ cm}^{-1}$ , with the former one being notably more intense. For  $x = 0.64$ , the spectrum resembles that of  $x = 0.54$ , but the band initially at  $3400\text{ cm}^{-1}$  appears up-shifted to approximately  $3500\text{ cm}^{-1}$ , and the  $3700\text{ cm}^{-1}$  band diminishes in intensity.

By integrating the findings from the IR spectral analysis of both nanocrystalline films and microcrystalline powder samples, several key observations can be made (Figure 6.3). The appearance of a prominent and intense band at around  $3400\text{--}3500\text{ cm}^{-1}$  for higher Sc dopant concentrations ( $x = 0.54$  and  $0.64$ ), suggests that proton distribution in the films becomes less uniform. In more detail, a larger proportion of protons occupy relatively symmetric and weakly hydrogen-bonded configurations, compared to the lower-doped film ( $x=0.45$ ) and the powder systems. This indicates that a compositional threshold for the development of such preferred proton sites likely exists between  $x = 0.45$  and  $x=0.54$ , beyond which the spectral features tend to converge. Moreover, the elevated proton concentration near the surface points to the potential presence of a proton-rich top

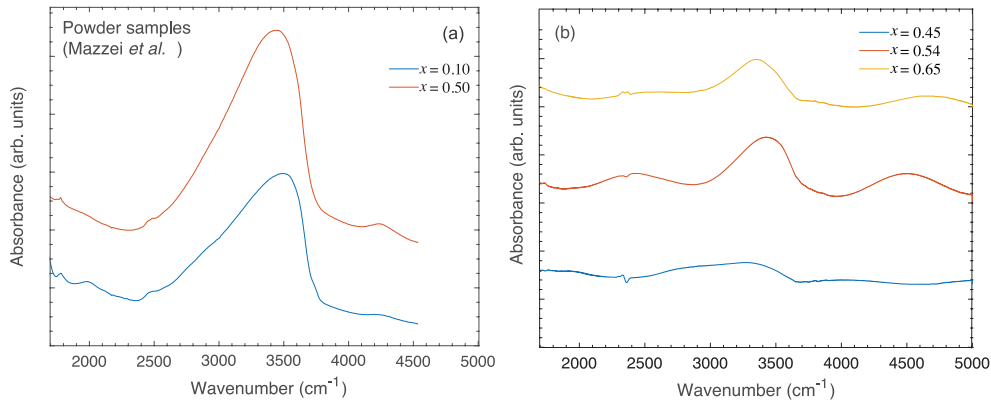


Figure 6.3: Comparison between the O–H region of the bulk powder samples from ref. [122] (a) and the film samples prepared by magnetron co-sputtering (b).

layer, a feature also reported in recent study of a 50 nm-thick  $\text{BaZr}_{0.53}\text{In}_{0.47}\text{O}_{2.77}$  film [189]. This suggests that formation of such a proton-rich surface layer may be a common characteristic of proton-conducting perovskite films. Overall, the results point towards a significant difference in the local proton environments in thin film samples which are primarily dominated by protons in symmetrical sites. The reasoning behind such preferred proton sites could be potentially linked to the low hydration degree in the films, which decreases systematically with increasing Sc concentration, as opposed to the fully hydrated powder samples. This suggests that factors beyond high Sc doping concentration, and related to the fabrication method itself, such as stress or lattice-mismatch with the substrate, influence the formation of such unique O–H stretch band.

To address this speculation, further investigation was conducted. Thin films of  $\text{BaZr}_{1-x}\text{Sc}_x\text{O}_{3-x/2}$  with  $x = 0.10, 0.20, 0.30$  were prepared using PLD with powders serving as targets. The powders were then fully characterized; XRD analysis confirmed the presence of a phase-pure cubic structure (Pm3m); the powders showed polycrystalline grains with sizes ranging from 700 nm to 900 nm. Figure 6.4 summarizes the characterization results.

The films along with with a small portion of the powder targets were hydrated at the same time

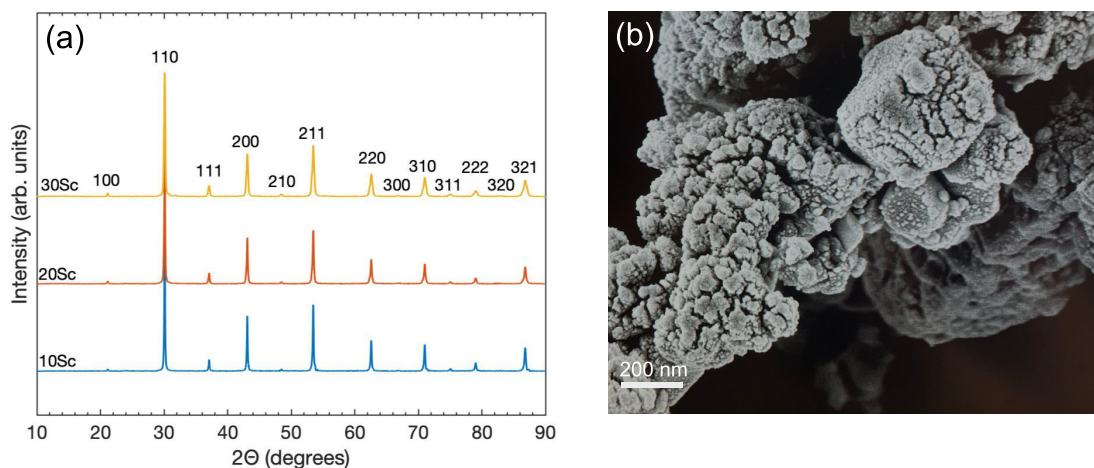


Figure 6.4: XRD patterns for  $\text{BaZr}_{1-x}\text{Sc}_x\text{O}_{3-x/2}$  films with  $x = 0.10, 0.20, \text{ and } 0.30$  (a) and SEM image of  $\text{BaZr}_{0.80}\text{Sc}_{0.20}\text{O}_{2.90}$  (b).

to verify that the hydration is successful. Figure 6.5 shows the IR absorbance spectra of the hydrated powders (a) and thin film (b) samples of  $\text{BaZr}_{1-x}\text{Sc}_x\text{O}_{3-x/2}$  with  $x = 0.10, 0.20,$  and  $0.30$ . Generally, the powders are characterized with a broad O–H stretch band, indicating a diverse distribution of proton sites and in accordance with the literature [1, 97, 196]. On contrary, no distinct O–H stretch band is observed in any of the films across the different doping concentrations. While the cause of this is unknown, we speculate that conditions related to the PLD deposition or the substrate itself are responsible for lack of oxygen vacancies. These results further support the implication that factors related to film fabrication such as stress or lattice-substrate mismatch contribute to low (or absent) degree of proton concentration, especially since protons (and distinct O–H stretch band) could be observed in the powders used as targets. These results give further insights into the relationship between local proton environments in films, and the fabrication methods used. The results also highlight the importance of developing and optimizing a fabrication method for depositing films that have properties similar to those observed in the powders.

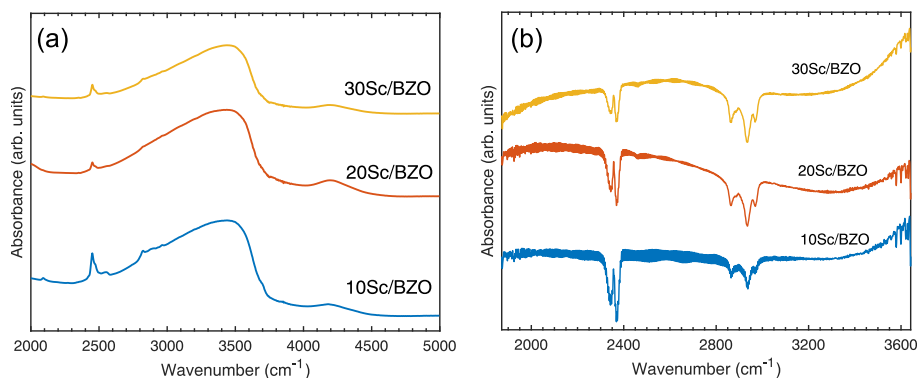


Figure 6.5: IR absorbance spectra of hydrated  $\text{BaZr}_{1-x}\text{Sc}_x\text{O}_{3-x/2}$  powders (a) and films prepared by PLD (b) with  $x = 0.10, 0.20,$  and  $0.30$ .

## 6.2 Elucidation of the relationship between type of dopant atom and local structure and dynamics

Recent studies on hydrated  $\text{Ba}_2\text{In}_2\text{O}_5$ , based on INS and QENS, revealed the presence of two types of proton sites, H(1) and H(2), associated with proton rotational motions and proton transfers, respectively, with activation energies  $E_a$  between 10–20 meV [93, 129]. Additionally, a third site, acting as a saddle point for proton transfers and rotational motions was identified, with  $E_a = 35$  meV, in the timescale of 45–77 ps. The effect on the dopant atom in a doped  $\text{Ba}_2\text{In}_2\text{O}_5$ , i.e.  $\text{Ba}_2\text{In}_{1.85}\text{M}_{0.15}\text{O}_5$  with  $M = \text{Ga}, \text{Sc}$  and  $\text{Y}$  was also investigated using INS and IR spectroscopy [135]. The study showed that the nature of the dopant has only a minor effect on the populations of these two proton sites, H(1) and H(2).

Building upon these insights, this present study was focused on investigations on the effect of the nature of dopant atom on the localized dynamics in  $\text{Ba}_2\text{In}_{1.85}\text{M}_{0.15}\text{O}_5$  with  $M = \text{In}, \text{Ga}, \text{Sc}$  and  $\text{Y}$ . The study is a continuance of the latter two investigations, and it aims to provide more detailed information regarding the relationship between the nature of the dopant atom and its localized dynamics. Hydrated powder samples of  $\text{Ba}_2\text{In}_{1.85}\text{M}_{0.15}\text{O}_5$  with  $M = \text{In}, \text{Ga}, \text{Y}$  and  $\text{Sc}$ , hereafter referred to as BIO, Ga/BIO, Y/BIO and Sc/BIO were analyzed using QENS. Analysis of

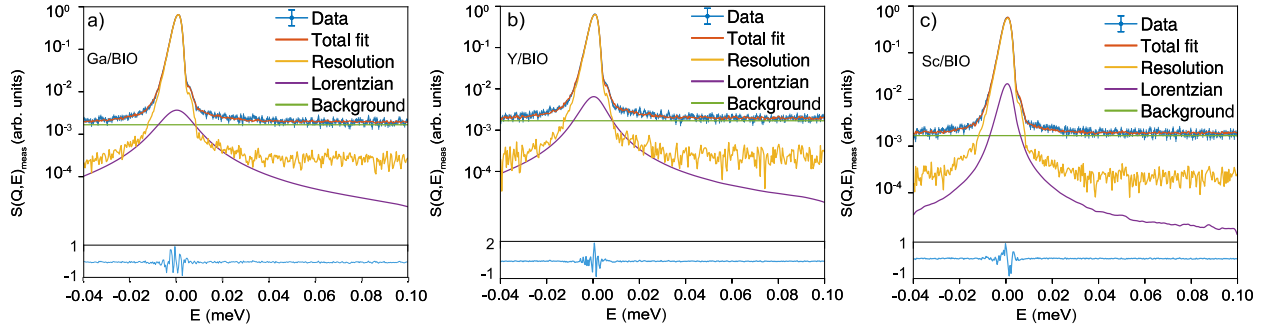


Figure 6.6:  $S(Q, E)_{\text{meas}}$  together with fits for (a)  $\text{Ba}_2\text{In}_{1.85}\text{Ga}_{0.15}\text{O}_5$ , (b)  $\text{Ba}_2\text{In}_{1.85}\text{Y}_{0.15}\text{O}_5$  and (c)  $\text{Ba}_2\text{In}_{1.85}\text{Sc}_{0.15}\text{O}_5$  at  $T = 4900$  K for  $Q = 1.50 \text{ \AA}^{-1}$ .

the data for the undoped material, BIO, did not reveal a significant quasielastic scattering signal at any of the tested temperatures ( $T = 400, 490,$  and  $600$  K). Although the exact cause remains unclear, this absence is likely attributed to the presence of more stable protons with stronger bonding in the material which are not mobile at these temperatures, as suggested by the TGA measurements characterized with a rapid release of protons at temperatures above  $700 \text{ }^\circ\text{C}$  (see Supporting Information of Paper II), and in accordance with several other reports [92, 129].

Analysis of the doped materials, M/BIO (where  $M = \text{Ga}, \text{Y},$  and  $\text{Sc}$ ) showed that the dependence of the FWHM on  $Q$  varies with temperature. Up to  $T = 490$  K, the FWHM showed no significant  $Q$ -dependence (within error), for any of the three materials. However, for  $T = 600$  K, the FWHM was found to increase with increasing  $Q$ , as shown in Figure 6.7. This was related to the presence of localized dynamics with timescales in the range of  $100$ – $220$  picoseconds for temperatures up to  $490$  K, and a long-range diffusion at  $600$  K, quite independent of  $M$ . It is worth noting that the timescale for localized dynamics in  $\text{Sc/BIO}$  [ $700(90)$  ps] was disregarded on the basis that it is likely attributed to a weak quasielastic signal that exceeds the instrument resolution as shown in Figure 6.6 c). The localized dynamics was shown to have contributions from both proton transfers and rotational motions, quite independent of  $M$ , as shown in Figure 6.8, and in accordance to studies on  $\text{Ba}_2\text{In}_2\text{O}_5$ , and other cubic-structured proton conductors [129, 202, 203].

A (virtually) constant value of the immobile fraction was observed, independent of  $M$ . The values are similar to those reported for  $\text{Ba}_2\text{In}_2\text{O}_5$ , with  $c = 90(3)\%$  to  $82(2)\%$  for  $T = 400$ – $485$  K [129]. On the contrary, systematic decrease of  $c$  down to  $50$ – $60\%$  is common for various cubic

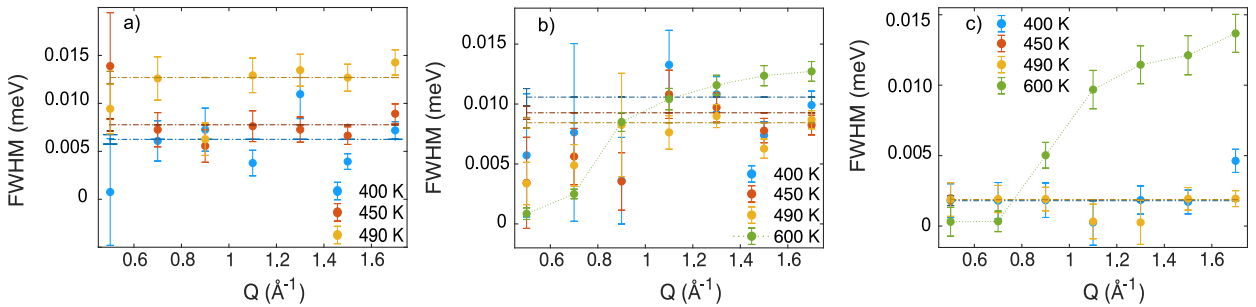


Figure 6.7: Temperature evolution of the FWHM for (a) Ga/BIO, (b) Y/BIO and (c) Sc/BIO, as derived from the Si(111) data. Dashed lines represent the  $Q$ -average value for each temperature.

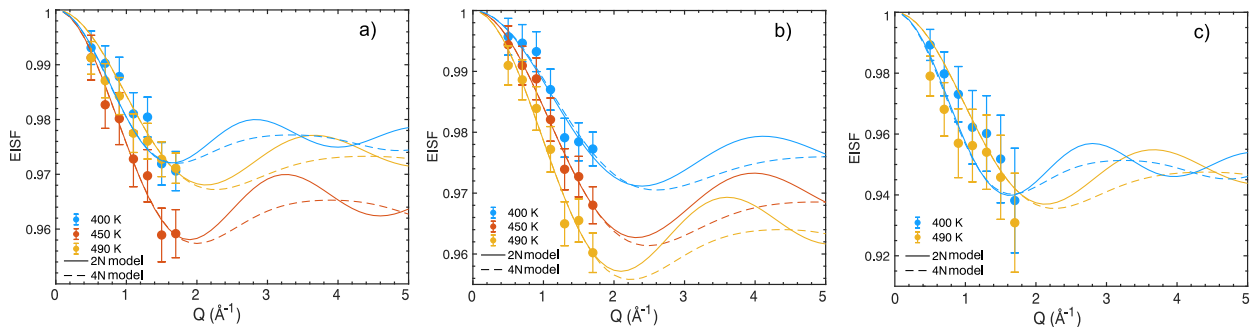


Figure 6.8: EISFs for a) Ga/BIO, b) Y/BIO and c) Sc/BIO, as derived from the BASIS data. The lines are fits to the jump-diffusion model over two ( $N = 2$ ) and four ( $N = 4$ ) sites.

proton conductors, such as for example for Y- and Sc-doped  $\text{BaZrO}_3$  [176, 198, 203, 204]. The higher fraction of immobile protons in brownmillerite-structured materials than in cubic-structured materials could be related to a presence of a slower proton dynamics, which could be rationalized as dynamics of protons too slow to be detected in the instrumental "time window". It can also be explained by a population of strongly-bonded protons, not found in cubic proton conductors, which are present not only at room-temperature but are also stable up to ca. 400 °C [92, 137], and persists well beyond the onset of dehydration and up to 700 °C. This is supported by the TGA results (Supporting Information, Paper II) with BIO showing a small gradual dehydration in the range of 400–700 °C followed up by a significant and rapid mass loss at 700 °C. The presence and persistence in temperature of these strongly-bonded protons are less pronounced in the M-doped materials, by the lower dehydration temperature of ca. 300 °C for Ga/BIO, Y/BIO and Sc/BIO. Note however that the temperature of dehydration in M/BIO is significantly higher than in cubic-structured materials, typically at ca. 200 °C [106, 202, 204], which suggest that these strongly-bonded protons are likewise present in the doped M/BIO materials. The long-range dynamics observed at 600 K, independent of M, was attributed to a series of jumps with a fixed jump length of around 2.5 Å and an average relaxation time of around 120 ps, as per the Chudley-Elliott model [178]. As an example, Figure 6.9 shows fits of this model to the Y/BIO and Sc/BIO data.

A key result in this study is in the difference of the timescale of proton dynamics in the undoped BIO and M/BIO materials, as only the M/BIO materials show proton dynamics in the here probed range of 30 -300 ps. As all materials have similar hydration degree, the difference in such timescale of the dynamics may indicate difference in local environment of protons in BIO, as opposed to M/BIO. Peak-fit analysis of the IR spectra however, showed a quite similar ratio of the number of H(1) protons to H(2) protons for all materials, pointing out that the difference in dynamics between BIO and M/BIO may be, instead, related to the H(3) site (Supporting Information, Paper II). In this regard, we speculate that the absence of dynamics in BIO may be related to lack of site availability of H(3) due to proton saturation in the BIO structure. Specifically, cation substitution is an effective route for lowering the amount of protons [129], which may also explain the weak effect of the nature of dopant atom, considering that the doping concentration for all M/BIO is the same. The lower amount of protons in M/BIO, hence increases the probability for occupation of the H(3) site. Assuming that the occupation of H(3) sites enables long-range diffusion, then larger availability of the H(3) site would translate into faster long-range diffusion, as observed in our QENS measurements. This suggests that doping the  $\text{Ba}_2\text{In}_2\text{O}_5$  system decreases the occupation of such sites, thereby facilitating long-range proton diffusion. Such insight could potentially contribute to

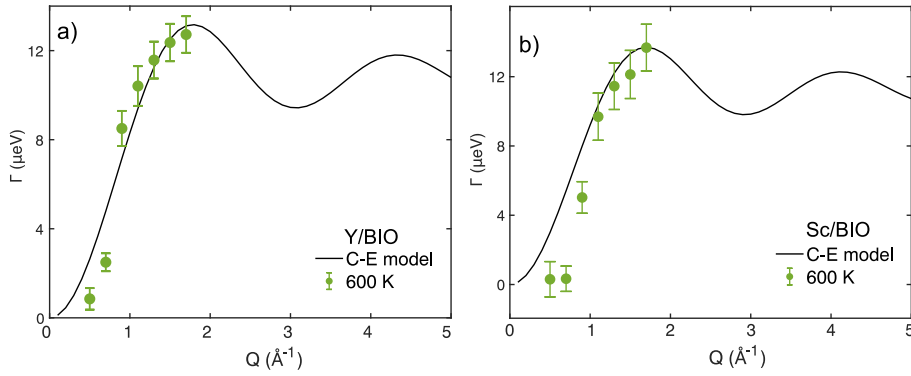


Figure 6.9:  $Q$ -dependence of the FWHM at  $T=600$  K for a) Y/BIO and b) Sc/BIO. The lines are fits to the C-E model.

further optimization of these materials for fuel cell technologies by expanding the application of different (and more economic) dopant atoms.

### 6.3 Local structure and dynamics in perovskite-type oxyhydrides

In this study, initially based on synthesis of oxyhydrides, LiH was used as a reducing agent for  $\text{BaTiO}_3\text{H}_x$ . TGA experiments were conducted to verify successful reduction and possibly hydride-ion incorporation. As shown in Figure 6.10, the  $\text{BaTiO}_3$  oxyhydride is characterized with a notable increase in mass, suggesting successful reduction and hydride-ion incorporation. The hydride-ion concentration was quantified through solid-state NMR measurements, revealing hydride-ion molar ratio of  $x=0.12$ .

The hydride-ion diffusion in  $\text{BaTiO}_{2.88}\text{H}_{0.12}$  oxyhydride was further investigated using QENS. Interestingly, the study showed an absence of any diffusional process within the material, indicating that oxygen vacancies are essential for hydride-ion diffusion. The study likewise investigated the hydride-ion dynamics in  $\text{BaTiO}_{2.67}\text{H}_{0.12}\square_{0.21}$  oxyhydride; overall, the hydride-ion diffusion in this

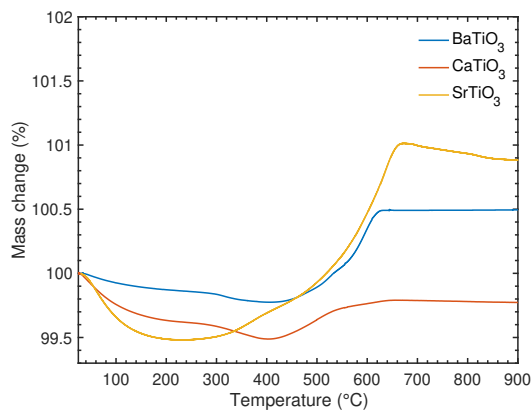


Figure 6.10: TGA curves of  $\text{BaTiO}_3$ ,  $\text{SrTiO}_3$  and  $\text{CaTiO}_3$  oxyhydrides measured in air.

oxyhydride with oxygen vacancies, was shown to be a two-timescale dynamics: a faster dynamics component ranging between 2–6 ps, likely associated with hydride-ion diffusion in vacancy-rich environments, and a slower dynamics component between 20–40 ps, possibly linked to hydride-ion diffusion in vacancy-poor areas. A high percentage of the hydride ions was found to be immobile on the here probed timescales, which further indicates that these mobile hydride ions are related to a certain local environment in the material. The nature of such specific local environment remains to be investigated, but could result from the existence of regions relatively rich in anion vacancies which could be found, for example, in the vicinity of grain boundaries. A key result in this study is the necessity of oxygen vacancies for hydride-ion dynamics in  $\text{BaTiO}_{2.88}\text{H}_{0.12}$ . Furthermore the presence of specific local environments present in the oxygen deficient  $\text{BaTiO}_{2.67}\text{H}_{0.12}\square_{0.21}$  sheds light on the relationship between the oxygen vacancies and hydride-ion dynamics. If this relationship is further explored, synthesis of these oxyhydrides with an optimal number of oxygen vacancies could contribute to optimization of materials with desirable hydride-ion conductivity for their final applications in fuel cells. In this thesis, I have also synthesized  $\text{SrTiO}_3$  and  $\text{CaTiO}_3$  oxyhydrides with  $\text{CaH}_2$  as a reducing agent. The successful reduction of these materials was confirmed by TGA (Figure 6.10). It is worth pointing out, however, that the initial weight loss in the TGA shown in Figure 6.10 for all three materials can be due to loss of surface hydroxyl and secondary water [67]. The slightly bigger drop observed for the  $\text{CaTiO}_3$  oxyhydride may be due to the extensive washing, which could lead to increased amount of water absorption [67]. The hydride-ion concentration was quantified through solid-state NMR measurements, revealing hydride-ion molar ratios of  $x=0.13$  in the  $\text{SrTiO}_3$  oxyhydride. Unfortunately, no hydride-ions were detected in the  $\text{CaTiO}_3$  oxyhydride; this could be related to unfinished reduction process, which may indicate that repetition of the reduction process is needed. The  $\text{SrTiO}_3$  oxyhydride will be further investigated with QENS, with the aim to unravel the relationship between the A-site cation and hydride-ion dynamics. Such insights will contribute to a deeper understanding of the governing mechanism for hydride-ion diffusion which can help in optimization of these materials for fuel cell applications.

Note that understanding the relationship between synthesis parameters and hydride-ion incorporation and diffusion in oxyhydrides is also essential for further advancement in this relatively novel field of materials science. The topochemical route, as outlined in Chapter 3, requires special conditions and equipment, which may limit its practicality for large-scale production and industrial application. Motivated by the need for a more straightforward synthesis method for oxyhydrides, and inspired by a recent study on a hydrogen gas reduction route for synthesis of a new class of oxyhydride,  $\text{BaZr}_{0.50}\text{In}_{0.50}\text{O}_{2.25}\text{H}_{0.5}$  [70], this thesis focused on optimization of the hydrogen gas synthesis route for a broader range of perovskite oxyhydrides. Building upon results of the study in ref [70], additional compositions of  $\text{BaZr}_{1-x}\text{In}_x\text{O}_{3-x/2}$  oxyhydrides with  $x=0.10$  and  $0.20$  were synthesized with the hydrogen gas reduction method, allowing for a more systematic study. XRD patterns confirmed the preservation of phase-pure powders post-synthesis. TGA measurements showed slight oxidation, suggesting reduction of the material and possibly presence of a small amount of hydride-ions in the material. To verify hydride-ion incorporation, INS measurements were performed. As shown in Figure 6.11 b), no clear hydrogen-related peaks were detected in the samples. The reason for this is not fully clear, but can be related to extremely small amount of hydride ions. Assuming incorporation of hydride-ions is sensitive to the dopant concentration (and amount of oxygen vacancies present in the material),  $\text{BaZr}_{1-x}\text{In}_x\text{O}_{3-x/2}$  powders with  $x$  close to  $0.50$ , namely  $x=0.56$  and  $x=0.59$  were also investigated. TGA results revealed notable difference in mass increase, with  $x=0.56$  showing significantly higher increase (Figure 6.11 a)). This result indicated high sensitivity of hydride-ion incorporation to doping concentration. To further investigate this, a larger amount (ca. 5 grams) of the very same  $x=0.56$  powder batch underwent hydrogen reduction under the same

conditions used previously. Interestingly, TGA data showed a lower mass increase compared to the previously reduced material (0.1 grams), implying that that hydride-ions did not penetrate in the bulk materials as effectively at larger scales (Figure 6.11 a)). INS measurements on the 59In/BZO powder, however, showed no distinguishable hydrogen-related peaks. The reason for this remains unclear at present times, but can be related to a very small amount of hydride-ions which produced very weak (unnoticeable peaks) along with strong absorption in the material. It can imply that the material transformed into oxygen-ion conductor, rather than a hydride-ion conductor. Upcoming QENS experiments should give more insights regarding this cause.

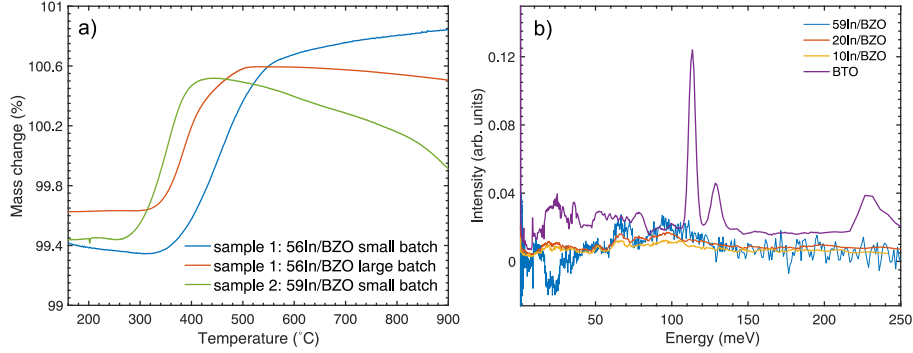


Figure 6.11: TGA curves of  $\text{BaZr}_{0.44}\text{In}_{0.56}\text{O}_{2.72}$  (sample 1: 56In/BZO) and  $\text{BaZr}_{0.41}\text{In}_{0.59}\text{O}_{2.71}$  (sample 2: 59In/BZO), measured in air (a). INS spectra at  $T = 10$  K of 10In/BZO and 20In/BZO and 56In/BZO; the purple line shows the data for  $\text{BaTiO}_{2.88}\text{H}_{0.12}$  (BTOH) measured on IN1 (proposal 7-01-550) for the comparison (b).

The science of today is the technology of tomorrow.

---

*Edward Teller*

The research results presented in this thesis have contributed to the fundamental understanding of proton diffusion and local proton environment in proton-conducting oxides, particularly perovskite and perovskite-like brownmillerite-type oxides. Additionally, this thesis has also provided more detailed and systematic results into the influence of different parameters for the local structure and dynamics in perovskite-type oxyhydrides. Referring back to the research questions outlined in Chapter, 1, this thesis provides valuable insights.

In addressing the research question, "What is the relationship between the doping concentration and the dynamics of protons, its activation energy, timescale and geometry in Sc-doped BaZrO<sub>3</sub> perovskites? Does it differ? How?", the findings reveal that the localized proton dynamics, is weakly affected by the Sc doping level within the here investigated range up to 50%. In more detail, studies on powder samples of BaZr<sub>1-x</sub>Sc<sub>x</sub>O<sub>3-x/2</sub> ( $x = 0.10$  and  $0.50$ ) confirmed that proton dynamics are localized and composed of proton rotational motions around a single oxygen atom, and transfers between neighboring oxygens. These processes occur on timescales below 10 ps, with activation energies ranging between 8 and 40 meV. The implications from this study suggest that Sc doping concentration has a minor effect on the proton dynamics, therefore providing further insights which can contribute to industrialization of these materials for fuel cell applications, considering that for large-scale applications, factors such as chemical composition have a significant economic impact. This research question was also further investigated on the effect of Sc dopant on the proton environments in BaZr<sub>1-x</sub>Sc<sub>x</sub>O<sub>3-x/2</sub>, ( $x = 0.45, 0.54, 0.65$ ) films prepared by magnetron co-sputtering. The goal was to better understand this research question from an application perspective, making the findings more relevant for real-application. The results revealed a diverse range of local proton environments for  $x = 0.45$ . In contrast, compositions with  $x = 0.54$  and  $0.65$  showed evidence of preferred, symmetric, weakly hydrogen-bonding proton configurations. Additionally, it was demonstrated that the local structural features of the studied films prepared by magnetron sputtering differ significantly from those observed in powder samples with comparable compositions, with the films exhibiting much homogeneous distribution of protons. On contrary, absence of proton incorporation was observed in the films prepared by PLD, as compared to the powder "targets" used for their deposition, which were characterized by a diverse range of local proton environments. The results on films fabricated by magnetron co-sputtering and PLD indicate that factors beyond chemical composition play role in the presence of such unique local structural features, hence highlighting the importance of advancement and optimization of fabrication methods on both lab- and large-scale.

In relation to the second research question "What are the effects of different dopants on the proton environments, proton diffusion, its timescale, and geometry of motion in  $\text{Ba}_2\text{In}_{1.85}\text{M}_{0.15}\text{O}_5$ ,  $\text{M} = \text{In, Ga, Y, and Sc}$  brownmillerite materials", the results demonstrated that doping the  $\text{Ba}_2\text{In}_2\text{O}_5$  structure with Ga, Y, and Sc, results in the presence of localized proton diffusion in the range of a hundred picoseconds. Doping was found to be an effective strategy for promoting the occupation of a saddle state which facilitates the interexchange of proton transfers and rotational motions, and for enabling long-range diffusion. The specific type of dopant atom was observed to have only a minor influence on the distribution of proton sites, as well as on the dynamics or timescale of the diffusional processes. These findings, overall, indicate that cation substitution has favorable influence on both the localized and long-range diffusion, whereas the specific dopant atom plays a minor role in the geometry or temporal characteristics of these processes. Such findings may contribute to application of a wider range of dopant atoms, some which are also more economic and applicable in industrial settings.

Regarding the remaining research questions related to synthesis of perovskite oxyhydride and the relationship between the compositional differences of the precursors and the hydride-ion incorporation and dynamics, the results reveal important new insights. In more detail, the study utilizing a topochemical synthesis route demonstrated that reducing agents other than  $\text{CaH}_2$ , such as  $\text{LiH}$ , can be employed to synthesize oxygen vacancy-free  $\text{BaTiO}_{2.88}\text{H}_{0.12}$ . However, the same material showed no signs of hydride-ion diffusion, indicating that the presence of oxygen vacancies is essential for facilitating hydride-ion diffusion. The study also revealed that hydride-ion diffusion relies on oxygen-vacancies, and that the timescale of this diffusion is dependent on the local environment of hydride ions, especially related to the vicinity of oxygen vacancies.

Additionally, the effect of the doping concentration on hydride-ion incorporation in a series of  $\text{BaZr}_{1-x}\text{Sc}_x\text{O}_{3-x/2}$ , ( $x = 0.20, 0.30, 0.56, \text{ and } 0.59$ ) using hydrogen gas reduction method was investigated. The findings indicate that doping concentration and synthesis parameters significantly influence the ability of hydride-ion incorporation. These findings indicate that advances in synthesis methods, allowing for controlled composition of oxyhydrides, is crucial for further advancement in this relatively new field of materials science.

With a view towards the future, this thesis has also raised new intriguing research questions worthy of further investigation. For instance, the findings for Sc-doped  $\text{BaZrO}_3$  powder and film samples show structural difference between the two, highlighting the need for additional investigation on the cause of this phenomenon. As one example, systematic study on the effect of fabrication parameters and compositional differences in these systems may help in developing films with features similar to the powder ones. Additionally, more detailed studies of the localized structure between films and powders using, for example, UV-Raman spectroscopy can possibly provide more details that can help optimize the films.

Further investigation on the influence of the dopant atom on the macroscopic conductivity in  $\text{Ba}_2\text{In}_{1.85}\text{M}_{0.15}\text{O}_5$ ,  $\text{M} = \text{In, Ga, Y, and Sc}$ , can, naturally, offer deeper insights into the relationship between nature of dopant atom, localized diffusion and macroscopic conductivity. Such insights could further contribute in optimization of these materials for their practical application. It would be also interesting to investigate the behavior of these systems in conditions used in fuel cell under operation. Additionally, investigation of  $\text{Ba}_2\text{In}_{1.85}\text{M}_x\text{O}_5$ ,  $\text{M} = \text{In, Ga, Y, and } x = 0.05\text{--}0.20$  would offer a more systematic study for the influence of the dopant atom concentration on the localized and long-range proton dynamics.

Regarding the synthesis methods, numerous approaches remain to be explored. As one example, optimizing parameters such as temperature and gas flow in hydrogen gas reduction method could give new insights to avoid structural decomposition. Extended systematic studies using both

topochemical and hydrogen gas reduction routes with different composition of precursors, reducing agents and temperatures may also bring new insights which will facilitate innovations in this relatively new field.

Furthermore, studies on the hydride-ion diffusion in a series of  $\text{BaTiO}_3$  oxyhydrides with different amount of oxygen vacancies could provide a more thorough understanding on the relationship between hydride-ion local environment and diffusion.



---

## Appendix A

### Fuel cells– brief considerations

Fuel cells are electrochemical devices that produce electricity through reactions between a fuel, typically hydrogen, and an oxidant, usually oxygen. There are different types of fuel cells, each distinguished by their electrolyte material and operating conditions beyond SOFCs, which is explained in Chapter 2 of this thesis. Other type of fuel cells include proton exchange membrane fuel cells (PEMFCs), molten carbonate fuel cells (MCFCs), alkaline fuel cells (AFCs), and phosphoric acid fuel cells (PAFCs). These fuel cells differ in terms of materials used, efficiency levels, operational temperatures, and applications. Figure 7.1 summarizes the primary characteristics of these fuel cell types [205].

Fuel cell type	Electrolyte material	Operating temperature	Application	Challenges
PEM	Polymer membrane	Below 100 °C	Stationary, portable, and transportation	Lower efficiency above 80 °C, costly
AFM	Alkaline polymer membrane	Below 75 °C	Space and transportation	CO poisoning
PAFC	Phosphoric acid matrix	100-200 °C	Stationary power generation	Corrosion, CO poisoning

Figure 7.1: Characteristics of different fuel cells, beyond SOFCs, and some of their characteristics. Adapted from [205].



---

## Appendix B

### Incorporation of protons and hydride-ions in perovskite-type oxides

#### Incorporation of protons in $ABO_3$ systems

<sup>1</sup>Protons do not exist by default in the oxide materials, but rather are incorporated into the structure [35]. The essential requirement for proton incorporation, however, is the presence of oxygen vacancies. Oxygen vacancies can be part of the structure of these oxides, or they can be created by acceptor doping as a result the difference in valency between the transition metal and dopant atom. The process used for proton incorporation is called hydration and it is performed by exposing the oxide to water vapor for certain amount of time. Upon hydration, the oxygen vacancies are filled due to water dissociation, or in terms of Kröger-Vink nomenclature:



Where  $V_O^{\cdot\cdot}$  is the oxygen vacancy present within the structure or created by acceptor doping,  $O_o^x$  is the oxygen ion on the lattice site and  $OH^{\cdot}$  is the proton localized on the oxygen ion. For the acceptor doped perovskite oxides, the number of proton concentration is roughly estimated to be equal to the dopant concentration; once incorporated, the protons remain stable at room temperature. However, increasing the temperature above certain point causes the protons to leave the structure, a process also known as dehydration.

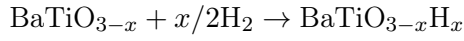
#### Incorporation of hydride-ions in hydride-ion-conducting $ABO_3$ systems

The mechanism of hydride-ion incorporation in perovskite  $ABO_3$  systems is not yet known. However, there are likely processes that are possible during the hydride reduction of these systems. In the two step case-scenario, the  $ABO_3$  system reacts with a metal hydride and creates hydrogen gas a side product. Then, the oxygen-deficient system reacts with the  $H_2$  gas in which the hydride-ion enters the perovskite framework and forms the oxyhydride [68].



---

<sup>1</sup>This part is partially included in my Licentiate thesis [1].



In the hydrogen gas case-scenario, the  $\text{ABO}_3$  system reacts with a hydrogen gas and creates oxygen vacancies on the surface. The oxygen moves up towards the surface, creating oxygen vacancies in the bulk. Consequently, the hydride ion is incorporated on the surface and penetrates down in the bulk of the material [68]. Schematic drawing is shown in Figure 7.2.

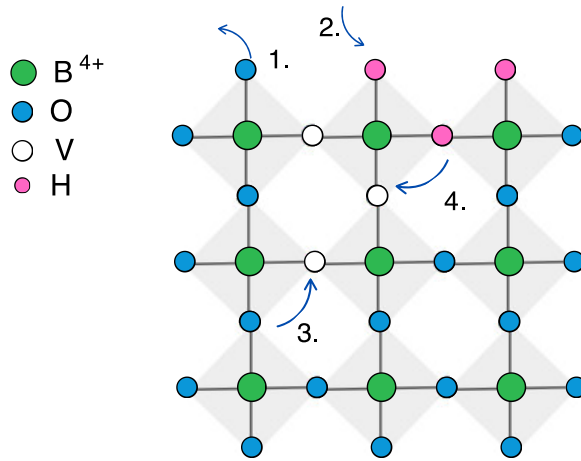
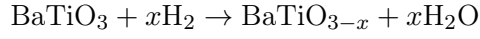


Figure 7.2: Schematic drawing of the possible hydride-ion incorporation process with hydrogen gas reduction. Oxygen vacancies are created on the surface (1); hydride-ion is incorporated (2); oxygen migrates to the surface leaving vacancies in the bulk (3); at the same time the hydride-ion diffuse into the bulk (4)

---

## Acknowledgements

My greatest gratitude is to my supervisor Prof. Maths Karlsson for the continuous support, and knowledge over these years. I am thankful to my examiner Prof. Per-Anders Carlsson, my co-supervisor Prof. Per Eklund, Prof. Martin Magnuson, Dr. Arnaud Le Febvrier, and Gabriel K. Nzulu for the all those discussions, suggestions, advice and experiment planning. To my collaborators Dr. Adrien Pericchon, Dr. Marek Koza, Prof. Max Wolff, Prof. Fabio Piccinelli and Dr. Andreas Schaefer for the enormous help in producing the papers, and interesting discussions. To Dr. Niina Jalarvo and Dr. Fanni Juranyi for your enormous help, suggestions and discussions regarding the analysis of the QENS data.

To my group who became my big family: Rasmus, Joanna, Pedram, Kanming, Bartosz, Lucas, Oskar, Peng, David, Diego and Aymen; I am so lucky I met you all; I am beyond thankful to you all for your unconditional love and support, for your help, discussions, suggestions and advice at work (and outside work), and for all these fun memories (and let's face it all memories are fun with you).

Special thank you to Prof. Christine Geers for the endless support (and cookies); you are inspirational! To Prof. Itai Panas for sharing the same enthusiasm about synthesis, the great discussions and support over the years. To Prof. Pavleta Knutsson, thank you for all your support and kindness, I am very glad I met you! To my colleagues at Materials Chemistry (current and former), thank you for everything! I am grateful to Prof. Ulrich Häussermann and Prof. Jekabs Grins from Stockholm University for the warm welcome, supervision, and great discussions during my stay. To Oskar, Anton, Samira and the rest of the Swedness group for making the conferences super fun! To Doğaç, Rui, Ruslan and Esraa; words are not enough to express my gratitude for everything. I am so lucky I have met you. To Prof. Åke Nilsson and the Jazz group: Pierre, Charity, Lennart, Börje, John, Åsgeir, Tore; I am so thankful for all of the jazz concerts and great science discussions. To the Dr. Genie group and Maria Saline for leading Chalmers towards more equality and inclusion. To Paul, Saikat, Igor, Denis, Laura and my EYE crew; thank you for everything. To Albin, Andrea, Cecilia, Eve, Dennis, Alex R, Jessica, Alex N, Guido, Yigit, and all my friends here at Chalmers for the amazing time. To Anika and Milena; my life wouldn't be complete without you in it!

To my (extended) family: Lotta, Kjell, Emma, Jonas, Wilhem and Flora; thank you for your support, love, and understanding, especially when I was busy working during holidays. To my Olle, I am so grateful for your unconditional love, support and patience. Thank you for making me (always) see the bright side of things, and for always being there with (and for) me.

Beyond all, to my parents Ina & Bobby; words could never be enough to express my gratitude...Thank you for your unconditional love and support which inspired my passion for science, and for always supporting my thirst for knowledge by providing me with all those books, encyclopedias and kids science experiments kits. I love you the most.

*Elena*



- [1] E. Naumovska, *Lic. thesis*, Chalmers Tekniska Hogskola (Sweden), 2023.
- [2] M. K. G. Deshmukh, M. Sameeroddin, D. Abdul and M. A. Sattar, *Mater. Today*, 2023, **80**, 1756–1759.
- [3] E. T. Sayed, A. G. Olabi, A. H. Alami, A. Radwan, A. Mdallal, A. Rezk and M. A. Abdelka-reem, *Energies*, 2023, **16**, 1415.
- [4] K. Richardson, W. Steffen, W. Lucht, J. Bendtsen, S. E. Cornell, J. F. Donges, M. Druke, I. Fetzer, G. Bala, W. von Bloh *et al.*, *Sci. Adv.*, 2023, **9**, 2458.
- [5] M. Granovskii, I. Dincer and M. A. Rosen, *Int. J. Hydrog. Energy*, 2007, **32**, 927–931.
- [6] J.-H. Wee, *Renew. Sust. Energ.*, 2010, **14**, 735–744.
- [7] Q. Hassan, A. K. Nassar, A. K. Al-Jiboory, P. Viktor, A. A. Telba, E. M. Awwad, A. Amjad, H. F. Fakhruldeen, S. Algburi, S. C. Mashkooor *et al.*, *Technol. Soc.*, 2024, **77**, 102535.
- [8] D. E. Matkin, I. A. Starostina, M. B. Hanif and D. A. Medvedev, *J. Mater. Chem. A*, 2024.
- [9] M. Tayyab, S. Rauf, A. Z. Khan, Z. Tayyab, K. Khan, I. Hussain, M. B. Hussain, M. Waseem, A. N. Alodhay, X.-Z. Fu *et al.*, *Ceram. Int.*, 2024.
- [10] X. Meng, H.-N. Wang, S.-Y. Song and H.-J. Zhang, *Chem. Soc. Rev.*, 2017, **46**, 464–480.
- [11] J. A. Kilner and M. Burriel, *Annu. Rev. Mater.*, 2014, **44**, 365–393.
- [12] H. Su and Y. H. Hu, *J. Chem. Eng.*, 2020, **402**, 126235.
- [13] N. Preux, A. Rolle and R. Vannier, in *N. Preux, A. Rolle and R. Vannier*, Elsevier, 2012, pp. 370–401.
- [14] H. Dai, *Ceram. Int.*, 2017, **43**, 7362–7365.
- [15] R. B. Cervera, Y. Oyama, S. Miyoshi, I. Oikawa, H. Takamura and S. Yamaguchi, *Solid State Ion.*, 2014, **264**, 1–6.
- [16] H. Shi, C. Su, R. Ran, J. Cao and Z. Shao, *Prog. Nat. Sci.: Mater. Int.*, 2020, **30**, 764–774.
- [17] O. Yamamoto, *Electrochim. Acta*, 2000, **45**, 2423–2435.

- [18] J. Larminie and A. Dicks, *Fuel Cell Systems Explained*, Wiley, 2nd edn., 2003.
- [19] *Handbook of Fuel Cell Technology*, John Wiley Sons, 3rd edn., 2001.
- [20] A. Baroutaji, T. Wilberforce, M. Ramadan and A. G. Olabi, *Renew. Sust. Energ.*, 2019, **106**, 31–40.
- [21] M. Schmelcher and J. Häßy, *Hydrogen fuel cells for aviation? A potential analysis comparing different thrust categories*, 2022.
- [22] F. A. de Bruijn, V. A. T. Dam and G. J. M. Janssen, *Fuel cells 08*, 2008, **1**, 3–22.
- [23] S. Y. Gómez and D. Hotza, *Renew. Sust. Energ.*, 2016, **61**, 155–174.
- [24] G. Hoogers, *Fuel Cell Technology Handbook*, CRC Press, 2003.
- [25] H. Shi, C. Su, R. Ran, J. Cao and Z. Shao, *Prog. Nat. Sci.: Mater. Int.*, 2020, **30**, 764–774.
- [26] D. Yan, L. Liang, J. Yang, T. Zhang, J. Pu, B. Chi and J. Li, *Energy*, 2017, **125**, 663–670.
- [27] D. Medvedev, J. Lyagaeva, E. Gorbova, A. Demin and P. Tsiakaras, *Prog. Mater. Sci.*, 2016, **75**, 38–79.
- [28] B. C. H. Steele and A. Heinzl, *Nature*, 2001, **414**, 345–352.
- [29] Y. Liu, R. Ran, M. O. Tade and Z. Shao, *J. Membr. Sci.*, 2014, **467**, 100–108.
- [30] I. Ahmed, M. Karlsson, S.-G. Eriksson, E. Ahlberg, C. S. Knee, K. Larsson, A. K. Azad, A. Matic and L. Börjesson, *J. Am. Chem. Soc.*, 2008, **91**, 3039–3044.
- [31] K. D. Kreuer, in *Perovskite Oxide for Solid Oxide Fuel Cells*, ed. T. Ishihara, Springer, 2009.
- [32] Y. Wang, K. S. Chen, J. Mishler, S. C. Cho and X. C. Adroher, *Appl. Energy*, 2011, **88**, 981–1007.
- [33] N. Kochetova, I. Animitsa, D. Medvedev, A. Demin and P. Tsiakaras, *RSC Adv.*, 2016, **6**, 73222–73268.
- [34] P. Colomban, *Proton conductors*, Cambridge University Press, 1992.
- [35] P. Colomban, *Proton Conductors: Solids, membranes and gels-materials and devices*, Cambridge University Press, 1992.
- [36] H. Iwahara, in *Proton conductors: Solids, membranes and gels - materials and devices*, ed. P. Colomban, University press, Cambridge, 1992, ch. 8.
- [37] Y.-J. Gu, Z.-G. Liu, J.-H. Ouyang, F.-Y. Yan and Y. Zhou, *Electrochim. Acta*, 2013, **105**, 547–553.
- [38] G. Ma, T. Shimura and H. Iwahara, *Solid State Ion.*, 1998, **110**, 103–110.
- [39] G. Chiodelli, L. Malavasi, C. Tealdi, S. Barison, M. Battagliarin, L. Doubova, M. Fabrizio, C. Mortalo and R. Gerbasi, *J. Alloys Compd.*, 2009, **470**, 477–485.

- [40] R. V. Kumar, *J. Alloys Compd.*, 2006, **408**, 463–467.
- [41] K. D. Kreuer, S. Adams, W. Münch, A. Fuchs, U. Klock and J. Maier, *Solid State Ion.*, 2001, **145**, 295–306.
- [42] Q. Zhang, H. Ni, L. Wang and F. Xiao, *ECS J. Solid State Sc.*, 2014, **4**, R23–R26.
- [43] W. Sun, M. Liu and W. Liu, *Adv. Energy Mater.*, 2013, **3**, 1041–1050.
- [44] A. Azad and J. Irvine, *Solid State Ion.*, 2007, **178**, 635–640.
- [45] J. Bu, P. G. Jönsson and Z. Zhao, *J. Power Sourc.*, 2014, **272**, 786–793.
- [46] J. Hyodo, K. Kitabayashi, K. Hoshino, Y. Okuyama and Y. Yamazaki, *Adv. Energy Mater.*, 2020, **10**, 2000213.
- [47] B. Bogdanovic, R. A. Brand, A. Marjanovic, M. Schwickardi and J. Tolle, *J. Alloys Compd.*, 2000, **302**, 36–58.
- [48] D. Navas, S. Fuentes, A. Castro-Alvarez and E. Chavez-Angel, *Gels*, 2021, **7**, 275.
- [49] M. K. Hossain, M. C. Biswas, R. K. Chanda, M. H. Rubel, M. I. Khan and K. Hashizume, *Emergent Mater.*, 2021, **4**, 999–1027.
- [50] A. K. Nayak and A. Sasmal, *J. Clean. Prod.*, 2023, **386**, 135827.
- [51] J. Li, C. Wang, X. Wang and L. Bi, *Electrochem. commun.*, 2020, **112**, 106672.
- [52] A. Løken, T. S. Bjørheim and R. Haugrud, *J. Mater. Chem. A*, 2015, **3**, 23289–23298.
- [53] T. S. Bjørheim, A. Løken and R. Haugrud, *J. Mater. Chem. A*, 2016, **4**, 5917–5924.
- [54] U. Tariq, M. Z. Khan, O. Gohar, Z. U. D. Babar, F. Ali, R. A. Malik, I. A. Starostina, J. Rehman, I. Hussain, M. Saleem *et al.*, *J. Power Sourc.*, 2024, **613**, 234910.
- [55] S. Fop, *J. Mater. Chem. A*, 2021, **9**, 18836–18856.
- [56] J. Zhao and X. Wang, *ACS omega*, 2022, **7**, 10483–10491.
- [57] V. Sharma, P. Kumar, P. Dev and G. Pilania, *J. Appl. Phys.*, 2020, **128**, 034902.
- [58] M. Karlsson, *Phys. Chem. Chem. Phys.*, 2015, **17**, 26.
- [59] M. Coduri, M. Karlsson and L. Malavasi, *J. Mater. Chem. A*, 2022, **10**, 5082–5110.
- [60] Y. Izumi, F. Takeiri, K. Okamoto, T. Saito, T. Kamiyama, A. Kuwabara and G. Kobayashi, *Adv. Energy Mater.*, 2023, **13**, 2301993.
- [61] G. Bouilly, T. Yajima, T. Terashima, W. Yoshimune, K. Nakano, C. Tassel, Y. Kususe, K. Fujita, K. Tanaka, T. Yamamoto *et al.*, *Chem. Mat.*, 2015, **27**, 6354–6359.
- [62] T. Yajima, A. Kitada, Y. Kobayashi, T. Sakaguchi, G. Bouilly, S. Kasahara, T. Terashima, M. Takano and H. Kagayama, *J. Am. Chem. Soc.*, 2012, **134**, 8782–8785.

- [63] C. Eklöf-Österberg, R. Nedumkandathil, U. Häussermann, A. Jaworski, A. J. Pell, M. Tyagi, N. H. Jalarvo, B. Frick, A. Faraone and M. Karlsson, *J. Phys. Chem. C*, 2018, **123**, 2019–2030.
- [64] H. Kageyama, H. Ogino, T. Zhu and T. Hasegawa, *Mixed-anion Compounds*, Royal Society of Chemistry, 2024.
- [65] H. Kageyama, K. Hayashi, K. Maeda, J. P. Attfield, Z. Hiroi, J. M. Rondinelli and K. R. Poeppelmeier, *Nature Commun.*, 2018, **9**, 772.
- [66] Y. Kobayashi, O. J. Hernandez, T. Sakaguchi, T. Yajima, T. Roisnel, Y. Tsujimoto, M. Morita, Y. Noda, Y. Mogami, A. Kitada, M. Ohkura, S. Hosokawa, Z. Li, K. Hayashi, Y. Kusano, J. eun Kim, N. Tsuji, A. Fujiwara, Y. Matsushita, K. Yoshimura, K. Takegoshi, M. Inoue, M. Takano and H. Kageyama, *Nat. Mater.*, 2012, **11**, 507–511.
- [67] H. Guo, A. Jaworski, Z. Ma, A. Slabon, Z. Bacsik, R. Nedumkandathil and U. Häussermann, *RSC Adv.*, 2020, **10**, 35356–35365.
- [68] R. Nedumkandathil, A. Jaworski, J. Grins, D. Bernin, M. Karlsson, C. Eklöf-Österberg, A. Neagu, C.-W. Tai, A. J. Pell and U. Häussermann, *Acs Omega*, 2018, **3**, 11426–11438.
- [69] H. Guo, *Ph.D. thesis*, Department of Materials and Environmental Chemistry, Stockholm University, 2021.
- [70] H. Toriumi, G. Kobayashi, T. Saito, T. Kamiyama, T. Sakai, T. Nomura, S. Kitano, H. Habazaki and Y. Aoki, *Chem. Mat.*, 2022, **34**, 7389–7401.
- [71] Y. Kobayashi, Y. Tang, T. Kageyama, H. Yamashita, N. Masuda, S. Hosokawa and H. Kageyama, *Journal of the American Chemical Society*, 2017, **139**, 18240–18246.
- [72] Y. Tang, Y. Kobayashi, N. Masuda, Y. Uchida, H. Okamoto, T. Kageyama, S. Hosokawa, F. Loyer, K. Mitsuhara, K. Yamanaka *et al.*, *Adv. Energy Mater.*, 2018, **8**, 1801772.
- [73] Y. Tang, Y. Kobayashi, C. Tassel, T. Yamamoto and H. Kageyama, *Adv. Energy Mater.*, 2018, **8**, 1800800.
- [74] K. Fukui, S. Iimura, T. Tada, S. Fujitsu, M. Sasase, H. Tamatsukuri, T. Honda, K. Ikeda, T. Otomo and H. Hosono, *Nat. Commun.*, 2019, **10**, 2578.
- [75] F. Takeiri, A. Watanabe, A. Kuwabara, H. Nawaz, N. I. P. Ayu, M. Yonemura, R. Kanno and G. Kobayashi, *Inorg. Chem.*, 2019, **58**, 4431–4436.
- [76] X. Zhang, S. H. Chan, G. Li, H. K. Ho, J. Li and Z. Feng, *J. Power Sourc.*, 2010, **195**, 685–702.
- [77] M. B. Hanif, S. Rauf, M. Motola, Z. U. D. Babar, C.-J. Li and C.-X. Li, *Mater. Res. Bull.*, 2022, **146**, 111612.
- [78] Y. Tang, Y. Kobayashi, K. Shitara, A. Konishi, A. Kuwabara, T. Nakashima, C. Tassel, T. Yamamoto and H. Kageyama, *Chem. Mat.*, 2017, **29**, 8187–8194.
- [79] R. Lavén, *PhD thesis*, Chalmers Tekniska Hogskola (Sweden), 2023.
- [80] L. Fine, *Lic. thesis*, Chalmers Tekniska Hogskola (Sweden), 2024.

- [81] T. Wei, L. A. Zhang, Y. Chen, P. Yang and M. Liu, *Chem. Mat.*, 2017, **29**, 1490–1495.
- [82] T. Takahashi and H. Iwahara, *Rev. Chim. Miner.*, 1980, **17**, 243–253.
- [83] K. D. Kreuer, *J. Chem. Phys. Chem.*, 2002, **3**, 771–775.
- [84] G. Zhang and D. Smyth, *Solid State Ion.*, 1995, **82**, 153–160.
- [85] T. Schober, J. Friedrich and F. Krug, *Solid State Ion.*, 1997, **99**, 9–13.
- [86] F. Giannici, A. Longo, K.-D. Kreuer, A. Balerna and A. Martorana, *Solid State Ion.*, 2010, **181**, 122–125.
- [87] R. B. Cervera, Y. Oyama, S. Miyoshi, K. Kobayashi, T. Yagi and S. Yamaguchi, *Solid State Ion.*, 2008, **179**, 236–242.
- [88] S. Tao and J. T. S. Irvine, *Adv. Mat.*, 2006, **18**, 1581.
- [89] J. Tong, D. Clark, M. Hoban and R. O’Hayre, *Solid State Ion.*, 2010, **181**, 496–503.
- [90] C. Zuo, S. Zha, M. Liu, M. Hatano and M. Uchiyama, *Adv. Mater.*, 2006, **18**, 3318–3320.
- [91] K. Saito and M. Yashima, *Nat. Commun.*, 2023, **14**, 7466.
- [92] J. Bielecki, S. F. Parker, L. Mazzei, L. Börjesson and M. Karlsson, *J. Mater. Chem. A*, 2016, **4**, 1224–1232.
- [93] A. Perrichon, M. Jiminez-Ruiz, L. Mazzei, S. M. H. Rahman and M. Karlsson, *J. Mater. Chem. A*, 2019, **7**, 17626–17636.
- [94] G. Zhang and D. Smyth, *Solid State Ion.*, 1995, **82**, 153–160.
- [95] A. Jarry, E. Quarez, K. Kravchyk and O. Joubert, *Solid State Ion.*, 2012, **216**, 11–14.
- [96] H. Kawamori, I. Oikawa and H. Takamura, *Chem. Mat.*, 2021, **33**, 5935–5942.
- [97] L. Mazzei, *PhD thesis*, Chalmers Tekniska Hogskola (Sweden), 2019.
- [98] D. Noferini, *PhD thesis*, Chalmers Tekniska Hogskola (Sweden), 2018.
- [99] K. D. Kreuer, *Annu. Rev. Mater. Res.*, 2003, **33**, 333–359.
- [100] R. A. Davies, M. S. Islam and J. D. Gale, *Solid State Ion.*, 1999, **126**, 323–335.
- [101] P. G. Sundell, M. E. Björketun and G. Wahnström, *Phys. Rev. B: Condens. Matter*, 2006, **73**, 104112.
- [102] M. E. Björketun, P. G. Sundell and G. Wahnström, *Faraday Discuss.*, 2007, **134**, 247–265.
- [103] K. D. Kreuer, E. Schönherr and J. Maier, in *Proceedings of the 14th Risø International Symposium on Materials Science*, ed. F. Poulsen, J. Bentzen, T. Jacobsen, E. Skou and M. Østergård, 1993, pp. 297–304.
- [104] D. Shima and S. M. Haile, *Solid State Ion.*, 1997, **97**, 443–455.

- [105] S. M. Haile, D. A. Boysen, C. R. I. Chisholm and R. B. Merle, *Nature*, 2001, **410**, 910–913.
- [106] L. Mazzei, A. Perrichon, A. Mancini, G. Wahnström, L. Malavasi, S. F. Parker and L. Börjesson, *J. Mater. Chem. A*, 2019, **7**, 7360–7372.
- [107] M. Karlsson, M. E. Björketun, P. G. Sundell, A. Matic, G. Wahnström, D. Engberg, L. Börjesson, I. Ahmed, S. G. Eriksson and P. Berastegui, *Phys. Rev. B*, 2005, **72**, 094303: 1–7.
- [108] D. Noferini, M. M. Koza, S. M. H. Rahman, Z. Evenson, G. J. Nilsen, S. Eriksson, A. R. Wildes and M. Karlsson, *Phys. Chem. Chem. Phys.*, 2018, **20**, 13697–13704.
- [109] P. Du, Q. Chen, Z. Fan, H. Pan, F. G. Haibach, M. A. Gomez and A. Braun, *Commun. phys.*, 2020, **3**, 200:1–9.
- [110] M. Karlsson, *Dalton Trans.*, 2013, **42**, 317–329.
- [111] W. Münch, G. Seifert, K. D. Kreuer and J. Maier, *Solid State Ion.*, 1996, **86-88**, 647–652.
- [112] R. Hempelmann, C. Karmonik, T. Matzke, M. Cappadonia, U. Stimming, T. Springer and M. A. Adams, *Solid State Ion.*, 1995, **77**, 152–156.
- [113] T. Matzke, U. Stimming, C. Karmonik, M. Soetramo, R. Hempelmann and F. Güthoff, *Solid State Ion.*, 1996, **86-88**, 621–628.
- [114] C. Karmonik, R. Hempelmann, J. Cook and F. Güthoff, *Ionics*, 1996, **2**, 69.
- [115] D. Noferini, M. M. Koza and M. Karlsson, *J. Phys. Chem. C*, 2017, **121**, 7088–7093.
- [116] D. Noferini, M. M. Koza, S. M. H. Rahma, Z. Evenson, G. J. Nilsen, S. Eriksson, A. R. Wildes and M. Karlsson, *Phys. Chem. Chem. Phys.*, 2018, **20**, 13697–13704.
- [117] M. Pionke, T. Mono, W. Schweika, T. Springer and H. Schober, *Solid State Ion.*, 1997, **97**, 497–504.
- [118] M. Karlsson, D. Engberg, M. E. Björketun, A. Matic, G. Wahnström, P. G. Sundell, P. Berastegui, I. Ahmed, P. Falus, B. Farago, L. Börjesson and S. Eriksson, *Chem. Mater.*, 2010, **22**, 740–742.
- [119] K. D. Kreuer, *Solid State Ion.*, 2000, **136-137**, 149–160.
- [120] D.-H. Kim, B.-K. Kim and Y.-C. Kim, *Solid State Ion.*, 2013, **213**, 18–21.
- [121] M. A. Gomez, M. A. G. A. S. Jindal, K. D. Rule and V. R. Cooper, *J. Chem. Phys.*, 2005, **123**, 094703.
- [122] L. Mazzei, A. Perrichon, A. Mancini, L. Malavasi, S. F. Parker, L. Börjesson and M. Karlsson, *J. Phys. Chem. C*, 2019, **123**, 26065–26072.
- [123] K. D. Kreuer, S. J. Paddison, E. Spohr and M. Schuster, *Chem. Rev.*, 2004, **104**, 4637–4678.
- [124] M. Cherry, M. S. Islam, J. D. Gale and C. R. A. Catlow, *Solid State Ion.*, 1995, **77**, 207–209.
- [125] L. Malavasi, C. A. J. Fisher and M. S. Islam, *Chem. Soc. Rev.*, 2010, **39**, 4370.

- [126] W. Münch, G. Seifert, K. D. Kreuer and J. Maier, *Solid State Ion.*, 1997, **97**, 39–44.
- [127] K. D. Kreuer, *Solid State Ion.*, 1999, **125**, 285–302.
- [128] Q. Zhang, G. Wahnström, M. E. Björketun, S. Gao and E. Wang, *Physical Review Letters*, 2008, **101**, 1–4.
- [129] A. Perrichon, M. M. Koza, Z. Evenson, B. Frick, F. Demmel, P. Fouquet and M. Karlsson, *Chem. Mat.*, 2023.
- [130] E. Naumovska, J. Orstadius, A. Perrichon, R. Lavén, M. M. Koza, Z. Evenson and M. Karlsson, *J. Phys. Chem. C*, 2023, **127**, 24532–24541.
- [131] R. Hempelmann, *Quasielastic neutron scattering and solid state diffusion*, 2000.
- [132] A. Mancini, J. F. Shin, A. Orera, P. R. Slater, C. Tealdi, Y. Ren, K. L. Page and L. Malavasi, *Dalton Trans.*, 2012, **41**, 50–53.
- [133] T. Schober, J. Friedrich and F. Krug, *Solid State Ion.*, 1997, **99**, 9–13.
- [134] S. Noirault, E. Quarez, Y. Piffard and O. Joubert, *Solid State Ion.*, 2009, **180**, 1157–1163.
- [135] L. Mazzei, F. Piccinelli, M. Bettinelli, S. F. Parker and M. Karlsson, *Solid State Ion.*, 2021, **365**, 115624.
- [136] J. Bielecki, S. F. Parker, D. Ekanayake, S. M. H. Rahman, L. Börjesson and M. Karlsson, *J. Mater. Chem. A*, 2014, 16915–16924.
- [137] J.-R. Martinez, C. E. Mohn, S. Stoelen and N. L. Allan, *J. Solid State Chem.*, 2007, **180**, 3388.
- [138] V. Jayaraman, A. Magrez, M. Caldes, O. Joubert, F. Taulelle, J. Rodriguez-Carvajal, Y. Piffard and L. Brohan, *Solid State Ion.*, 2004, **170**, 25.
- [139] S. Sun, Q. Tang, K. Zhang, Y. Wen, A. Billings and K. Huang, *Mater. Adv.*, 2023, **4**, 389–407.
- [140] M. A. Hayward, E. J. Cussen, J. B. Claridge, M. Bieringer, M. J. Rosseinsky, C. J. Kiely, S. J. Blundell, I. M. Marshall and F. L. Pratt, *Science*, 2002, **295**, 1882–1884.
- [141] G. Kobayashi, Y. Hinuma, S. Matsuoka, A. Watanabe, M. Iqbal, M. Hirayama, M. Yonemura, T. Kamiyama, I. Tanaka and R. Kanno, *Science*, 2016, **351**, 1314–1317.
- [142] F. Takeiri, A. Watanabe, K. Okamoto, D. Bresser, S. Lyonard, B. Frick, A. Ali, Y. Imai, M. Nishikawa, M. Yonemura *et al.*, *Nature Mater.*, 2022, **21**, 325–330.
- [143] T. Sakaguchi, Y. Kobayashi, T. Yajima, M. Ohkura, C. Tassel, F. Takeiri, S. Mitsuoka, H. Ohkubo, T. Yamamoto, J. E. Kim *et al.*, *Inorg. Chem.*, 2012, **51**, 11371–11376.
- [144] Y. Iwazaki, T. Suzuki, Y. Mizuno and S. Tsuneyuki, *Phys.Rev.B*, 2012, **86**, 214103.
- [145] R. Nedumkandathil, A. Jaworski, J. Grins, D. Bernin, M. Karlsson, C. Eklöf-Österberg, A. Neagu, C.-W. Tai, A. J. Pell and U. Häussermann, *Acs Omega*, 2018, **3**, 11426–11438.

- [146] K. Arai, K. Onagi, Y. Tang, T. Ishigaki, H. Sai, Y. Sasahara, G. Caruntu, H. Okabe, M. Harada, K. Nakashima *et al.*, *Inorg. Chem.*, 2024, **63**, 23260–23266.
- [147] T. Uchimura, F. Takeiri, K. Okamoto, T. Saito, T. Kamiyama and G. Kobayashi, *J. Mater. Chem. A*, 2021, **9**, 20371–20374.
- [148] G. Kobayashi, Y. Hinuma, S. Matsuoka, A. Watanabe, M. Iqbal, M. Hirayama, M. Yonemura, T. Kamiyama, I. Tanaka and R. Kanno, *Science*, 2016, **351**, 1314–1317.
- [149] N. Masuda, Y. Kobayashi, O. Hernandez, T. Bataille, S. Paofai, H. Suzuki, C. Ritter, N. Ichijo, Y. Noda, K. Takegoshi *et al.*, *J. Am. Chem. Soc.*, 2015, **137**, 15315–15321.
- [150] T. Yajima, F. Takeiri, K. Aidzu, H. Akamatsu, K. Fujita, W. Yoshimune, M. Ohkura, S. Lei, V. Gopalan, K. Tanaka *et al.*, *Nat. Chem.*, 2015, **7**, 1017–1023.
- [151] V. Agafonov, A. Kahn, D. Michel and M. Guymont, *Mater. Res. Bull.*, 1983, **18**, 975–981.
- [152] N. Torino, *PhD thesis*, Chalmers Tekniska Hogskola (Sweden), 2019.
- [153] K. D. Kreuer, E. Schönherr and J. Maier, *Solid State Ion.*, 1994, **70-71**, 278–284.
- [154] C. Duan, R. Kee, H. Zhu, N. Sullivan, L. Shu, L. Bian, D. Jennings and R. O’Hayre, *Nature Energy*, 2019, **4**, 230–240.
- [155] J. Habash, J. Raftery, R. Nuttall, H. Price, C. Wilkinson, A. Kalb and J. Helliwell, *Acta Crystallogr. D*, 2000, **56**, 541–550.
- [156] F. Iguchi, T. Tsurui, N. Sata, Y. Nagao and H. Yugami, *Solid State Ion.*, 2009, **180**, 563–568.
- [157] F. J. Loureiro, N. Nasani, G. S. Reddy, N. Munirathnam and D. P. Fagg, *J. Power Sourc.*, 2019, **438**, 226991.
- [158] N. Torino, P. F. Henry, C. S. Knee, T. S. Bjørheim, S. M. Rahman, E. Suard, C. Giacobbe and S. G. Eriksson, *Dalton Transactions*, 2017, **46**, 8387–8398.
- [159] N. Torino, P. F. Henry, C. S. Knee, S. K. Callear, R. I. Smith, S. M. H. Rahman and S. G. Eriksson, *Solid State Ion.*, 2018, **324**, 233–240.
- [160] P. Babilo, T. Uda and S. M. Haile, *J. Mater. Res.*, 2007, **22**, 1322.
- [161] Y. Yamazaki, R. Hernandez-Sanchez and S. M. Haile, *Chem. Mat.*, 2009, **21**, 2755–2762.
- [162] A. K. Eessaa and A. El-Shamy, *Microelectron. Eng.*, 2023, **279**, 112061.
- [163] P. J. Kelly and R. D. Arnell, *Vacuum*, 2000, **56**, 159–172.
- [164] A. Le Febvrier, L. Landälv, T. Liersch, D. Sandmark, P. Sandström and P. Eklund, *Vacuum*, 2021, **187**, 110137.
- [165] G. K. Nzulu, E. Naumovska, M. Karlsson, P. Eklund, M. Magnuson and A. le Febvrier, *Thin Solid Films*, 2023, **772**, 139803.
- [166] N. Salazar, C. Marquez and F. Gamiz, in *2D Materials for Nanophotonics*, Elsevier, 2021, pp. 1–79.

- [167] V. Demange, X. Portier, S. Ollivier, M. Pasturel, T. Roisnel, M. Guilloux-Viry, C. Hebert, M. Nistor, C. Cachoncinlle, E. Millon *et al.*, *Cryst. Growth Des.*, 2023, **23**, 8534–8543.
- [168] S. Steinsvik, Y. Larring and T. Norby, *Solid State Ion.*, 2001, **143**, 103–116.
- [169] F. W. Poulsen, *Solid State Ion.*, 2001, **145**, 387–397.
- [170] P. Lindner and T. Zemb, *Neutrons, X-rays and Light: Scattering Methods Applied to Soft Condensed Matter*, Elsevier, 2002.
- [171] NMI3, *Neutron methods and techniques for research*, <https://nmi3.eu/neutron-research/techniques-for-.html>.
- [172] P. C. H. Mitchell, S. F. Parker, A. J. Ramirez-Cuesta and J. Tomkinson, *Vibrational Spectroscopy with Neutrons - With Applications in Chemistry, Biology, Materials Science and Catalysis*, World Scientific Publishing, 2005.
- [173] R. Pynn, *Neutron Scattering - A Primer*, 2000.
- [174] L. V. Hove, *Phys. Rev.*, 1954, **95**, 249–262.
- [175] M. Karlsson, *Phys. Chem. Chem. Phys.*, 2015, **17**, 26–38.
- [176] M. Karlsson, A. Matic, D. Engberg, M. E. Björketun, M. M. Koza, I. Ahmed, G. Wahnström, P. Berastegui, L. Börjesson and S. G. Eriksson, *Solid State Ion.*, 2009, **180**, 22.
- [177] D. Noferini, M. M. Koza, P. Fouquet, G. J. Nilsen, M. C. Kemei, S. M. H. Rahman, M. Maccarini, S. Eriksson and M. Karlsson, *J. Phys. Chem. C*, 2016, **120**, 13963–13969.
- [178] C. T. Chudley and R. J. Elliott, *Proc. Phys. Soc.*, 1961, **77**, 353.
- [179] P. Hall and D. K. Ross, *Mol. Phys.*, 1981, **42**, 673.
- [180] K. Singwi and A. Sjölander, *Phys. Rev.*, 1960, **120**, 1093.
- [181] M. Karlsson, *PhD thesis*, Chalmers University of Technology, 2007.
- [182] C. Eköf-Österberg, L. Mazzei, E. J. Granhed, G. Wahnström, R. Nedumkandathil, U. Häussermann, A. Jawroski, A. J. Pell, S. F. Parker and M. Karlsson, *J. Mater. Chem. A*, 2019.
- [183] P. Sindhu, *Fundamentals of Molecular Spectroscopy.*, New Age International, 2006.
- [184] S. Gaisford, V. Kett and P. Haines, *Principles of thermal analysis and calorimetry*, Royal society of chemistry, 2019.
- [185] E. Fabbri, D. Pergolesi and E. Traversa, *Chem. Soc. Rev.*, 2010, **39**, 4355.
- [186] A. K. E. Eriksson, S. M. Selbach, C. S. Knee and T. Grande, *J. Am. Ceram. Soc.*, 2014, **07**, 2654–2661.
- [187] C. W. Mburu, S. M. Gaita, C. S. Knee, M. J. Gatari and M. Karlsson, *J. Phys. Chem. C*, 2017, **121**, 16174–16181.
- [188] M. Wilde and K. Fukutani, *Surf. Sci. Rep.*, 2014, **69**, 196–295.

- [189] L. Mazzei, M. Wolff, D. Pergolesi, J. A. Dura, L. Börjesson, P. Gutfreund, M. Bettinelli, T. Lippert and M. Karlsson, *J. Phys. Chem. C*, 2016, **120**, 28415–28422.
- [190] M. Weller and N. Young, *Characterisation methods in inorganic chemistry*, Oxford University Press, 2017.
- [191] B. Dutrow and C. Clark, *X-ray Powder Diffraction (XRD)*, 2007, [https://serc.carleton.edu/research\\_education/geochemsheets/techniques/XRD.html](https://serc.carleton.edu/research_education/geochemsheets/techniques/XRD.html) [Accessed: May 2025].
- [192] M. Karlsson, *PhD thesis*, Chalmers University of Technology, 2007.
- [193] W. Lohstroh and Z. Evenson, *JLSRF*, 2015, **1**, A15–A15.
- [194] A. Anghel, F. Atchison, B. Blau, B. Van den Brandt, M. Daum, R. Doelling, M. Dubs, P.-A. Duperrex, A. Fuchs, D. George *et al.*, *Nucl. Instrum. Methods Phys. Res. A*, 2009, **611**, 272–275.
- [195] E. Mamontov, M. Zamponi, S. Hammons, W. S. Keener, M. Hagen and K. W. Herwig, *Neutron News*, 2008, **19**, 22–24.
- [196] L. Mazzei, A. Perrichon, A. Mancini, L. Malavasi, S. F. Parker, L. Börjesson and M. Karlsson, *J. Phys. Chem. C*, 2019, **123**, 26065–26072.
- [197] M. Weller and N. Young, 2017.
- [198] E. Naumovska, J. Orstadius, A. Perrichon, R. Lavén, M. M. Koza, Z. Evenson and M. Karlsson, *J. Phys. Chem. C*, 2023, **127**, 24532–24541.
- [199] E. Naumovska, G. K. Nzulu, L. Mazzei, A. Le Febvrier, K. Komander, M. Magnuson, M. Wolff, P. Eklund and M. Karlsson, *Vib. Spectrosc.*, 2024, **130**, 103622.
- [200] M. Karlsson, A. Matic, D. Engberg, M. E. Björketun, M. M. Koza, I. Ahmed, G. Wahnström, P. Berastegui, L. Börjesson and S. G. Eriksson, *Solid State Ion.*, 2009, **180**, 22–28.
- [201] M. Karlsson, in *Neutron Applications in Materials for Energy*, ed. G. J. Kearley and V. K. Peterson, Springer, 2015, ch. 9.
- [202] D. Noferini, M. M. Koza, S. M. H. Rahman, Z. Evenson, G. J. Nilsen, S. Eriksson, A. R. Wildes and M. Karlsson, *Phys. Chem. Chem. Phys.*, 2018, **20**, 13697–13704.
- [203] D. Noferini, M. M. Koza and M. Karlsson, *J. Phys. Chem. C*, 2017, **121**, 7088–7093.
- [204] D. Noferini, M. M. Koza, P. Fouquet, G. J. Nilsen, M. C. Kemei, S. M. H. Rahman, M. Maccarini, S. Eriksson and M. Karlsson, *J. Phys. Chem. C*, 2016, **120**, 13963–13969.
- [205] A. Talukdar, A. Chakrovorty, P. Sarmah, P. Paramasivam, V. Kumar, S. K. Yadav and S. Manickkam, *Int. J. Energy Res.*, 2024, **2024**, 6443247.



